Physics of Cytokinesis

A Thesis

Submitted to the
Tata Institute of Fundamental Research, Mumbai
Subject Board of Biology
for the degree of Doctor of Philosophy

by

Aditya Singh Rajput

International Centre for Theoretical Sciences
Tata Institute of Fundamental Research

April, 2026

Declaration

This thesis is a presentation of my original research work. Wherever contributions of others are involved, every effort is made to indicate this clearly, with due reference to the literature, and acknowledgement of collaborative research and discussions.

The work was done under the guidance of Professor Vijaykumar Krishnamurthy at the Tata Institute of Fundamental Research, Mumbai. Professor Masatoshi Nishikawa served as co-supervisor.

(Aditya Singh Rajput)

In my capacity as the formal supervisor of record of the candidate's thesis, I certify that the above statements are true to the best of my knowledge.

(Vijaykumar Krishnamurthy)

Date: 16 April 2026

ACKNOWLEDGEMENTS

> *Plato has said, man is a heavenly plant.*
> *The indication of this is that he is like an inverted tree:*
> *its roots are toward heaven and its branches are toward the earth.*
>
> *al-Mas'ūdī*

I would first like to thank my advisors Prof. Vijaykumar Krishnamurthy and Prof. Masatoshi Nishikawa for their support, guidance, and encouragement through these past years. They are both extremely gentle, and, it would go without saying, scholarly. I am constantly amazed by the breadth of Vijay's interests, both scientific and otherwise. This always makes for interesting conversation, even when we disagree. Perhaps, specifically when we disagree. Masatoshi (Ma) has a view of science that seems almost unperturbed by the cynicism that often plagues a lot of us in academia. All the new experiments reported in this thesis were performed by him. He is an extremely rare scientist, and it has been an absolute pleasure working with him and a privilege to get to know him.

Towards Prof. Vidyanand Nanjundiah, I feel a kind of gratitude that can be hardly put into words. Every dinner conversation, every walk, and every scientific discussion (and every email!) with him turns out to be memorable. I am thankful to him for relentlessly entertaining my almost nonsensical ramblings about physics, history, and embryology. I would like to thank Prof. Rama Govindarajan for the one-person course on Fluid Mechanics that I greatly enjoyed. She was instrumental in developing the intuition I often relied on during this work. The members of my thesis committee; Prof. Maithreyi Narasimha, Prof. Vishal Vasan, and Prof. Sriram Ramaswamy were very patient and helpful in all discussions. I thank them for the constant encouragement. I also thank Dr. Vikas Trivedi for many exciting discussions on about everything that came to our heads. I look forward to many more in the future.

During my time in Mumbai, Prof. Swapan Ghosh was an inspirational presence and was one of the first people who supported my

interest in theoretical physics and biology. He is also the one who introduced me to active matter for the first time.

I thank Prof. Boris Shraiman and Prof. Sebastian Streichan for the opportunity to attend the QBio at KITP. I thank Prof. Amy Shyer and Prof. Alan Rodrigues for their encouragement and patience while a theorist made a mess of chicken embryos. I greatly enjoyed working with the Sichen, Vanessa, Ramya, and Alex during the school, all of whom have become lifelong friends.

I thank Dr. Mathhias Merkel and Prof. Thomas Lecuit for hosting me in Marseille for an ongoing collaboration, it was also during this visit that parts of this thesis were written. I thank Patrick and Michael for exciting discussions and for the great company in Marseille, and now while working on this collaboration. I thank TIFR for a Sarojini-Damodaran fellowship that partially funded this visit.

I was lucky to enjoy the company of fantastic colleagues. Jigyasa is an astonishingly rigorous physicist and has been a wonderful comrade since the beginning of this work. I thank Kunal, Aiswarya, Diksha, Sangeetha, and Ankan for the many wonderful discussions. Kunal was especially supportive during a crucial period, and is an endless source of enthusiasm which keeps the spirits up. Parts of chapter 3 and 4 were worked on in collaboration with him. I thank all the other members of the Biophysics group. It warms my heart to now see a flourishing community at ICTS, interested in biological problems.

The office where most of this work was done was made lively by the constant puzzles from Ankush, and equally constant retorts from H. Joshi. I thank both of them for being as fun, sharp, and, lighthearted as they are. The associate visitor in this office, Sparsh is a friend since college days, and has been a part of many (mis?) adventures mentioned above. I also thank Prateek Anand who pushed me to pen the very first sentence of this thesis.

I thank my friends at NCBS: Nivya, Sukanta, Shreyas, Aboli, Srishti, Abel, Heera, Ajay, Maroof, and Sricharan; with whom many an aimless conversation and many a passionate debate were had. A special thanks to Shubhangi who has been a pillar of support throughout, and has been a partner-in-crime for all that is closest to my heart. I have her to thank for many logical points of this work which came out during our discussions.

I also thank my friends from college: Swarnim, Shashank, and Ashish, without whom the time spent in Mumbai would not have been anywhere as memorable. I am sure I have missed out on thanking

many people here, apologies to you all. If it has happened, it is only in a fugue of immense gratitude towards so many.

Throughout my childhood, I was constantly encouraged in whatever I wished to pursue, and I have my family to thank for it. As I write this, my head fills with nebulous memories of my mother explaining why the diagonal road to home was shorter, by arranging noodles into a triangle on a plate; of my sister sketching out cells at the back of a notebook; of my father telling me why the train that passed us by felt like it was going faster than it actually was.

This thesis is dedicated to all my teachers.

To the ones I met too early, and the ones I met too late.
To the mentors, who eventually became friends.
To the friends who became my mentors;
and to the first teachers: my sister, my mother, and my father.

LIST OF FIGURES

CONTENTS

ABSTRACT

Cell division is a fundamental biological process that ensures the segregation of genetic material and also involves dramatic changes in the cellular geometry, leading to cytokinesis: the cleavage of a cell giving rise to two daughter cells. In metazoans, cytokinesis is orchestrated by flows resulting from active stress gradients in the actomyosin cortex – a thin film comprising myosin motors, actin filaments, and other associated macromolecules. In this thesis, we develop a theory for the geometrodynamics of the cortex treated as an active surface.

First, we establish the necessary mathematical tools for the geometry of surfaces in ambient coordinates. To deal with dynamical geometries, we also derive the necessary equations for the kinematics of moving surfaces. Relying on this formulation, we solve the relevant equations using a flexible computational finite-element method using on the FeniCS library.

Next, we explore the interplay between the active patterns with fixed curved geometry. We show that the steady state patterns predicted on simple geometries localise on regions of different curvatures dependent on the parameters. This seems to arise from the Gaussian curvature acting as an effective friction on curved surfaces. We also observe that qualitatively new patterns emerge purely due to the change in geometry when the surfaces have regions of negative Gaussian curvature, naturally giving rise to cytokinesis-like patterns of myosin distribution and flows.

Finally, we turn to the full problem of the interplay of active patterns and dynamical geometry. At high contractility, we observe self-organised dynamics of the cytokinetic furrow and concomitant myosin patterns, which agree well with experimental measurements on the dynamics of cytokinetic ring, surface curvature, and rate of myosin accumulation during the first division in the *C. elegans* embryo. We then propose an approximate theory assuming only the feedback from concentration changes due to geometric effects, and the resulting changes in the dynamics of geometry due to altered active stresses. We find a linear relationship between myosin accumulation rates and the speed of ring contraction in the theory, and observe this relation across

several RNAi perturbations in the embryo. Through the same RNAi perturbations, we further test our prediction that higher contractility generically leads to asymmetric ingression. This work suggests that active, self-organised dynamics could underlie the widely observed kinematic features and asymmetries in cytokinesis.

1

INTRODUCTION: CELLS AND CYTOKINESIS

> *. . . something unfailingly upsets our physical intuition as we watch this phenomenon, whose strangeness is even more appreciable than before the experiment. Why? Because we see very clearly that this process is bent or oriented in one exclusive direction: the multiplication of cells. These to be sure do not violate the laws of thermodynamics, quite the contrary.*
> *They not only obey them; they utilize them as a good engineer would, with maximum efficiency, to carry out the project and bring about (as François Jacob has put it) the "dream" of every cell: to become two cells.*
>
> *Jacques Monod*
> *Chance and Necessity (1970)*

The ability to replicate is a universal feature of all cellular life forms. It is unclear what the earliest cells looked like, but we imagine them to be a compartment capable of both chemical replication (of the primordial genetic constituents) and physical separation (of the primordial membrane enclosing these genetic constituents) [Szostak et al., 2001]. There is a strong possibility that our view of the earliest cells is biased by their descendants roughly 3 billion years later. However, noticing the common phenomena in cells operating at remarkably different length-, and time-scales, with some liberty, one can postulate the existence of an ancestral cell which, while primitive, showed both of these features as far as its replication was concerned. We could ask: How did an ancestral eukaryotic cell develop robust mechanisms for division such that these processes have been inherited across generations? Clearly, evolutionary processes have built on this robust mechanism, leading to the current stunning diversity of multicellular life. What simple *regulatory constraints* can allow for the robustness of this replication mechanism? Can self-organised patterns emerging from physical

processes allow for such minimal cells to execute their "function"? If yes, what kind of physical principles underlie this self-organisation?

In this introductory chapter, we discuss physical principles and relevant experimental findings based on which one can build a theoretical framework for understanding cytokinesis. We focus on cytokinesis in eukaryotes; metazoans, to be more specific. We begin with examples of self-organised dynamics in bacterial cell division.

There are two main questions that appear persistently while discussing cytokinesis. First, what decides the site of the cell cleavage? Second, how are the forces necessary for the cleavage generated?

1.1 CYTOKINESIS IN BACTERIA

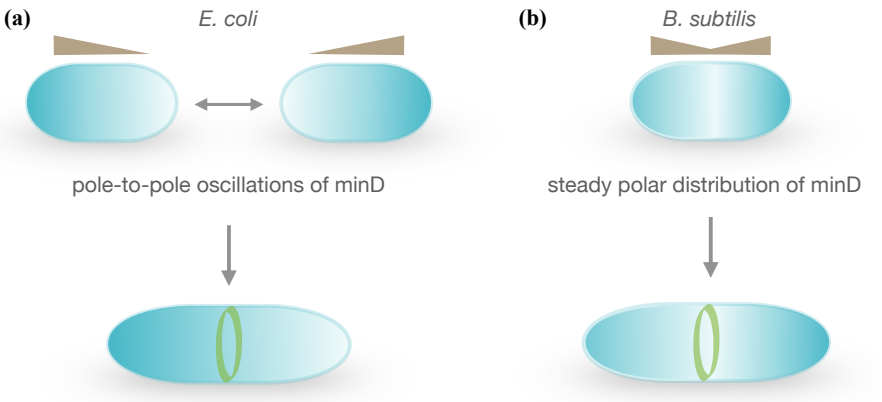

Figure 1.1: In bacteria, two clear examples of reaction-diffusion driven mechanisms for cytokinesis site specification exist. **(a)** In *E. coli*, pole-to-pole oscillations of the protein minD suppress the localisation of cytokinetic proteins at the poles, leading to an effective localisation in the middle. **(b)** On the other hand, minD forms a stable pattern in the cell with two maxima at the poles, leading to specification of the cytokinetic ring in the middle of the cell.

The mechanisms behind cytokinesis site specification can be different for different bacterial species; however, an underlying theme is that spatiotemporal gradients of specific proteins can activate or inhibit the formation of filamentous structures that drive cytokinesis, primarily the FtsZ proteins, to localise at the division site. It is not obvious how the FtsZ filaments generate the forces necessary to deform the membrane. The current view on this matter is the following: once assembled and linked to the membrane, the FtsZ filaments undergo continuous polymerisation and depolymerisation from two extreme ends. An effective reduction in the length constricts the diameter of the filamentous helix, pulling the membrane inwards [Haeusser and

Margolin, 2016]. Note that this mechanism of force generation on the cell surface to divide contrasts with eukaryotes, an issue to which we shall return later in the chapter. Turning our attention back to site specification in bacterial cytokinesis; prominent examples are that of *E. coli* and *B. subtilis* where the distribution of the Min family proteins on the cell poles causes local inhibition of FtsZ formation and therefore localises it towards the centre of the cell [Raskin and De Boer, 1999; Levin et al., 1999]. In *E. coli*, the effective attachment-detachment dynamics of the MinD and MinE proteins to the membrane and the differences in their diffusion rates in the cytoplasm give rise to an effective Turing like instability [Turing, 1952], which can self organise to give rise to the pole-to-oscillations [Howard et al., 2001; Kruse, 2002]. These pole-to-pole oscillations (See Figure 1.1 **(a)**) give rise to an effective time-averaged profile of the Min proteins with is maximum at the poles and minimum at the centre of the cell. In contrast, as shown in Figure 1.1 (**b**), the spatial profile of these inhibitory proteins seems to be non-oscillatory in *B. subtilis*. However, recent work suggests that the molecular interactions of these proteins is similar to that in *E. coli*, and their dynamics can be modelled as a dynamic steady-state arising from a reaction-diffusion system [Feddersen et al., 2021], which is then read-out by the FtsZ proteins to localise a cytokinetic ring that physically separates the two cells. Note that at the length scales of $\sim 1\,\mu$m, as in the case of both the examples above, it is possible to organise intracellular structures on the timescales of $10^1 - 10^2$ s relying solely on diffusive transport. However, as much larger eukaryotic cells emerged in the course of evolution, their ability to change shape, to divide (and, to migrate), posed novel challenges that cannot be solved by diffusive transport alone.

1.2 ENERGETIC AND TRANSPORT CONSTRAINTS IN EUKARYOTIC CELLS

Energy production in bacterial cells is restricted to the membrane, which naturally leads to the energy budget of the cell to scale with its surface area. On the other hand, the energetic requirements of the cell (for maintenance and growth), are typically understood to scale with its volume [Lane and Martin, 2010]. For simplicity, if we consider a spherical cell, this demand-to-budget ratio is expected to scale as R^3/R^2, where R is the cell radius. This specific physiology is, therefore, restricted by its surface area to volume ratio, since beyond

Energetic considerations

a threshold size, the energetic demands will always overwhelm the energy production apparatus. The emergence of chloroplast and mitochondrial symbiosis allowed eukaryotic cells to circumnavigate this problem by a drastic change in the cell physiology, thereby allowing the "storage" of the energy producing apparatus more compactly, allowing the much bigger eukaryotic cells to emerge and is therefore considered one of the most important transitions in evolution [Smith and Szathmary, 1997]. However, circumventing the energetic bottleneck is not enough, as a size increase in cells during evolution lead to another fundamentally different challenge: transport.

Thermal versus active transport

The size of the region which can be accessed by diffusion in a timescale t scales sublinearly with time, as $\sim \sqrt{t}$, to be precise. For a typical protein, the diffusion constant turns out to be $D \approx 1\,\mu\text{m}^2/\text{s}$ [Milo et al., 2010]. The typical timescale for cytokinesis of a eurkaryotic cells is $\sim 10^2$ s. If cytokinetic patterns were to arise from diffusive transport mechanisms, this would be possible only for cells of sizes less than $\sim 10\,\mu$m. On the other hand, *active* transport driven molecular motor proteins have typical translocation speeds of $v \approx 1\,\mu\text{m}/\text{s}$. As such, beyond length scales of order $D/v \sim 5\mu$m, active transport will always dominate diffusive transport [Howard et al., 2011]. Notably, the sizes of eukaryotic cells range from $10^1 - 10^3\,\mu$m. It is therefore not a surprise that eukaryotic cells arose not only with their physiological novelty of endosymbiotic energy production, but also with a diverse array of motor proteins [Koonin, 2010]. These motor proteins actuate on filamentous structures using energy from adenosine triphosphate (ATP) hydrolysis, and thereby generate active movement [Howard, 2001]. In plant cells, for example, the construction of a new cell wall following mitosis is achieved through kinesin mediated active transport [Strompen et al., 2002; Smith, 2002].

1.3 CYTOKINESIS IN METAZOANS

We now turn to cytokinesis in animal cells. Lacking a cell wall, they show remarkable changes in their geometry as they deform and cleave to give rise to daughter cells. A fundamental question thus arises: how do these cells harness active forces to divide into two? What are the general features that characterise this method of cell division? Is the highly dynamical geometry merely an outcome of these active forces, or does it feed back and affect the very forces that caused it to change?

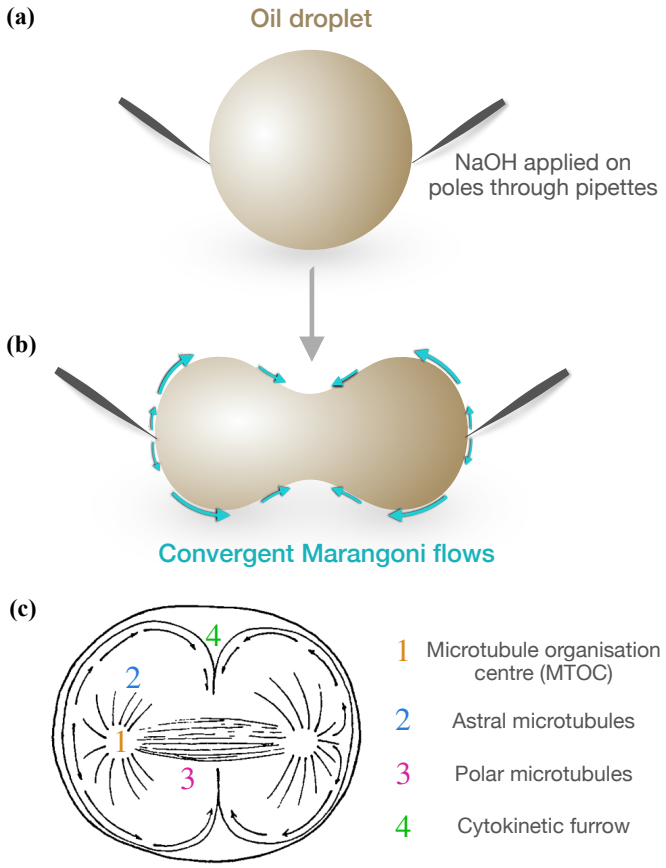

Figure 1.2: The *other* oil-droplet experiment. **(a)** Stimulated Marangoni flows from surface tension gradients using NaOH at the opposing poles leads to destabilisation of an oil droplet. **(b)** The resultant convergent flows eventually drive shape changes in the droplet, resulting in its division. **(c)** Strikingly similar convergent flows were also observed by Josef Spek during cell division in *Rhabditis dolichura* embryos. The panel here shows the mitotic spindle, cytokinetic furrow, and convergent flows. Panel **(c)** reproduced with permission, from J. Spek, *Archiv für Entwicklungsmechanik der Organismen* (1918) [Spek, 1918] ©Springer Nature BV.

Animal cells are *soft*. Experimental measurements report stiffness values in the range of $\sim 10^{-1} - 10^{1}$ kPa [Wu et al., 2018]. As such, initial ideas about animal cells considered them as fluid droplets. Therefore, one could anticipate surface tension differences to possibly destabilise the initial cell geometry and cause it to divide. Support for this hypothesis first emerged in the form of experiments on oil droplets, shown in Figure 1.2 **(a-b)**, where an induced surface tension gradient using NaOH on opposing poles of the droplet caused convergent flows. These flows, directed away from the poles, deformed the droplet to form a furrow-like shape, and eventually cleave into two droplets [McClendon, 1912]. Notably, similar convergent flows

were also reported in a host of different embryos undergoing cytokinesis, including the nematode *Rhabditis dolichura* embryos shown in Figure 1.2 **(c)** [Spek, 1918].

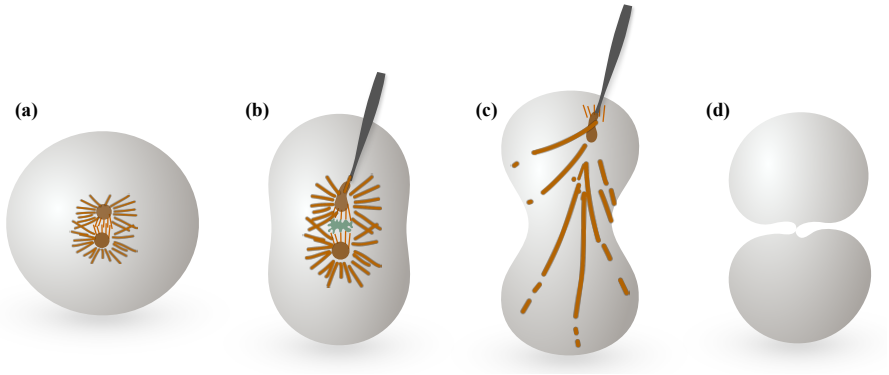

Figure 1.3: Schematic showing the experiment on sea urchin embryos by Y. Hiramoto.

The segregation of the duplicated genetic material occurs concomitant with these geometric shape changes. This segration is primarily achieved by the mitotic spindle, visible in Figure 1.2 **(c)** as the two-lobed structure inside the cell. The cytoskeletal filaments crucial for the formation and stability of the mitotic spindle are microtubules.

The mitotic spindle

These are polymeric filaments made of tubulin subunits [Alberts et al., 2022], and are highly stiff at the length scale of a eukaryotic cell [Howard, 2001]. These filaments, emanating from the microtubule organising centre (MTOC) are broadly classified into polar filaments (responsible for the segregation of chromosomes) and astral filaments which radiate outwards towards the cell membrane. An alternate hypothesis to surface tension gradients driving shape changes in cytokinesis was that astral microtubules generate the necessary forces to pull the furrow inward as the MTOCs move apart to segregate the chromosomes. This hypothesis was first tested using colchicine to perturb the microtubules in sea urchin embryos. Treatment with colchicine at the appropriate time (mid-anaphase, when the chromosomes have separated), showed that the cell continued to divide normally despite the complete disappearance of the spindle [Swann and Mitchison, 1953]. A more direct, physical evidence was to follow from an experiment where the spindle was pulled out of a dividing sea urchin (*Clypeaster japonicus*) embryo using a micropipette. As seen in the time sequence in Figure 1.3, the embryo is able to divide normally despite the strong perturbation of its position and the eventual removal of the spindle [Hiramoto, 1956]. Note that in both of these experiments, *timing* is of extreme importance. The disruption of the

Mitotic spindle is dispensable for cytokinesis completion

spindle using colchicine, or its direct removal using a micropipette, both result in failure of cytokinesis. We now know that the astral microtubules are actually responsible for localising myosin around the cytokinetic furrow [Pollard and O'Shaughnessy, 2019]. This really points to the idea that the spindle (and astral microtubules originating therein) act as a spatiotemporal trigger for cytokinesis. Once the appropriate initial conditions are met, mechanical forces arising from the cell surface are sufficient to deform the furrow, resulting in the cleavage of the mother cell.

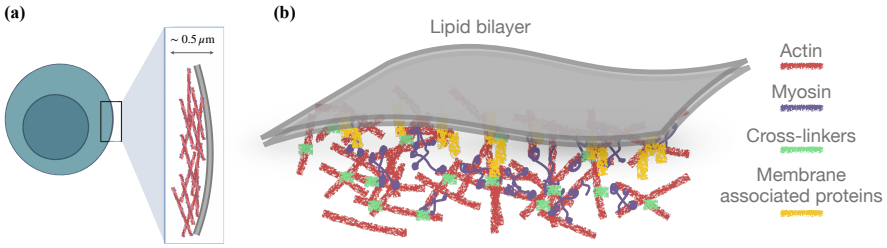

Figure 1.4: (a) The actomyosin cortex is a thin layer setting near the cell surface. Roughly $\sim 0.5\,\mu$m in thickness, but can be up to $1\,\mu$m. (b) The main constituents are actin filaments, myosin motor proteins, and cross linkers and other membrane associated proteins. Due to its small thickness compared to the cell size, for studying patterns at the scale of cells, the cortex can be assumed to be a two-dimensional material.

Given the above experimental findings, the hypothesis that spatial gradients in cell surface tension can drive shape changes during cytokinesis becomes quite plausible. However, at the time of these findings, it was not clear how surface tension gradients necessary for cell division are generated [Mabuchi, 1986]. Subsequent research revealed the molecular constituents that generate *active* forces on the cell surface. It soon became clear that there exists organised filamentous structures on the cell surface at the onset of cytokinesis [Schroeder, 1968; Arnold, 1969]. The discovery that these filaments were polymers of the protein actin also followed soon after [Perry et al., 1971; Schroeder, 1973]. These actin filaments, with the associated myosin motor proteins proved to be necessary for the completion of cytokinesis [Schroeder, 1970, 1973; Mabuchi and Okuno, 1977; Maupin and Pollard, 1986; Mabuchi, 1986]. According to our current understanding, the cortex associated with the cell membrane, is a network of actin filaments, myosin motor proteins and cross linkers [Pollard and O'Shaughnessy, 2019; Alberts et al., 2022], driven out of thermodynamic equilibrium owing to the chemical fluxes converted into mechanical forces [Jülicher et al., 1997]. This *actomyosin cortex* is the cytoskeletal meshwork re-

Molecular drivers of cytokinesis

sponsible for force generation on the cell surface. The cortex is at least an order of magnitude thinner than the size of a typical cell [Salbreux et al., 2012], and is under constant material exchange with the cytoplasm on the timescales of $\sim 10\,\mathrm{s}$ [Mayer et al., 2010; Saha et al., 2016]. These facts, summarised in Figure 1.4, allow us to treat the actomyosin cortex as a two-dimensional material.

Actomyosin cortex as an active layer

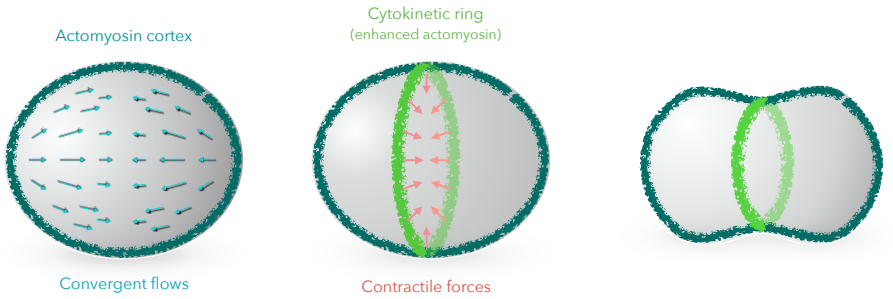

Figure 1.5: At the onset of cytokinesis, cortical flows generate a ring of increased concentration of myosin and other cytoskeletal molecules, generating localised contractile forces which subsequently lead to formation of the cytokinetic furrow

Our current understanding of the emergent dynamics of cytokinesis, (Figure 1.5), is the following: at the early stages, gradients in the concentration of myosin motor proteins are set up due to signals from the mitotic spindle. The positive ends of the astral microtubules orient towards the furrow region, causing a localised activation of the Rho pathway leading to higher concentration of myosin motor proteins on the cell surface [Pollard and O'Shaughnessy, 2019]. Due to the active nature of motors, these concentration gradients then generate gradients in stress (or *tension*, if treated as a two-dimensional surface), giving rise to convergent flows. The same forces concomitantly change the shape of the cell, generating a furrow which constricts to give rise to two daughter cells. Owing to the location of the furrow and the dynamics of advective flows preceding cytokinesis, there can be additional asymmetries can arise during cell division, giving rise to differences in the sizes and/or the distribution of certain proteins.

1.4 EMBRYONIC CELL DIVISIONS: THE INHERITANCE OF BROKEN SYMMETRIES

During embryonic development, a single cell must proliferate to give rise to an immense diversity of cells, which then specialise and collectivise to become specific organs and tissues [Wolpert et al., 2015]. In

addition, there must be continuous supply of new cells for the maintenance and homeostasis of adult organisms. This diversification is primarily driven through *asymmetric cell divisions*, where the two cells *inherit* distinct morphological and chemical properties upon division [Knoblich, 2001].

A prominent example of such an asymmetry is the first embryonic division in *C. elegans*. An initially homogenous distribution of the PAR-2 and PAR-6 proteins on the cell surface is perturbed by sperm entry in the oocyte, and segregates into distinct spatial domains (Figure 1.6) [Munro and Bowerman, 2009]. This asymmetry not only defines the germline cell and somitic cell lineages in the successive cell divisions, but also establish the anterior-posterior axis of the organism. A primary requirement for cell polarity is the existence of multiple locally stable (patterned) states [Trong et al., 2014]. An external signal can then trigger the system to transition from one of these stable (unpolarised) states to another stable (polarised) state. In the *C. elegans* zygote, this signal is delivered by the MTOC associated with male pro-nucleus which triggers large-scale cortical flows that segregate the PAR proteins [Goehring et al., 2011; Gross et al., 2019]. This general principle, known as guided self-organisation, could possibly also underlie cytokinesis, as evident by the observation of the spindle acting as trigger for the initiation of surface flows and being completely dispensable at later stages. We will not discuss this asymmetry further in this thesis. Interestingly, there exist other aspects of asymmetry in *cytokinetic ingression* that we address next.

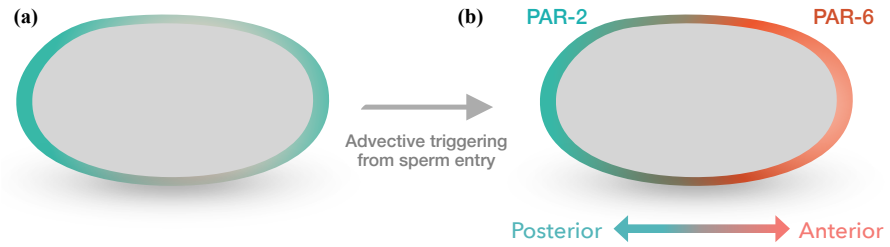

Figure 1.6: The PAR system in the *C. elegans* embryo establishes the anterior-posterior axis before the first cell division

1.5 ASYMMETRIES DURING CYTOKINETIC INGRESSION

As the cell surface deforms and the cytokinetic furrow deepens to separate the prospective daughter cells, this deformation itself can be asymmetric; i.e., the furrow ingression can be in a delayed manner, or

at different speeds in different regions of the cytokinetic ring. This asymmetry is especially pronounced in large embryos, as seen in the comb jelly *B. ovata* shown in Figure 1.7 **(a)** where the ingression seems almost *unilateral* [Rappaport, 1996].

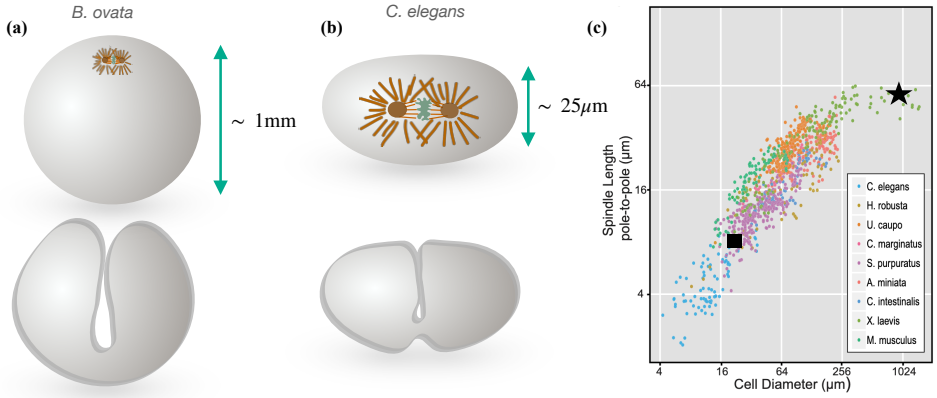

Figure 1.7: Asymmetric cytokinesis can occur across species, and do not require the localisation of a smaller spindle. **(a)** Asymmetric ingression in the comb jelly *B. ovata* embryo, note the difference in relative sizes of cell and spindle in both the embryos.**(b)** shows the asymmetric ingression of cytokinetic furrow in *C. elegans*. **(c)** The spindle size in mitotic cells scales up to a threshold of $\sim 200\,\mu$m, beyond which the cells have a much smaller spindle, which is located very close to the cell surface as in **(a)**. The approximate average morphology for these two embryos is labelled with black symbols; ★ corresponds to *B. ovata* and ■ corresponds to *C. elegans*. Panel **(c)** is adapted with permission from Crowder *et al., Curr. Biol* (2015) [Crowder et al., 2015] ©Elsevier.

Early studies on cytokinesis were performed on embryos of marine animals, chosen for their large size and ease of experimentation. These cells commonly have a proportionately smaller spindle, which is localised towards the embryo surface. One would then expect a smaller region of high Rho activity on the surface, which could then lead to asymmetric flows and ingression. As such, we might expect asymmetric ingression to be restricted to cells which have a mismatch in the spindle size compared to the cell size. However, in *C. elegans* embryos, cytokinesis proceeds in a similar, highly asymmetric manner, while cell and spindle sizes are comparable, and the spindle seems to be positioned symmetrically [Maddox et al., 2007].

Spindle morphologies scale with cell sizes across the animal kingdom, but only up to a threshold of $\sim 200\,\mu$m. In Figure 1.7 **(c)**, we show results from quantitative morphological measurements of spindle and cell sizes [Crowder et al., 2015], where a saturation of the spindle sizes can clearly be observed. The two examples we have

discussed in this section, while showing asymmetric ingression, lie on either extremes of this threshold. This suggests that a localised signal is possibly not a necessary requirement for driving this asymmetry in ingression.

With this background on asymmetric ingression, we ask two related questions. First, what physical principles drive this asymmetry? Second, since this asymmetry is also an aspect of the *geometry* of the cell as it deforms to divide, could the physical principles that drive cytokinesis itself also give naturally rise to this asymmetry? If the answer to the second question is in the positive, asymmetric cytokinesis must be very prevalent. This indeed seems to be the case, as it is observed in diverse cells well below the $\sim 200\,\mu$m threshold [Bourdages et al., 2014]. Thus, our aim in this thesis is to understand the correlation between the physical mechanisms that underlie cytokinesis, and ask if same mechanisms underlie asymmetric ingression during cytokinesis.

1.6 OVERVIEW OF THE THESIS

To summarise the discussion above, we view cytokinesis as an interplay between mechanical stresses on the cell surface, the flows resulting from their gradients, the spatial patterns of force-generating molecules, and the geometry changes that occur simultaneously (Figure 1.8).

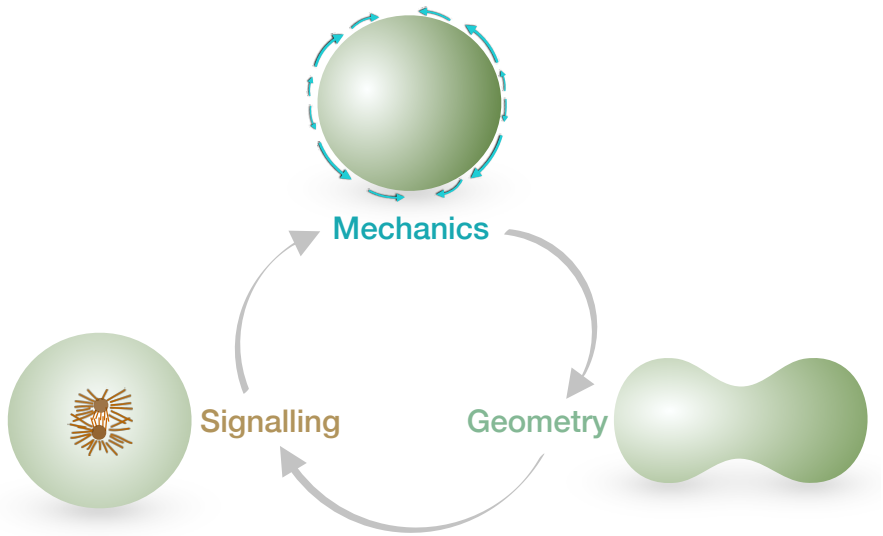

Figure 1.8: Animal cell cytokinesis arises from feedback between signalling, mechanics, and dynamical geometry.

Formally, we will develop coarse-grained active hydrodynamic equations of the actomyosin cortex, and couple them to dynamical geometry. These hydrodynamic equations for the cortex and the kinematic equations for evolving surfaces, are highly non-linear. Exact analytical solutions are, therefore, highly unlikely. As such, we will have to develop appropriate numerical techniques to solve them. Mathematically, this involves solving partial differential equations for concentrations and flow-fields on arbitrary and dynamical geometries. The problem is non-trivial since the deformation of the geometry is specified by quantities which are themselves evolving on that geometry. In other words, we view the dynamical cell shape during cytokinesis as the *geometrodynamics of active surfaces*. Moreover, though these equations can be formulated using intrinsic coordinates, they can seldom be solved due to the presence of coordinate singularities.

In **Chapter 2**, we develop the geometry of curved surfaces embedded in the three-dimensional ambient space. We also formulate methods to perform differential calculus of fields defined on this evolving geometry using only ambient coordinates. Finally, we derive kinematic equations that describe the evolution of geometrical quantities associated with the surface.

In **Chapter 3**, we set up a theory for the actomyosin cortex, treating it as an active fluid. We then study the dynamics of aemergent ctive mechanochemical patterns on curved *static* surfaces. We find that active patterns are highly sensitive to the underlying geometry, and localise on regions on different curvatures depending on the physical parameters. On surfaces shaped like a peanut (which has regions of negative Gaussian curvature), the active fluid self-organises to generate convergent flows, and a ring of myosin pattern in the furrow-like region.

In **Chapter 4**, we study spontaneous patterns that emerge from the geometrodynamics of active surfaces. Surprisingly, we find like cytokinesis-like dynamics of geometry, flows, and concentration fields can emerge spontaneously. We then quantitatively compare this dynamics with cytokinesis in the embryo of the nematode worm *C. elegans*. We find that our theory naturally predicts universal quantitative features of cytokinesis that have been observed across multiple species. We then write an approximate theory relying solely on the feedback between dynamical geometry and the concentration changes seen during the contraction of the cytokinetic ring. We find the predictions of this approximate theory agree with both the numerical solutions of the full theoretical problem, and experimental measurements in

the embryo. Finally, we show that asymmetric cytokinesis also arises naturally in our theory. Furthermore, our theory predicts that the dynamics of asymmetric ingression correlated with the ingression rate of the cytokinetic furrow. This is also quantitatively seen in the experiments.

In **Chapter 5**, we conclude by discussing some drawbacks and open questions that remain. We then attempt to frame our results in the broader context of cellular and embryonic physiology, and end with an evolutionary outlook.

2

KINEMATICS OF EMBEDDED SURFACES

The discussions in the previous chapter emphasized the importance of dynamical geometry in eukaryotic cell division. In this chapter, we develop the extrinsic differential geometry of time-evolving two-dimensional surfaces embedded in the ambient three-dimensional space. The equations governing the spatiotemporal evolution of the geometrical quantities, such as the surface normal and curvature, as well as physical fields defined on the surface are highly nonlinear in nature. With an aim to solve these equations numerically, we recast these dynamical equations in a manner suited to an implementation using the finite element method.

2.1 THE INTRINSIC AND AMBIENT VIEW OF THE SURFACE

Consider a two-dimensional surface $\mathcal{M}$ embedded in $\mathbb{R}^3$. We describe $\mathcal{M} \subset \mathbb{R}^3$ by specifying a smooth map $\boldsymbol{\phi} : U \to \mathcal{M}$ where $U \subset \mathbb{R}^2$. Parametrising U with coordinates s^α, the map $\boldsymbol{\phi}$ gives the Cartesian coordinates $x^i \in \mathbb{R}^3$ of the point corresponding to $\{s^1, s^2\} \in U$ as shown in Figure 2.1. Thus $\boldsymbol{\phi}(s^1, s^2) = \phi^i(s^1, s^2)\,\hat{\mathbf{e}}_i$, where $\hat{\mathbf{e}}_i$ are the Cartesian basis unit-vectors in $\mathbb{R}^3$, ϕ^i are the components of the map $\boldsymbol{\phi}$, and repeated indices are summed over following the *Einstein summation convention*. We will use Greek letters $\alpha, \beta, \ldots$ to index coordinates and vector components in U, and Latin indices $i, j, \ldots$ to refer to coordinates and vector components in the ambient space $\mathbb{R}^3$. We will assume that map $\boldsymbol{\phi}$ is locally invertible.

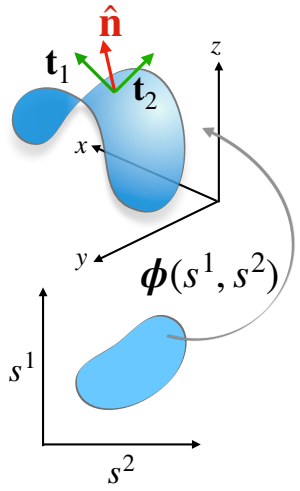

Figure 2.1: The embedded surface as a map. Depicting the local tangent vectors (green) and the unit normal vector (red).

At a point $\mathbf{p}$ on the surface, the tangent vectors $\mathbf{t}_\alpha$ are obtained by:

$$\mathbf{t}_\alpha = \frac{\partial \boldsymbol{\phi}}{\partial s^\alpha} = s^i_\alpha\, \hat{\mathbf{e}}_i. \tag{2.1}$$

The *shift tensor* $\mathbf{s}$ with components $s^i_\alpha \equiv \partial \phi^i / \partial s^\alpha$ in the above equation is the Jacobian of the map $\boldsymbol{\phi}$ [Waxman, 1984; Kreyszig, 1991; Grinfeld et al., 2013]. It is easy to see why the term shift is used. Let $\mathbf{v}$ be a

tangent vector to the surface $\mathcal{M}$ at a point $\mathbf{p}$. We can write $\mathbf{v}$ either in terms of the tangent vectors $\mathbf{t}_\alpha$ or in terms of $\hat{\mathbf{e}}_i$ as:

$$\mathbf{v} = v^\alpha \, \mathbf{t}_\alpha = v^\alpha \, s^i_\alpha \, \hat{\mathbf{e}}_i = v^i \hat{\mathbf{e}}_i,$$

where we have used (2.1) and defined the Cartesian components $v^i = s^i_\alpha v^\alpha$. Thus, the shift tensor $\mathbf{s}$, represented by a 3×2 matrix, allows us to *lift* a 2×1 vector, with components v^α, into a 3×1 vector, with components v^i. This lifting process will work for arbitrary tensors.

The $\mathbf{t}_\alpha$ form a basis for the tangent vector space $T_\mathbf{p}\mathcal{M}$ at the point $\mathbf{p}$. The corresponding *dual vector space* $T^*_\mathbf{p}\mathcal{M}$ has $\mathbf{t}^\alpha$ as the basis vectors with $\mathbf{t}^\alpha(\mathbf{t}_\beta) = \delta^\alpha_\beta$, where δ^α_β represents the Kronecker-delta. Further, just like the $\hat{\mathbf{e}}_i$ form a basis for the tangent vector space $T_\mathbf{p}\mathbb{R}^3$ at the point $\mathbf{p}$, the dual vectors $\hat{\mathbf{e}}^i$ form a basis for the cotangent vector space $T^*_\mathbf{p}\mathbb{R}^3$. The shift tensor $\mathbf{s}$ with components s^i_α defined above is an element of $T^*_\mathbf{p}\mathcal{M} \otimes T_\mathbf{p}\mathbb{R}^3$, where $\otimes$ is the tensor product. It is thus natural to define another shift tensor $\mathbf{s}^*$ with component $s^\alpha_i \equiv \partial s^\alpha / \partial \phi^i$ which is an element of $T^*_\mathbf{p}\mathbb{R}^3 \otimes T_\mathbf{p}\mathcal{M}$. It should be noted that, by definition, $s^\alpha_i s^i_\beta = \delta^\alpha_\beta$. Analogous to (2.1), we have $\hat{\mathbf{e}}_i = s^\alpha_i \, \mathbf{t}_\alpha$, and for the dual vectors $\mathbf{t}^\alpha = s^\alpha_i \, \hat{\mathbf{e}}^i$ and $\hat{\mathbf{e}}^i = s^i_\alpha \, \mathbf{t}^\alpha$. However, this only works for vectors that are tangent to the surface $\mathcal{M}$ since the tangent vector space $T_\mathbf{p}\mathcal{M}$ is a subspace of $T_\mathbf{p}\mathbb{R}^3$ at every point $\mathbf{p}$.

The metric tensor $\mathbf{g}$ for the surface $\mathcal{M}$ is

The metric tensor

$$\mathbf{g} = g_{\alpha\beta} \, \mathbf{t}^\alpha \otimes \mathbf{t}^\beta, \tag{2.2}$$

where the components $g_{\alpha\beta}$ are given by $g_{\alpha\beta} = \mathbf{t}_\alpha \cdot \mathbf{t}_\beta$ where $\cdot$ is the scalar product of vectors in $\mathbb{R}^3$.

The identity operator in the tangent space $T_\mathbf{p}\mathcal{M}$ is $\mathbf{I}_2 = \mathbf{t}_\alpha \otimes \mathbf{t}^\alpha$ while the corresponding quantity in the tangent space $T_\mathbf{p}\mathbb{R}^3$ is $\mathbf{I} = \hat{\mathbf{e}}_i \otimes \hat{\mathbf{e}}^i$ in $\mathbb{R}^3$. To find a relationship between these two operators, we consider the unit-normal vector $\hat{\mathbf{n}}$ at every point on the surface.

At each point $\mathbf{p}$ on the surface $\mathcal{M}$, we construct the unit-normal vector $\hat{\mathbf{n}}$ given by:

The unit normal

$$\hat{\mathbf{n}} = \frac{\mathbf{t}_1 \times \mathbf{t}_2}{|\mathbf{t}_1 \times \mathbf{t}_2|}, \tag{2.3}$$

where $\times$ represents the cross product in $\mathbb{R}^3$. The subspace of $T_\mathbf{p}\mathbb{R}^3$ spanned by $\hat{\mathbf{n}}$ is one-dimensional, and hence the dual of $\hat{\mathbf{n}}$ can be iden-

tified with itself. Note also that the direct sum of this one-dimensional subspace and $T_{\mathbf{p}}\mathcal{M}$ is the full tangent space $T_{\mathbf{p}}\mathbb{R}^3$.

Consider an arbitrary vector $\mathbf{v}$, not necessarily tangential to $\mathcal{M}$, defined at the point $\mathbf{p}$. This vector can be split into its normal and tangential components as $\mathbf{v} = v_\perp \hat{\mathbf{n}} + \mathbf{v}_\parallel$, where $v_\perp = \hat{\mathbf{n}} \cdot \mathbf{v}$, and

$$\mathbf{v}_\parallel = \mathbf{v} - v_\perp \hat{\mathbf{n}} = (\mathbf{I} - \hat{\mathbf{n}} \otimes \hat{\mathbf{n}}) \cdot \mathbf{v} = \mathbf{P} \cdot \mathbf{v},$$

where we identify the tangential projection operator

$$\mathbf{P} \equiv \mathbf{I} - \hat{\mathbf{n}} \otimes \hat{\mathbf{n}}. \tag{2.4}$$

It is easy to show that $\mathbf{P} \cdot \hat{\mathbf{n}} = 0 = \hat{\mathbf{n}} \cdot \mathbf{P}$ and $\mathbf{P} \cdot \mathbf{v}_\parallel = \mathbf{v}_\parallel$. The last relation implies $\mathbf{P} \cdot \mathbf{P} = \mathbf{I}$.

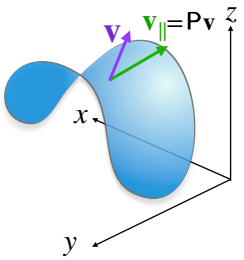

Figure 2.2: Projection of the vector field on the surface.

Now

$$\mathbf{v}_\parallel = \mathbf{I}_2 \cdot \mathbf{v}_\parallel = (\mathbf{t}_\alpha \otimes \mathbf{t}^\alpha) \cdot \mathbf{v}_\parallel = (s^i_\alpha s^\alpha_j \, \hat{\mathbf{e}}_i \otimes \hat{\mathbf{e}}^j) \cdot \mathbf{v}_\parallel$$

This implies

$$\mathbf{P} = \mathbf{t}_\alpha \otimes \mathbf{t}^\alpha = s^i_\alpha s^\alpha_j \, \hat{\mathbf{e}}_i \otimes \hat{\mathbf{e}}^j = \mathbf{s} \cdot \mathbf{s}^*, \tag{2.5}$$

where the projection operator has the components

$$\mathsf{P}^\alpha_\beta = \delta^\alpha_\beta, \qquad \mathsf{P}^i_j = s^i_\alpha s^\alpha_j. \tag{2.6}$$

Notice that we can also write $\mathbf{P} = \mathbf{s} \cdot \mathbf{s}^*$, which leads to $\hat{\mathbf{n}} \cdot \mathbf{s} = 0 = \mathbf{s}^* \cdot \hat{\mathbf{n}}$. From the above, and noting that $\mathbf{I}_2 = g_{\alpha\beta} \, \mathbf{t}^\alpha \otimes \mathbf{t}^\beta$, we realize that the projection operator $\mathbf{P}$ and the metric tensor $\mathbf{g}$ are related to each other via the shift tensors. In other words, the projection operator is the metric tensor of the surface, lifted in the ambient space. Both of these mathematical objects, therefore, are equivalent and contain the same information about the embedded surface [Delfour and Zolésio, 2011].

2.2 TANGENTIAL CALCULUS

Recall that we would like to compute the derivatives of on fields defined on the surface, but using the ambient basis. A natural question, therefore, is how to extend fields in the direction normal to the surface, despite them being restricted on the surface. A mathematically well-posed way is to define the *constant normal extension* of surface fields. Consider any field $f : \mathcal{M} \to \mathbb{R}$. Let d be the signed distance function

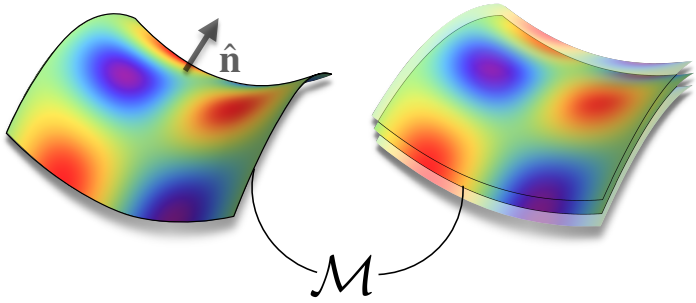

Figure 2.3: A scalar field (represented by the colourmap) on the surface $\mathcal{M}$, with a unit normal vector field $\hat{\mathbf{n}}$. This scalar field can be extended from $\mathcal{M}$ into the ambient space $\mathbb{R}^3$ via a *constant normal extension*. We show this schematically by two surfaces separated by displacements $\pm d\hat{\mathbf{n}}$, above and below $\mathcal{M}$.

from the surface such that $\nabla_3 d = \hat{\mathbf{n}}$ where ∇_3 is the Cartesian gradient operator. Now, let $f_e : \Omega \to \mathbb{R}$ be an extension of the function to the ambient space, such that $\Omega \subset \mathbb{R}^3$ contains all possible deformations of the surface. For a constant normal extension, at any point $\mathbf{p} \in \Omega$, we define the function f_e as:

$$f_e(\mathbf{p}) = f(c(\mathcal{M}, \mathbf{p})),$$

where $c(\mathcal{M}, \mathbf{p})$ refers to the closest point on the surface $\mathcal{M}$ corresponding to $\mathbf{p}$. Now, since f_e is defined in Ω, the ambient gradient ∇_3 is a perfectly well-defined operation. However, by definition, f_e is a *constant* normal extension of the function f, which implies there is no change in this extended field in the normal direction. This clearly implies

Constant normal extension

$$(\nabla_3 f_e) \cdot \hat{\mathbf{n}} = 0.$$

From the definition of the extended function, it is clear that on the surface both the function and its extension coincide: $f_e(\mathbf{p}) = f(\mathbf{p})$ iff $\mathbf{p} \in \mathcal{M}$. Clearly, this construction can be extended in a straightforward manner to all tensor fields on the surface. Note that we need this mathematical construction of constant normal extension to justify the *existence* of fields locally in $\mathbb{R}^3$ around the surface $\mathcal{M}$.

For scalar fields f extended into the ambient space via the constant normal extension, the surface derivative coincides with the Cartesian derivative, i.e.,

$$\nabla f = \nabla_3 f_e. \tag{2.7}$$

However, the definition of such derivatives for more general tensor fields requires some care which we address in the next section. We remark that the definition and existence of tangential derivatives do not depend on the specific manner in which we extend the surface fields into the ambient space [Delfour and Zolésio, 2011].

We now formulate the tangential differential calculus of fields defined on the surface $\mathcal{M}$ but expressed in ambient coordinates. This allows us to compute all derivatives in terms of Cartesian coordinates, without any coordinate singularities, and obtain the appropriate surface derivatives with the applications of enough number of projection operators.

Consider a scalar field $c(\mathbf{x})$ defined on the surface $\mathcal{M}$. We extend $c(\mathbf{x})$ locally into the ambient space $\mathbb{R}^3$ in any suitable manner. Therefore, at each point $\mathbf{p} \in \mathcal{M}$, the Cartesian derivative $\nabla_3 c$ is well defined. The surface derivative is then defined by

$$\nabla c \equiv \mathbf{P} \cdot \nabla_3 c. \tag{2.8}$$

Tangential derivative of a scalar

For a vector field $\mathbf{v}(\mathbf{x})$, the surface derivative is defined by

$$\nabla \mathbf{v} = \mathbf{P} \cdot \nabla_3 \mathbf{v} \cdot \mathbf{P}. \tag{2.9}$$

Tangential derivative of a vector

It can be shown that this definition coincides with the usual covariant derivative of a vector field defined in intrinsic coordinates using a Levi-Civita connection [Delfour and Zolésio, 2011; Renteln, 2014].

2.3 SURFACE CURVATURE AND AMBIENT SHAPE OPERATOR

Given a surface $\mathcal{M} \subset \mathbb{R}^3$ which is specified by a smooth map $\boldsymbol{\phi} : U \to \mathcal{M}$ where $U \subset \mathbb{R}^2$, we can construct the tangent vectors $\mathbf{t}_\alpha$ and the unit-normal vector $\hat{\mathbf{n}}$ to the surface as discussed in the previous sections. The curvature of a surface is measured by the variation of $\hat{\mathbf{n}}$ as move on it. Specifically, the extrinsic curvature tensor $\mathbf{B}$

$$\mathbf{B} = B_{\alpha\beta}\, \mathbf{t}^\alpha \otimes \mathbf{t}^\beta, \tag{2.10}$$

with the components $B_{\alpha\beta}$ given by

$$B_{\alpha\beta} = \mathbf{t}_\alpha \cdot \partial_\beta \hat{\mathbf{n}}, \tag{2.11}$$

where $\partial_\alpha \equiv \partial/\partial s^\alpha$ is a coordinate derivative. $B_{\alpha\beta}$ is a symmetric tensor and has two eigenvalues, k_1, k_2 which are the principal curvatures. The two invariants of the curvature tensor, the trace and determinant

$$\mathcal{H} = \mathrm{Tr}(B_{\alpha\beta}) = k_1 + k_2, \tag{2.12}$$

$$\mathcal{K} = \mathrm{Det}(B_{\alpha\beta}) = k_1\, k_2, \tag{2.13}$$

are the summed curvature $\mathcal{H}$ and the Gaussian curvature $\mathcal{K}$ respectively. Note that $\mathcal{H}$ is an extrinsic quantity while $\mathcal{K}$ is intrinsically defined without reference to any ambient embedding of the surface.

We want to obtain the lift of $\mathbf{B}$ to the ambient space. To do so, we note $\partial_\alpha = s^i_\alpha \partial_i$ and rewrite

$$B_{\alpha\beta} = s^i_\alpha \partial_\beta n_i = s^i_\alpha s^j_\beta (\partial_j n_i).$$

Using this and $\mathbf{t}^\alpha = s^\alpha_i\, \hat{\mathbf{e}}^i$ in (2.10), we get

$$\mathbf{B} = s^i_\alpha s^j_\beta\, (\partial_j n_i)\, s^\alpha_k s^\beta_l\, \hat{\mathbf{e}}^k \otimes \hat{\mathbf{e}}^l = \mathsf{P}^i_k\, \mathsf{P}^j_l\, (\partial_j n_i)\, \hat{\mathbf{e}}^k \otimes \hat{\mathbf{e}}^l,$$

where in the last equality we have used $\mathsf{P}^i_j = s^i_\alpha s^\alpha_j$. Clearly $\partial_j n_i$ are the components of $\nabla_3 \hat{\mathbf{n}}$. Thus $\mathsf{P}^i_k\, \mathsf{P}^j_l\, (\partial_j n_i)$ are the components of a tensor which forms the lift of $\mathbf{B}$ to the ambient space $\mathbb{R}^3$. This motivates us to define the ambient shape operator or the *Weingarten map* [Walker, 2015] as

Shape operator

$$\mathbf{S} \equiv \nabla \hat{\mathbf{n}} = \mathbf{P} \cdot (\nabla_3 \hat{\mathbf{n}}) \cdot \mathbf{P}. \tag{2.14}$$

We can thus compute $\mathbf{S}$ by first computing the Cartesian gradient $\nabla_3 \hat{\mathbf{n}}$ and then using the projection operators appropriately.

The shape operator $\mathbf{S}$ has a non-trivial null vector: $\hat{\mathbf{n}}$, i.e., $\mathbf{S} \cdot \hat{\mathbf{n}} = 0$. The three eigenvalues of $\mathbf{S}$ are then k_1, k_2, k_3, where the first are the principal curvatures of the surface mentioned earlier and $k_3 = 0$. In terms of $\mathbf{S}$, the summed and Gaussian curvatures of the surface as

Curvatures

$$\mathcal{H} = \mathrm{Tr}(\mathbf{S}) = k_1 + k_2, \tag{2.15}$$

$$\mathcal{K} = [\mathrm{Tr}(\mathbf{S})]^2 - \mathrm{Tr}(\mathbf{S}^2) = k_1\, k_2 + k_2\, k_3 + k_1\, k_3 = k_1\, k_2. \tag{2.16}$$

It is clear that the third invariant, $\mathrm{Det}(\mathbf{S}) = k_1 k_2 k_3 = 0$. Furthermore, from the definition of $\mathbf{S}$, it is clear that $\mathbf{P} \cdot \mathbf{S} = \mathbf{S} = \mathbf{S} \cdot \mathbf{P}$.

A surface is completely specified, up to global translations and rotations, if the unit-normal $\hat{\mathbf{n}}$ (or equivalently the projector $\mathbf{P}$) and the shape operator $\mathbf{S}$ are specified. This, therefore, completes the

ambient space definitions of the various geometrical quantities needed to specify the surface $\mathcal{M}$. We are now in a position to define the geometry of the surface and also to construct the tangential derivatives of fields defined on it. We now turn our attention to deriving the dynamical equations for these geometrical quantities when the surface $\mathcal{M}$ is deforming in time.

2.4 KINEMATICS OF MOVING SURFACES

Our motivation for considering deformable surfaces in this thesis is to study the deformation of the cell surface during cytokinesis. These shape changes are predominantly governed by the dynamics of the effective two-dimensional surface composed of the actomyosin cortex and the lipid bilayer membrane. The bilayer membrane behaves as fluid membrane since the lipids contained in it can diffuse freely in the local tangent plane. The membrane resists bending shape changes for out of plane deformations. Similarly, the cortex flows like a viscous fluid on timescales longer compared to its viscoelastic relaxation timescale. We will discuss the physics of the cortex in the next chapter. For now, it suffices to underscore the idea that we should consider fluid surfaces that do not resist in-plane shear deformations and change shape only by movements along the local normal direction.

Consider a velocity field $\mathbf{v}$ defined on a fluid surface $\mathcal{M}$. Only the normal component of the velocity $\mathbf{v}_\perp = (\mathbf{v}\cdot\hat{\mathbf{n}})\,\hat{\mathbf{n}}$ contributes to the deformation of the surface. A material point on $\mathcal{M}$ specified by the position vector $\boldsymbol{\phi}(s^1, s^2)$ on $\mathcal{M}$ moves according to

$$\frac{d\boldsymbol{\phi}}{dt} = \mathbf{v}_\perp. \tag{2.17}$$

Evolution of a fluid surface

When constructing the constant normal extension of surface fields, we considered the signed distance function $d(\mathbf{x}, t)$ where $\mathbf{x} \in \Omega \subset \mathbb{R}^3$ is around the surface. The position vector $\mathbf{p}(\mathbf{x}, t)$ of the point closest to $\mathbf{x}$ on the surface is $\mathbf{p}(\mathbf{x}, t) = \mathbf{x} - d(\mathbf{x}, t)\,\hat{\mathbf{n}}$. This implies that the rate at which the signed distance function d changes is

$$\frac{\partial d}{\partial t} = -v_\perp$$

To get an equation for the unit-vector $\hat{\mathbf{n}}$, we note that (i) $\nabla_3 d = \hat{\mathbf{n}}$, (ii) the partial derivatives of d with respect to time and the ambient-space coordinates commute, i.e., $\partial_t \nabla_3 d = \nabla_3 \partial_t d$, and (iii) since $v_\perp$ is a scalar

field, we have $(\nabla_3 v_\perp)\cdot\hat{\mathbf{n}} = 0$ which implies $\nabla_3\hat{\mathbf{n}} = \nabla\hat{\mathbf{n}}$. Taking the spatial derivative of the above equation for d leads us to

Unit normal evolution

$$\frac{\partial\hat{\mathbf{n}}}{\partial t} = -\nabla v_\perp. \tag{2.18}$$

In words, this equation reveals that the unit normal field on a deformable surface changes only when there is a surface variation of the deformation velocity. Equation (2.18) is also known as Thomas equation [Thomas, 1961]. It is now straightforward to derive the equation of motion for the projection operator $\mathbf{P} = \mathbf{I} - \hat{\mathbf{n}}\otimes\hat{\mathbf{n}}$. We get

Projection operator evolution

$$\frac{\partial\mathbf{P}}{\partial t} = \nabla v_\perp\otimes\hat{\mathbf{n}} + \hat{\mathbf{n}}\otimes\nabla v_\perp. \tag{2.19}$$

Before deriving the equation for the ambient curvature tensor $\mathbf{S}$, we need to obtain a few more relations. The evolution for shift tensor is given by [Salbreux and Jülicher, 2017]:

$$\frac{\partial s_\alpha^i}{\partial t} = n^i\partial_\alpha v_\perp + v_\perp B_\alpha^\beta s_\beta^i\,. \tag{2.20}$$

To obtain the time derivative of the shift tensor s_i^α, we write $s_i^\alpha = g^{\alpha\beta}s_\beta^j\delta_{ij}$. Therefore,

$$\begin{aligned}\frac{\partial s_i^\alpha}{\partial t} &= \delta_{ij}\left(s_\beta^j\frac{\partial g^{\alpha\beta}}{\partial t} + g^{\alpha\beta}\frac{s_\beta^j}{\partial t}\right)\\ &= \delta_{ij}\left(-2v_\perp s_\beta^j B^{\alpha\beta} + v_\perp B^{\alpha\gamma}s_\gamma^j + n^j\partial^\alpha v_\perp]\right)\\ &= -v_\perp s_{i\beta}B^{\alpha\beta} + n_i\partial^\alpha v_\perp\end{aligned}$$

where we have used $\partial_t g^{\alpha\beta} = -2v_\perp B^{\alpha\beta}$ [Waxman, 1984]. This gives us the evolution equations of the two shift tensors. Next, we derive another relation that will be useful for further calculations. Consider the definition of the ambient shape operator: $(\mathbf{S})_j^i = s_\alpha^i B_\beta^\alpha s_j^\beta$, we would now like to write the quantity $s_\alpha^i B_\gamma^\alpha B^\gamma s_j^\beta$ purely in terms of ambient quantities. To obtain this, we write:

$$\begin{aligned}s_\alpha^i B_\gamma^\alpha B^\gamma s_j^\beta &= s_\alpha^i\, B_\mu^\alpha\delta_\gamma^\mu B^\gamma\, s_j^\beta\,,\\ &= s_\alpha^i\, B_\mu^\alpha\, g^{\mu\nu}g_{\nu\gamma}\, B^\gamma\, s_j^\beta\,,\\ &= s_\alpha^i\, B_\mu^\alpha\, s_m^\mu s^{m\nu}s_{\nu l}s_\gamma^l\, B^\gamma\, s_j^\beta.\end{aligned}$$

Using the definitions of the geometric quantities, we have $s^i_\alpha\, B^\alpha_\mu\, s^\mu_m = (\mathbf{S})^i_m$, $s^{m\nu} s_{\nu l} = s_{l\nu} s^{\nu m} = (\mathbf{P})^m_l$, and $s^l_\gamma\, B^\gamma\, s^\beta_j = (\mathbf{S})^l_j$. Therefore,

$$(s^i_\alpha B^\alpha_\gamma B^\gamma s^\beta_j)\, \hat{\mathbf{e}}_i \otimes \hat{\mathbf{e}}^j = (\mathbf{S})^i_m (\mathbf{P})^m_l (\mathbf{S})^l_j\, \hat{\mathbf{e}}_i \otimes \hat{\mathbf{e}}^j = \mathbf{S}\cdot(\mathbf{P}\cdot\mathbf{S}) = \mathbf{S}\cdot\mathbf{S}. \quad (2.21)$$

We now turn to the kinematic equation for the ambient curvature tensor (shape operator). Using the definition of the ambient shape operator we can write its time evolution as

$$\frac{\partial \mathbf{S}^i_j}{\partial t} = \underbrace{\frac{\partial s^i_\alpha}{\partial t}\, B^\alpha_\beta\, s^\beta_j}_{\Theta^i_j} + \underbrace{s^i_\alpha \frac{\partial B^\alpha_\beta}{\partial t} s^\beta_j}_{\Phi^i_j} + \underbrace{s^i_\alpha\, B^\alpha_\beta \frac{\partial s^\beta_j}{\partial t}}_{\Xi^i_j}.$$

We will derive the three terms on the right hand side of the equation one at a time. Starting with $\boldsymbol{\Theta}^i_j$, using $\partial_t s^i_\alpha = n^i \partial_\alpha v_\perp + v_\perp\, B^\gamma_\alpha\, s^i_\gamma$ we have

$$\Theta^i_j = (n^i \partial_\alpha v_\perp + v_\perp\, B^\gamma_\alpha\, s^i_\gamma)\, B^\alpha_\beta\, s^\beta_j.$$

From the first term inside the bracket, we get,

$$\begin{aligned} n^i \partial_\alpha v_\perp\, B^\alpha_\beta\, s^\beta_j &= n^i \partial_\mu v_\perp\, \delta^\mu_\alpha\, B^\alpha_\beta\, s^\beta_j \\ &= n^i \partial_\mu v_\perp\, g^{\mu\nu}\, g_{\nu\alpha}\, B^\alpha_\beta\, s^\beta_j \\ &= n^i \partial_\mu v_\perp\, s^\mu_l s^{l\nu}\, s_{\nu m} s^m_\alpha\, B^\alpha_\beta\, s^\beta_j. \end{aligned}$$

The second term inside the bracket, from (2.21), is $v_\perp \mathbf{S}\cdot\mathbf{S}$ in the coordinate free notation. Notice that $\partial_\mu v_\perp\, s^\mu_l = (\nabla v_\perp)_l$ due the action of the shift tensor on the tangential gradient. From the definition of projection operator, $s^{l\nu} s_{\nu m} = s_{m\nu} s^{\nu l} = (\mathbf{P})^l_m$. From the definition of the ambient shape operator, $s^m_\alpha\, B^\alpha_\beta\, s^\beta_j = (\mathbf{S})^m_j$. Combining these facts we can write Θ^i_j in index free notation

$$\boldsymbol{\Theta} = v_\perp \mathbf{S}\cdot\mathbf{S} + (\hat{\mathbf{n}} \otimes \nabla v_\perp)\cdot\mathbf{S}. \quad (2.22)$$

The second term, Φ^i_j, needs the partial time derivative of the (2×2) curvature tensor B^α_β, whose kinematic evolution is given by [Waxman, 1984; Salbreux and Jülicher, 2017]:

$$\frac{\partial B^\alpha_\beta}{\partial t} = -\nabla^\alpha \partial_\beta v_\perp - v_\perp B^\alpha_\gamma B^\gamma_\beta. \quad (2.23)$$

We therefore have

$$\Phi^i_j = s^i_\alpha \left(-\nabla^\alpha \, \partial_\beta v_\perp - v_\perp B^\alpha_\gamma B^\gamma_\beta \right) s^\beta_j .$$

From the first term on the right, we recognise the double derivative of the deformation speed,

$$s^i_\alpha \nabla^\alpha \, \partial_\beta v_\perp s^\beta_j = (\nabla \nabla v_\perp)^i_j . \tag{2.24}$$

For on the second term, using (2.21) again we get $v_\perp \mathbf{S} \cdot \mathbf{S}$. Combining this with (2.24), we can write Φ^i_j in a coordinate free form as

$$\mathbf{\Phi} = -\nabla \nabla v_\perp - v_\perp \mathbf{S} \cdot \mathbf{S}. \tag{2.25}$$

Finally, the last term Ξ^i_j,

$$\Xi^i_j = s^i_\alpha \, B^\alpha_\beta \frac{\partial s^\beta_j}{\partial t} = s^i_\alpha B^\alpha_\beta (-v_\perp s_{j\gamma} B^{\beta\gamma} + n_j \partial^\beta v_\perp) .$$

Relying on (2.21) once again, from the first term inside the bracket, we get $-v_\perp \mathbf{S} \cdot \mathbf{S}$. From the second term inside the bracket, we get:

$$\begin{aligned} s^i_\alpha \, B^\alpha_\beta \partial^\beta v_\perp n_J &= s^i_\alpha \, B^\alpha_\beta \, \delta^\beta_\mu \partial^\mu v_\perp n_j \\ &= s^i_\alpha \, B^\alpha_\beta \, g^{\beta\nu} g_{\nu\mu} \, \partial^\mu v_\perp n_j \\ &= s^i_\alpha \, B^\alpha_\beta \, s^\beta_l s^{l\nu} s_{\nu m} s^m_\mu \partial^\mu v_\perp n_j . \end{aligned}$$

We recognize, $s^i_\alpha \, B^\alpha_\beta s^\beta_l = (\mathbf{S})^i_l$, $s^{l\nu} s_{\nu m} = (\mathbf{P})^l_m$, and $s^m_\mu \partial^\mu v_\perp n_j = (\nabla v \otimes \hat{\mathbf{n}}_\perp)^m_j$. In index free notation

$$\mathbf{\Xi} = \mathbf{S} \cdot (\nabla v_\perp \otimes \hat{\mathbf{n}}) - v_\perp \mathbf{S} \cdot \mathbf{S}. \tag{2.26}$$

Combining (2.22), (2.25), and (2.26), we get

$$\begin{aligned} \mathbf{\Theta} + \mathbf{\Phi} + \mathbf{\Xi} = v_\perp \mathbf{S} \cdot \mathbf{S} &+ (\hat{\mathbf{n}} \otimes \nabla v_\perp) \cdot \mathbf{S} \\ &- \nabla \nabla v_\perp - v_\perp \mathbf{S} \cdot \mathbf{S} \\ &+ \mathbf{S} \cdot (\nabla v_\perp \otimes \hat{\mathbf{n}}) - v_\perp \mathbf{S} \cdot \mathbf{S} \end{aligned} \tag{2.27}$$

The first and the last terms on the right hand of this equation cancel each other, leading to the evolution equation of the ambient shape operator:

Shape operator evolution

$$\frac{\partial \mathbf{S}}{\partial t} = (\hat{\mathbf{n}} \otimes \nabla v_\perp) \cdot \mathbf{S} - \nabla \nabla v_\perp - v_\perp \mathbf{S} \cdot \mathbf{S} + \mathbf{S} \cdot (\nabla v_\perp \otimes \hat{\mathbf{n}}) . \tag{2.28}$$

Note that the second and the third terms are analogous to the evolution of the 2×2 curvature tensor in terms of the intrinsic coordinates (2.23). The first and the last terms arise *purely* because we wished to find the evolution equation of the curvature tensor lifted in the ambient coordinates. Combined with (2.18) and (2.19), it gives us the complete description of the time evolution of relevant ambient geometric quantities given a deformation velocity field $v_\perp \hat{\mathbf{n}}$.

2.5 SUMMARY

In this chapter, we have formulated the extrinsic differential geometry of surfaces embedded in $\mathbb{R}^3$. Our formulation emphasises a coordinate independent perspective and also focuses on suitability for a numerical implementation. Further, we have developed the tangential differential calculus of fields defined on the surface using their Cartesian derivates and appropriate projection operators. Finally, we consider dynamical fluid surfaces and derive the equations for the geometrical descriptors of the surface. In the forthcoming chapters, we employ the geometry of embedded surfaces and their kinematics developed here to first study active patterns on static surfaces and then explore aspects of cell division and the role of geometry therein.

3

ACTIVE PATTERNS ON STATIC CURVED SURFACES

In animal cells, mechanical deformations and structural stability are coordinated by a host of subcellular structures collectively known as the cytoskeleton. The actomyosin cortex, a part of the cellular cytoskeleton, is a thin ($\sim 0.2\,\mu$m [Clark et al., 2013]) meshwork of actin filaments, interspersed with motor proteins and cross-linkers (see Figure 3.1). The actuation of motor proteins by the hydrolysis of ATP manifest, at the coarse-grained level, as an active mechanical stresses generated within this layer. The cortex is in constant turnover – exchange of the surface bound proteins with the cytoplasm and the polymerisation depolymerisation of actin filaments. On timescale longer than this turnover timescale, the actomyosin cortex cannot sustain elastic stresses.

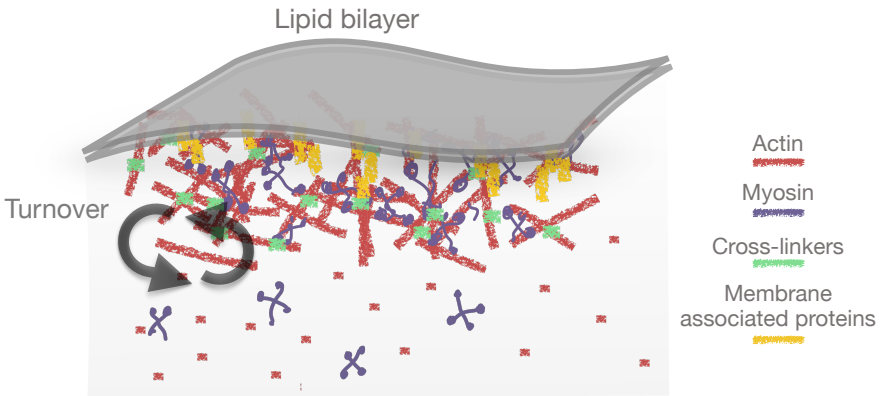

Figure 3.1: The actomyosin cortex is a highly dynamical structure with turnover, or cytoplasmic exchange, due to attachment-detachment of the myosin motor proteins and the polymerisation-depolymerisation of the actin filaments.

In this chapter, we first study a minimal model for the actomyosin cortex that incorporates mechanochemical stresses. We are interested in the dynamics of emergent self-organised patterns in the actomyosin cortex and their interplay with a fixed geometry of the surface. Cells

often exist in environments with complex geometric confinement due to constraints of development (embryos in eggshells) or of organismal physiology (cells surrounded by the other cells, or by secreted material like the extracellular matrix). With this in mind, we ask how patterns interact with the underlying fixed geometry, and what role does this geometric sensing play for the functioning of cells and embryos. Finally, we discuss how the interplay of a furrow-like geometry, active stresses, and cytoplasmic exchange can drive patterns of myosin and flow that mimic those observed during cytokinesis.

3.1 THE CORTEX AS AN ACTIVE FLUID

Towards the end of the first chapter, we discussed experimental studies that provided strong evidence that the forces necessary for cytokinesis do not originate from the spindle [Swann and Mitchison, 1953; Hiramoto, 1956]. However, the suggestion that the dynamics of cell surface could lead to cytokinesis predates these studies by several decades. Otto Bütchli was possibly the first to describe cytokinesis as a process driven by the mechanical forces generated on the "cell surface" [Bütschli, 1876]. Decades later, experimental studies on cytokinesis of ctenophore embryos by Naohide Yatsu also noted the rearrangements in the fluid-like outer surface during cytokinesis [Yatsu, 1912]. The early attempts at developing a theoretical understanding of cytokinesis, therefore, were already treating the cell surface as a fluid layer and phenomenologically studied the problem of cytokinesis patterns on this fluid layer by assuming gradients of surface tension driving Marangoni flows, in turn driving the shape changes [Greenspan, 1977; White and Borisy, 1983].

More recently, techniques like cortical laser ablation and co-moving mass-balance imaging have allowed a more quantitative probe into the mechanical parameters such as the viscoelastic relaxation time τ_M, length scales over which the velocity field is correlated, and the turnover rate [Mayer et al., 2010; Saha et al., 2016; Nishikawa et al., 2017]. From such studies, we understand that the actomyosin behaves as active viscoelastic gel that shows elastic response at short timescales and flows like a viscous fluid at long timescales. As such, the constitutive relation for the actomyosin cortex is well-approximated by

a linear Maxwell-Jeffrey viscoelastic model. In other words, the total hydrodynamic stress $\boldsymbol{\Sigma}$ satisfies

$$\left(1 + \tau_M \frac{D}{Dt}\right)(\boldsymbol{\Sigma} - \boldsymbol{\Sigma}^{\text{orientation}} - \boldsymbol{\Sigma}^{\text{active}}) = \boldsymbol{\Sigma}^{\text{fluid}}, \tag{3.1}$$

where $\boldsymbol{\Sigma}^{\text{orientation}}$ is the stress due to the orientational degrees of freedom, $\boldsymbol{\Sigma}^{\text{fluid}}$ is the fluidic stress, and $\boldsymbol{\Sigma}^{\text{active}}$ is the active stress.

Hydrodynamic flows in the actomyosin cortex occur are such that they are dominated by viscous effects, i.e., the Reynolds number is very low. In this scenario, momentum conservation is essentially captured by a balance of forces acting on the material:

$$\nabla \cdot \boldsymbol{\Sigma} + \mathbf{F}_{\text{ext}} = 0, \tag{3.2}$$

where $\mathbf{F}_{\text{ext}}$ represents the external forces.

Stresses in the cortex

The active stress $\boldsymbol{\Sigma}^{\text{active}}$ arises from the ATP consuming activity of molecular motors. For three-dimensional active gels, the simplest form of such an active stress is given by $\boldsymbol{\Sigma}^{\text{active}} = \zeta \, \Delta\mu \, f(c) \, \mathbf{Q}$, where ζ is an activity coefficient, $\Delta\mu$ represents the chemical potential difference of ATP hydrolysis, $\mathbf{Q}$ is a symmetric traceless tensor representing the local orientational order in the actomyosin cortex, and $f(c)$ is a monotonically increasing function of the concentration c of active stress regulating molecules (such as myosin). Note that the active stress cannot be isotropic for an three-dimensional incompressible material. However, on a surface, the active stress can be isotropic in the tangent plane to the surface.

As noted earlier, the actomyosin cortex is a thin fluid film located just beneath the plasma membrane and also interacts with the cytoplasm. In principle, one should consider the coupling between cortical flows and cytoplasm flows and the external force $\mathbf{F}_{\text{ext}}$ arises from traction effects [Mietke et al., 2019a]. However, we can approximate this effects by a frictional drag force, i.e., $\mathbf{F}_{\text{ext}} = -\gamma \mathbf{v}$, where γ is a friction coefficient.

Cortical laser ablation studies in the actomyosin ring of gastrulating zebrafish (*D. rerio*) embryos and in the actomyosin cortex of the zygote of the nematode worm *C. elegans* [Mayer et al., 2010; Saha et al., 2016] show that the Maxwell relaxation timescale τ_M is of the order of a fee seconds . Comparing this number to the typical timescales of cytokinesis in these embryos ($\sim 10^2 - 10^3$ s), it is clear the cortex can be approximated as a fluid at the timescale of cytokinesis. In other words, we can set $\tau_M \sim 0$.

Maxwell relaxation timescale for the cortex

The dynamics of orientational degrees of freedom is important at the timescales of cytokinesis [Spira et al., 2017]. In fact, the timescale for the relaxation of the orientational order to an isotropic state is of the order of a few minutes [Reymann et al., 2016]. However, studying the dynamics of patterns in anisotropic degrees of freedom on curved non-trivial (and dynamical) geometries is significantly involved [Salbreux and Jülicher, 2017; Al-Izzi and Morris, 2023]. In this thesis, we approximate the actomyosin cortex as an isotropic fluid (in the tangent plane) and hence neglect the effects of orientational degrees of freedom, i.e., we work with the assumption $\boldsymbol{\Sigma}^{\text{orientation}} = 0$ and $\boldsymbol{\Sigma}^{\text{active}}$ is isotropic in the plane of the cortex.

The turnover of the actomyosin cortex maintains its material density at a constant value. As such, tangential flows in the actomyosin cortex are *not* incompressible. The material exchange between the surface and the cytoplasm occurs predominantly in regions with non-zero divergence of the velocity. Furthermore, the hydrodynamic pressure in a surface material with constant turnover just leads to a modification its bulk viscosity [Jülicher et al., 2018]. As such, using a Newtonian constitutive relation, the fluid stress can be written as

$$\boldsymbol{\Sigma}^{\text{fluid}} = 2\eta\,\mathbf{E} + (\eta_b - \eta)\,\mathrm{Tr}(\mathbf{E})\,\mathbf{I}, \tag{3.3}$$

where η and η_b are, respectively, the shear and bulk viscosities, $\mathbf{I}$ is the identity tensor in the plane of the cortex, $\mathrm{Tr}(\cdots)$ denotes the trace operation, and the surface strain-rate tensor $\mathbf{E} = [\nabla\mathbf{v} + (\nabla\mathbf{v})^{\mathsf{T}}]/2$ with $(\cdots)^{\mathsf{T}}$ denoting the transpose. For a thin film of an incompressible three-dimensional Newtonian fluid, the shear and bulk viscosities are related to each other [Jenkins and Dysthe, 1997]. Note that on curved surfaces, the identity tensor $\mathbf{I}$ will be replaced by the tangential projector $\mathbf{P}$ introduced in the previous chapter.

To summarize, given an active stress $\boldsymbol{\Sigma}^{\text{active}} = \zeta\,\Delta\mu\,f(c)\,\mathbf{I}$ (isotropic in the tangent place of the surface), combining the force-balance condition, the constitutive relation for a viscous fluid, and the frictional approximation for the external force, we obtain the equation governing active cortical flows on a two-dimensional flat surface

$$\eta\nabla^2\mathbf{v} + \eta_b\nabla(\nabla\cdot\mathbf{v}) - \gamma\,\mathbf{v} = -\zeta\,\Delta\mu\,\nabla f(c). \tag{3.4}$$

Thus gradients in active stress, i.e., myosin contractility, are the source for cortical flows. These flows are correlated over a hydrodynamic

length-scale $\ell = \sqrt{\eta/\gamma}$. A higher value of ℓ implies that the flows are long-ranged and vice versa.

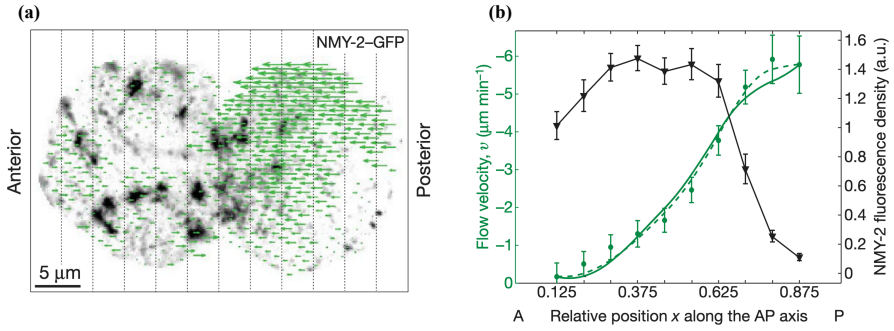

Figure 3.2: (a) The green glyphs depict the measured flows from particle imaging velocimetry (PIV), the dark punctae signifying regions of clustered NMY-2. (b) The black curve shows average NMY-2 intensity, and the green points show the measured flow. Error bars represent the standard error, N=75. The green lines are fits from the theory, the solid line representing the fit corresponding to the assumption $f(c) = c$, and the dashed line corresponds to $f(c) = c/(c + c_*)$. Both panels reproduced with permission, from Mayer *et al.*, *Nature* (2010) [Mayer et al., 2010] ©Springer Nature Limited.

The above picture of contractility gradients driving actomyosin flows has been quantitatively established in the *C. elegans* zygote [Mayer et al., 2010]. Here, a large-scale gradient of myosin concentration in the cortex drives cortical flows that lead to the establishment of cell polarity. This polarity pattern sets the anteroposterior axis of the organism. The large-scale cortical flows persist for several minutes, and therefore are well into the regime of fluid behaviour of the cortex

Measuring cortical flows

. Video microscopy analysis of fluorescently tagged myosin motors allows one to extract their concentration field (see Figure3.2(a)). Particle image velocimetry techniques provides a quantitative handle on estimating the cortical flows. Assuming azimuthal symmetry, the profile of myosin concentration and cortical flows are shown in Figure 3.2(b). We can now use the one-dimensional version of (3.4) to check the prediction contractility gradients driving cortical flows. Figure 3.2(b) shows fits of the theory to the experimental data using the myosin concentration field as an input. The excellent match between theoretical predictions and the experimental data confirms the validity of the active gel picture as applied to the actomyosin cortex.

Quantitative comparison of the flows with the active gel theory provides a route to extract material parameters of the cortex. From the fits shown in Figure 3.2(b), the extracted hydrodynamic length-scale

$\ell \sim 15\,\mu$m. Comparing this to the size of the *C. elegans* embryo (long axis $\sim 50\,\mu$m and short axis $\sim 30\,\mu$m), we find that the associated length-scale of these flows seem to be a significant fraction of the embryo size.

3.2 MECHANOCHEMICAL PATTERNS IN ACTIVE FLUIDS

We concluded from (3.4) that gradients in the active stress regulated by the function $f(c)$ are the source for cortical flows, and Figure 3.2 showed that this picture hold quantitatively in the cell. However, what maintains the profile the of the active stress? In other words, how is a spatial pattern of the concentration field c sustained? Can such active mechanochemical patterns arise spontaneously? We note that the cortical flow that arises from (3.4) will advect the very same concentration field whose gradients gave rise to the flow. In other words, the dynamics of the concentration profile gets an advective feedback from the cortical flows.

First, consider (3.4) in one-dimension:

$$\eta \partial_x^2 v - \gamma v = -\zeta\, \Delta\mu\, \partial_x f(c). \tag{3.5}$$

A 1-dimensional active fluid

Without loss of generality, we take the active stress regulation form

$$f(c) = \frac{c}{c + c_*}, \tag{3.6}$$

where c_* is a saturation concentration. The transport equation for myosin concentration c is

$$\partial_t c = -\partial_x (vc) + D\partial_x^2 c + \mathcal{R}(c), \tag{3.7}$$

where D is an effective diffusion constant and $\mathcal{R}(c)$ represents the chemical reactions that can change the surface concentration. For simplicity, we consider a linear reaction

$$\mathcal{R}(c) = -\kappa\,(c - c_0), \tag{3.8}$$

where κ is the turnover rate and c_0 is a set-point concentration. Equations (3.5) and (3.7) provide a complete system of equations for the concentration c and the flow v, when supplemented with appropriate boundary conditions and the initial concentration $c(x, 0)$.

The homogeneous state $c(x) = c_0$ and $v(x) = 0$ is a trivial fixed point of the system of equations (3.5) and (3.7). However, at high

sufficiently high activity, this state can become linearly unstable to small perturbations and the ensuing nonlinear dynamics can lead to the emergence of spontaneous patterns [Bois et al., 2011]. On a finite domain of size L with periodic boundary conditions, the allowed wavenumbers in such a domain are are $q = \pm 2n\pi/L$ where $n \in \mathbb{Z}$. Considering perturbations of the form $c(x) = c_0 + \delta c\, e^{iqx+\omega(q)\,t}$, a linear stability analysis leads to the wavenumber dependent growth rate $\omega(q)$ of the form [Bois et al., 2011]

$$\omega(q) = -\kappa - D\,q^2 + \zeta\,\Delta\mu\; c_0 \left(\frac{df}{dc}\right)_{c=c_0} \frac{q^2}{\eta q^2 + \gamma}. \tag{3.9}$$

From the above dispersion relation, we note that $\omega(q)$ can become positive at sufficiently large values of $\zeta\,\Delta\mu$. It is interesting to note that homogeneous state can become unstable via this mechanism even in the absence of the chemical reactions $\mathcal{R}(c)$.

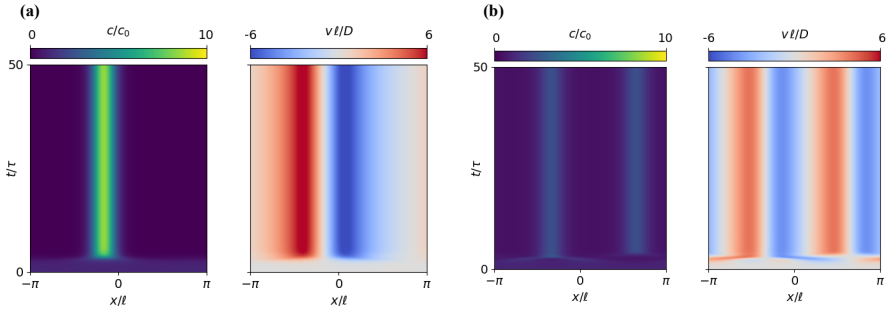

Figure 3.3: Mechanochemical patterns in one-dimension resulting from the numerical simulation of (3.5) and (3.7). Stationary patterns with (a) $\kappa = 0$ and (b) $\kappa \neq 0$.

Numerical simulations of equations (3.5) and (3.7) show that the instability of the homogeneous pattern at high activity leads to the emergence of active mechanochemical as displayed in Figure 3.3. Stationary patterns emerge when there is a balance between advective and diffusive transport, along with the turnover reaction if it is present. Note that patterns of the velocity v along with the patterns of concentration c.

The above formalism for active mechanochemical patterns can be generalized to two-dimensions and also to include multiple species [Bois et al., 2011] that can show spontaneous pulsatory patterns at the linear stability level. Recent studies have also shown leads to novel pulsatory patterns and travelling waves even with a single chemical regulator of active stress. However, these time-dependent patterns do not occur the level of the linear instability of the homogeneous

state, but are secondary bifurcations in the highly nonlinear regime arising from non-reciprocal interaction between the spatial modes of the concentration field [Picardo et al., 2025].

In this section, we considered novel mechanochemical patterns that arise from the essential coupling between cortical flows arising from active stress gradients and the advective transport of the chemical regulators of the mechanical stress. The ensuing patterns of concentration are accompanied by the concomitant patterns of flow and mechanical stress. These are very unlike reaction-diffusion systems involving only scalar fields of concentrations. Since these active mechanochemical patterns essentially involve the velocity vector field, it is natural that the geometry of the underlying domain will have a significant influence on these patterns. With this motivation, we consider active patterns on static two-dimensional curved surfaces embedded in the ambient three-dimensional space.

3.3 GEOMETRIC LOCALISATION OF ACTIVE PATTERNS

How do active mechanochemical patterns react to the underlying to the geometry of the underlying domain? Can inhomogeneities in surface curvature localize such patterns? Are there transitions when material parameters are varied?

We shall consider a closed two-dimensional orientable surface Ω embedded in the ambient three-dimensional space. To setup the equations for active patterns, we first need to develop the calculus of scalar, vector, and tensor fields defined on these surfaces. This was the subject of chapter 2. Recall that for an orientable surface with unit normal vector $\hat{\mathbf{n}}$, the projection operator $\mathbf{P} = \mathbf{I} - \hat{\mathbf{n}} \otimes \hat{\mathbf{n}}$ defines the local tangent plane and also provides a way to compute surface derivatives. Specifically, the covariant derivative of the concentration field is $\nabla c = \mathbf{P} \cdot \nabla_3 c$ where ∇_3 is the Cartesian derivative in the ambient space. For a vector field $\mathbf{v}$, the covariant derivative is $\nabla \mathbf{v} = \mathbf{P} \cdot (\nabla_3 \mathbf{v}) \cdot \mathbf{P}$. The projection operator $\mathbf{P}$ also plays the role of the surface metric tensor.

Force balance on curved geoemtries

As before, we assume that the active stresses are isotropic in the tangent plane to the cortical surface. In this case, the total hydrodynamic stress is given by

$$\boldsymbol{\Sigma} = 2\eta\, \mathbf{E} + (\eta_b - \eta)\, \mathrm{Tr}(\mathbf{E})\, \mathbf{P} + \zeta\, \Delta\mu\, f(c)\, \mathbf{P}, \tag{3.10}$$

where $\mathbf{P}$ now replaces $\mathbf{I}$ for the isotropic parts, and the surface strain-rate tensor is $\mathbf{E} = [\nabla \mathbf{c} + (\nabla \mathbf{v})^{\mathsf{T}}]/2$. The force-balance condition $\nabla \cdot \boldsymbol{\Sigma} = \gamma \mathbf{v}$ would lead to a flow equation analogous to (3.4).

Analytical solutions to these problems are only possible for simple geometries, such as a sphere, where the vector spherical harmonics provide a natural spectral representation for tangential vector fields [Picardo et al., 2025]. However, on arbitrary curved two-dimensional surfaces, no such spectral representations are known for tangential vector fields. In such a case, one has to resort to numerical methods. A naïve way to implement numerical methods would be to use surface fitted coordinates and develop the covariant calculus of the scalar and tangential vector fields. However, such an approach is fraught with coordinate singularities and is numerically unstable most of the time.

An alternate numerical approach, building on the tangential calculus that we developed in Chapter 2, is to consider a vector field $\mathbf{v}$ in the ambient space with support only the surface $\Omega \subset \mathbb{R}^3$. As before, we extend this vector field via a *constant normal extension* into small neighbourhoods "above" and "below" Ω. With this approach, we can now compute surface derivatives using the projector operator $\mathbf{P}$. We implement the tangential nature of the vector field $\mathbf{v}$ by imposing the constraint

$$\hat{\mathbf{n}} \cdot \mathbf{v} = 0 \tag{3.11}$$

at all points on Ω [Jankuhn et al., 2018]. Further, we incorporate a Lagrange multiplier field $\lambda(\mathbf{x})$ to remove any normal components in the force-balance condition. Thus

$$\nabla \cdot \boldsymbol{\Sigma} = \gamma \mathbf{v} - \lambda(\mathbf{x})\, \hat{\mathbf{n}}. \tag{3.12}$$

The above two equations, along with the (3.10), provide a complete description to obtain the surface flows given a concentration field $c(\mathbf{x})$. As alluded to above, we can analytically solve for the flow for a spherical surface for a given $c($**x** using vector spherical harmonics. We have benchmarked the numerical solution obtained from solving (3.12) and (3.11) via the finite-element method using the FEniCS library [Alnæs et al., 2015]. Comparing with the analytical solutions, we find that our numerical approach provides a convergent method to obtain the flow field.

To obtain the flow equation analogous to (3.4), we need to use the constitutive relation (3.10) in the force-balance condition (3.12).

This brings in some subtleties of the differential geometry of curved surfaces. First, we note that $\nabla \cdot (\nabla \mathbf{v}) = \nabla^2 \mathbf{v}$ gives the covariant Laplacian of the vector field $\mathbf{v}(\mathbf{x})$. However, computing $\nabla \cdot (\nabla \mathbf{v})$ is not straightforward, as covariant derivatives of tangential vector fields do not commute [Thomas, 1961; Kreyszig, 1991; Walker, 2015]. However, for two-dimenesional surfaces, it can be shown that $\nabla \cdot (\nabla \mathbf{v}) = \nabla(\nabla \cdot \mathbf{v}) + \mathcal{K}\,\mathbf{v}$ where $\mathcal{K}$ is the Gaussian curvature of the surface [Grinfeld et al., 2013; Walker, 2015; Jankuhn et al., 2018]. Furthermore, noting that $\nabla \cdot [f(c)\mathbf{P}] = \nabla f(c)$ leads to the flow equation on a curved surface:

$$\eta \nabla^2 \mathbf{v} + \eta_b \nabla(\nabla \cdot \mathbf{v}) + (\eta\, \mathcal{K} - \gamma)\, \mathbf{v} = -\zeta\, \Delta\mu\, \nabla f(c) - \lambda(\mathbf{x})\, \hat{\mathbf{n}}. \quad (3.13)$$

It should be remarked that we do not directly solve the above flow equation in our finite-element formulation. Rather, we solve (3.12) along with the tangentiality constraint (3.11). As in the case of flat domains, the concentration c of the active stress regulator satisfies the following advection-diffision-reaction equation on the surface:

$$\partial_t c = -\nabla \cdot (\mathbf{v} c) + D \nabla^2 c - \kappa (c - c_0), \quad (3.14)$$

where ∇ is the surface covariant derivative. To summarize, equations (3.12), (3.11), and (3.14) complete our description for active mechanochemical surfaces on arbitrary closed two-dimensional curved surfaces. Given an initial condition $c(\mathbf{x}, 0)$, these equations permit us to numerically explore the interplay of active patterns with surface geometry.

Effective friction modified by Gaussian curvature

We highlight that the term $\eta \mathcal{K} \mathbf{v}$ acts as a competitive friction in (3.13). Identifying $\gamma - \eta\mathcal{K}$ as an effective friction γ_{eff}, we see that on a surface where the Gaussian curvature is not constant, this would lead to spatially dependent frictional drag force on the velocity, Furthermore, on surface where $\mathcal{K} < 0$, the effective friction coefficient can even change sign.

On a spherical surface, the above equations governing active patterns can be analysed via scalar and vector spherical harmonics, to obtain the growth rate of perturbations near the homogeneous state $c = c_0$ and $\mathbf{v} = 0$ via linear stability analysis [Mietke et al., 2019b,a; Picardo et al., 2025]. We have checked that our numerical method reproduces the various phases seen in previous studies on the sphere.

We now study active mechanochemical patterns on generic curved surfaces with a spherical topology. We emphasize here that neither

our model equations nor our numerical code need to be changed for this case. Since we have formulated the problem with reference to Cartesian coordinates in the ambient three-dimensional space, this applied equally well to non-spherical surfaces Ω provided we are given a well-defined normal vector field $\hat{\mathbf{n}}(\mathbf{x})$. Furthermore, our finite-element method is developed in such a manner that changing the geometry only requires us to change the input mesh. The rest of the numerical method is agnostic to the particular geometry being considered.

Spherical harmonic surfaces

We restrict ourselves to *radial* surfaces whose shape can be parametrised by scalar spherical harmonics deviations away from a sphere of radius R_0. We thus choose the parametrisation:

$$\mathbf{x}(\theta,\phi) = R_0 \left[1 + \sum_{lm} \alpha_{lm}\, Y_l^m(\theta,\phi)\right] \hat{\mathbf{r}}(\theta,\phi), \tag{3.15}$$

where θ and ϕ are the usual angles in the spherical coordinate system, α_{lm} is the amplitude for the mode with spherical harmonic $Y_l^m(\theta,\phi)$, and $\hat{\mathbf{r}}(\theta,\phi)$ is the radial unit vector. Furthermore, we shall consider only azimuthally symmetric surfaces $m = 0$ and focus on the $l = 2$ mode, and define $\alpha \equiv \alpha_{20}$. For small values of α, the surface has $\mathcal{K} > 0$ everywhere for small while for large values of α, the surface develops regions with $\mathcal{K} < 0$.

Non-dimensional parameters

The dynamics of the active patterns on arbitrary fixed geometries is characterised by the following parameters:

$$\mathrm{Pe} = \frac{\zeta\,\Delta\mu}{\gamma\, D}, \quad \Lambda = \frac{\ell}{R_0}, \quad \mathrm{Da} = \frac{\kappa\, R_0^2}{D}, \tag{3.16}$$

where the Péclet number Pe compares the strength of the active advective flows with diffusive transport, Λ is the ratio of the hydrodynamic length $\ell = \sqrt{\eta/\gamma}$ to the radius R_0, and Da is the Damköhler number comparing the turnover rate with the diffusive timescale R_0^2/D. We choose the active stress regulation function defined in (3.6) and set $\eta_b = 5\eta/4$. Concentrations and times are reported in units of c_* and $\tau = \ell^2/D$.

We first consider surfaces corresponding to $\alpha = 0.2$, i.e., with a minimal from the sphere. Our first observation is that close to the pattern formation threshold (where the homogeneous state loses stability), the emergent spots of concentration patterns localise to the poles of the surface (and have an azimuthally symmetric profile). It is important to note that these are also the regions of highest Gaussian curvature,

as seen in Figure 3.4. On systematically increasing Pe while keeping other parameters fixed, we find that while the initial pattern still forms around the 'polar regions' of the surface (see Figure 3.5), this configuration eventually destabilises and localises on the equatorial region of the surface, where the curvature is the lowest.

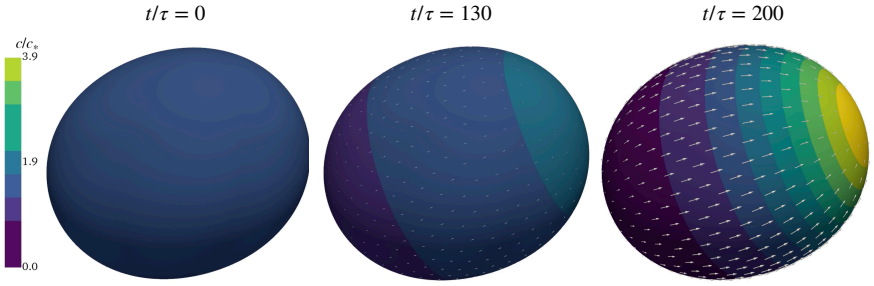

Figure 3.4: The patterns spontaneously localise in regions of high curvature. The colours represent local myosin concentration and the arrows represent the velocity profile on the surface. Here $\Lambda = 0.45$ $\mathrm{Da} = 0$, and $\mathrm{Pe} = 10$.

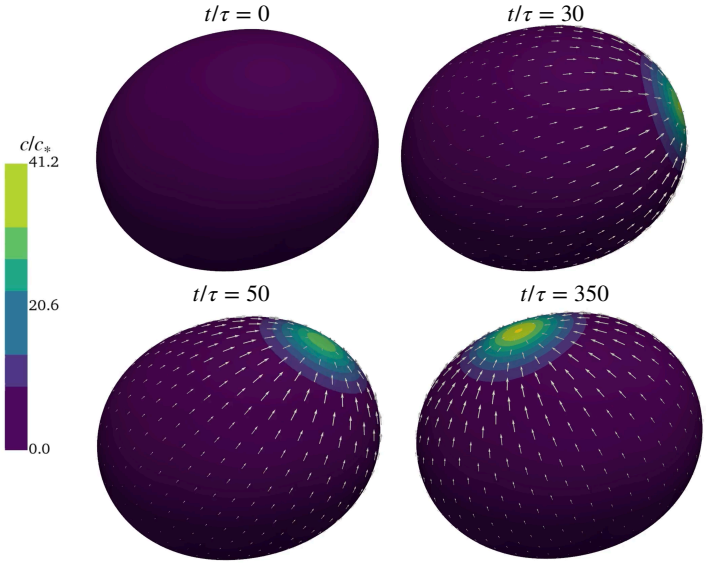

Figure 3.5: Keeping the geometry and other parameters constant, at higher contractility ($\mathrm{Pe} = 40$), one can observe an initial breakage of symmetry at the high curvature region. This pattern, however, quickly destabilises and moves to a region of lower curvature. It is important to highlight that the stable profile of concentration and flow *breaks* the azimuthal symmetry of the surface geometry.

A most interesting aspect of these patterns is that at low Pe they retain the azimuthal symmetry of the surface. However, in going to the equator at higher Pe, the pattern *breaks* azimuthal symmetry. Note that any assumption of an azimuthal symmetry while formulating the

problem (rendering the problem one-dimensional, mathematically) would have precluded the emergence of such patterns. Therefore, at low values of contractility the patterns are stable in regions of high curvature. As the contractility increases, the patterns that initially form in these regions destabilise and localise to regions of increasing γ_{eff}. As such, these active patterns are therefore sensitive to the underlying geometry.

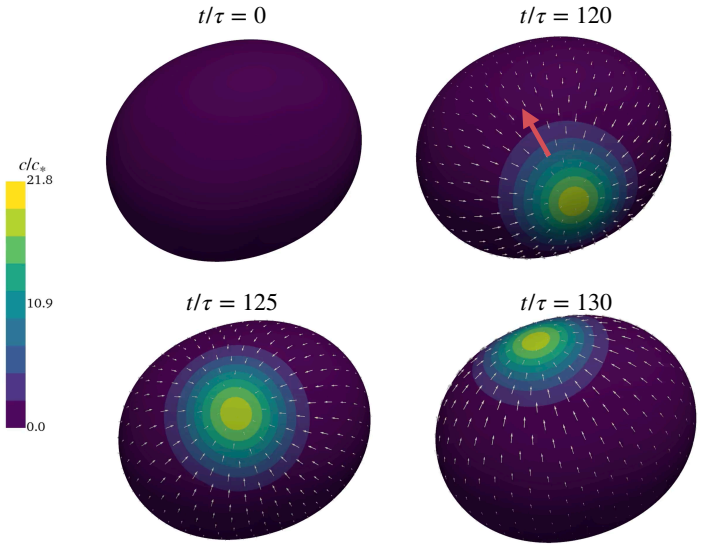

Figure 3.6: In regimes of high contractility and turnover (cytoplasmic exchange), we also observe the spontaneous emergence of waves. As before, the colours depict the myosin concentrations and white arrows denote the velocity field. The red arrow shows the direction of movement of the wave, as seen in the lower panels. Note that, at these parameters, the wave *also* remains localised along a specific geometry, i.e., the equator.

Geometric effects in cortical flows

Such geometric canalisation of patterns has been implicated in the division axis alignment of *C. elegans* AB cells [Middelkoop et al., 2024]. These cells have a non-trivial geometry due to confinement within an eggshell. Strikingly, the polarisation of the *C. elegans* embryo discussed in the first chapter also shows a similar self-organised alignment of polar patterns with the geometric axis of the embryo. The PAR-2/PAR-6 polarity system triggered by the sperm entry is sometimes observed to start at non-polar locations on the embryo leading to a misalignment of the polarity pattern with the geometric axis of the embryo. However, this misalignment is rapidly rectified by the curvature-dependent active flows on the cortex and the ensuing flows in the cytoplasm [Bhatnagar et al., 2023]. Without invoking nematic order parameters, our results show that such geometrisation of active

mechanochemical patterns can occur naturally due to an effective friction-coefficient dependent on the Gaussian curvature. A clear prediction from our results here is that changes in global contractilities should have a drastic impact on the ability of the embryo to correct for the geometric misalignments. Similar geometric effects due to flows arising from active stresses, could also underlie polarised dynamics at much bigger scales, for example, at the early stages of *Drosophila* development [Gehrels et al., 2023].

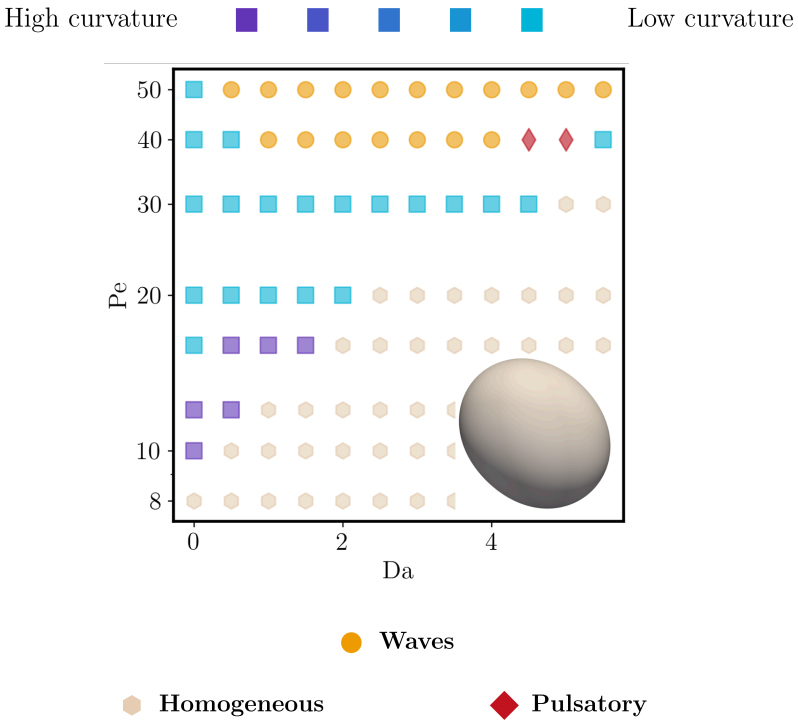

Figure 3.7: Phase diagram depicting the emergent patterns on a fixed geometry with $\alpha = 0.2$. The dark and light coloured squared denote time-independent spot-like patterns on high and low curvature regions, respectively. The pulsatory patterns are not discussed in this chapter, but analogous to those observed on a sphere [Picardo et al., 2025].

Next, we study the effect of cytoplasmic exchange rate Da on the dynamics of active patterns. Varying Da, we observe the appearance of active waves in Figure 3.6 reported earlier on simpler geometries. From the figure, it is also clear that at these values of the parameters, the waves seem to localise along the equator, a fact that will be of crucial importance in the next section. A summary of the different patterns discussed here can be seen in the phase-diagram shown in Figure 3.7. We observe the transitions of spot localising in regions of high curvature at low Pe, and lower curvatures at high Pe. The

variation in the turnover strength can be observed along the x-axis, where we first see the emergence of active waves discussed above, and then see the emergence of pulsatory patterns at even higher turnover [Picardo et al., 2025].

3.4 NOVEL PATTERNS ON NEGATIVELY CURVED SURFACES

We now consider surface with larger deformation amplitudes. A surface with $\alpha = 0.8$ has a furrow-like region at the equator of the surface. Note that this region of the surface is saddle-like, and therefore has $\mathcal{K} < 0$. This implies that γ_{eff} can change sign.

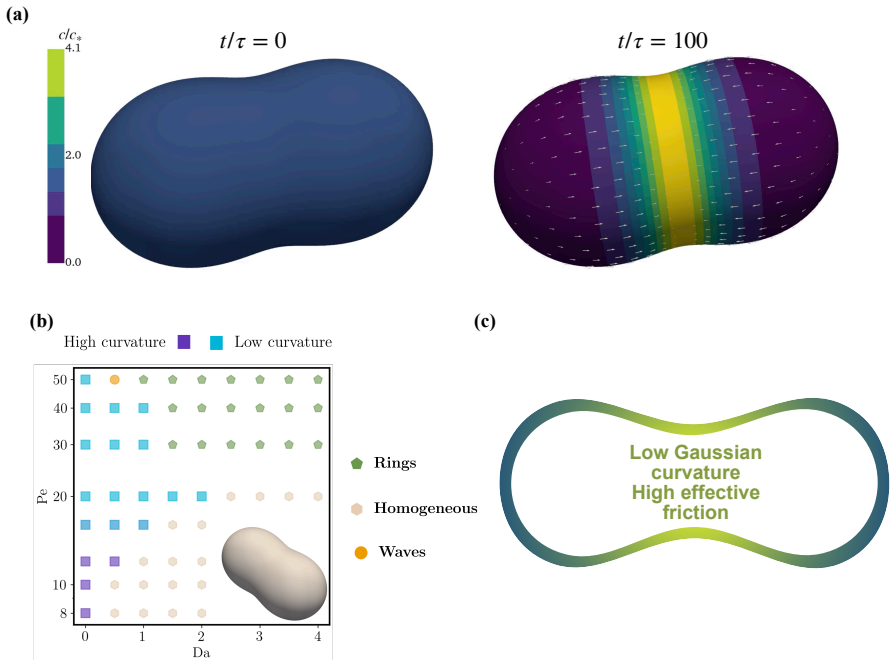

Figure 3.8: As the parameter α is increased, qualitatively novel patterns are observed once regions of negative Gaussian curvature emerge on the surface geometry. **(a)** The emergence of cytokinetic patterns, with convergent flows and myosin localisation at the furrow. The physical parameters here are identical to Figure 3.6, only the surface geometry parameter is set to $\alpha = 0.8$. **b** The phase diagram depicting the various patterns that emerge spontaneously. **c** Schematic depicting the localisation of myosin in regions of low Gaussian curvature, and therefore a higher effective friction γ_{eff}.

At $\text{Da} = 0$, we observe spot like patterns that move from regions of high curvature to regions of low curvature with increase in Pe. However, as the turnover strength is increased, qualitatively novel patterns are observed. In the regime where one could observe dynamical waves for the geometry $\alpha = 0.2$, we now observe patterns

that are steady and resemble the cytokinetic ring during cell division. Note that the flow profile also seems similar to the convergent flows observed in cells as shown in Figure 1.2 **(c)**. The observation of ring patterns at *high* turnover should also be viewed in the light of recent experiments, which showed an inhibition of myosin turnover in the contractile ring naturally leads to its destabilisation and breakup into multiple punctae [Thiyagarajan et al., 2022]. As such, this result not only points to the high sensitivity of active patterns to underlying geometry and turnover, but more broadly, it possibly also suggests the self-organised nature of cytokinetic patterns in the cortex.

3.5 SUMMARY

To summarise, after developing an active hydrodynamic description of the actomyosin cortex that agrees with experimental measurements, we formulated a minimalistic description to study active mechanochemical patterns on curved two-dimensional surfaces. We discussed how Gaussian curvature can act as an effective friction, giving rise to complex dynamics that is very different from that observed on a simple geometries like flat planes or spheres. Further, we observed how a change in geometry, without any change in physical parameters, can give rise to qualitatively different patterns. We saw that on surface geometries that mimic the dividing cell, myosin distributions and flow patterns naturally self organise to a steady state that is reminiscent of cytokinesis. In this chapter, we have only focused on *fixed* geometries while the full problem of cytokinesis is that of a coupling between the dynamics of surface concentrations, the flows generated due to gradients in active stresses, and the dynamics of geometry due to differential forces generated from the concentration gradients. This forms the subject of the next chapter.

4

GEOMETRODYNAMICS OF CYTOKINESIS

> *. . . for geometry, you know, is the gate of science, and the gate is so low and small that one can only enter it as a little child.*
>
> *William K. Clifford*

This chapter is about the self-organised dynamics of active surfaces, focusing mainly on the cytokinesis like patterns that emerge therein. We observe a spontaneous emergence of ring-like patterns. We then compare these emergent patterns of myosin and shape to the cytokinesis with the first embryonic division of the nematode *C. elegans*, and then study relationships between the emergent parameters that characterise cytokinesis, and the underlying geometrodynamic feedback.

4.1 DYNAMICS OF PASSIVE SURFACES

On timescales longer than the relaxation time for the elastic stresses, the actomyosin cortex flows like a viscous fluid [Saha et al., 2016]. Motivated by this long-time dynamics, we consider *fluid surfaces* wherein the surface deforms only along the local normal direction. Therefore, given a velocity field $\mathbf{v} = \mathbf{v}_\parallel + \mathbf{v}_\perp$ on the surface, the motion of a material point with position vector $\mathbf{x}$ is

$$\frac{d\mathbf{x}}{dt} = \mathbf{v}_\perp. \tag{4.1}$$

As the surface deforms, its geometry changes. The unit normal vector field, the projection operator and the shape operator on the surface sat-

isfy the equations (2.18), (2.19), and (2.28). We rewrite these equations here:

Geometry evolution

$$\frac{\partial \hat{\mathbf{n}}}{\partial t} = -\nabla v_\perp \,, \tag{4.2a}$$

$$\frac{\partial \mathbf{P}}{\partial t} = \nabla v_\perp \otimes \hat{\mathbf{n}} + \hat{\mathbf{n}} \otimes \nabla v_\perp \,, \tag{4.2b}$$

$$\frac{\partial \mathbf{S}}{\partial t} = -\nabla\nabla v_\perp - v_\perp \mathbf{S}\cdot\mathbf{S} + (\hat{\mathbf{n}} \otimes \nabla v_\perp)\cdot\mathbf{S} + \mathbf{S}\cdot(\nabla v_\perp \otimes \hat{\mathbf{n}}) \,. \tag{4.2c}$$

Here $v_\perp = \mathbf{v}\cdot\hat{\mathbf{n}}$ is the magnitude of the normal velocity. Note that $\hat{\mathbf{n}}$ and $\mathbf{P}$ changes only when $\nabla v_\perp \neq 0$, i.e., uniform translation does not change the surface normal and the tangent plane. Furthermore, These equations govern the surface dynamics for a given velocity $\mathbf{v}$. This velocity is obtained from other physical considerations.

The internal forces arising from interactions between the fluid-elements on the surface are captured by a stress tensor $\boldsymbol{\Sigma}$. On cellular scales, inertial forces are negligible. As such, the velocity field $\mathbf{v}$ is obtained from force- and torque-balance conditions encapsulated by

$$\nabla\cdot\boldsymbol{\Sigma} = -\mathbf{F}_{\text{ext}}, \tag{4.3}$$

where $\mathbf{F}_{\text{ext}}$ is the total external force on the surface. We neglect hydrodynamic flows in the cytoplasm, approximate its dissipative effects by a frictional force $-\gamma\,\mathbf{v}$ [Salbreux et al., 2009], and incorporate its incompressibility by including a constraint force $\Delta p\,\hat{\mathbf{n}}$, where the Lagrange multiplier Δp is the spatially uniform pressure difference across the surface obtained by implementing the volume constraint $\int_{\text{surface}} v_\perp = 0$. We therefore get the total external force as $\mathbf{F}_{\text{ext}} = -\gamma\,\mathbf{v} + \Delta p\,\hat{\mathbf{n}}$. To hold the centre-of-mass fixed, we include an additional force $\mathbf{F}_{\text{CM}}\cdot(\hat{\mathbf{n}}\otimes\hat{\mathbf{n}})$, where $\mathbf{F}_{\text{CM}}$ is a time-dependent Lagrange multiplier implementing the constraint $\int_{\text{surface}}(v_\perp\,\hat{\mathbf{n}}) = \mathbf{0}$.

The hydrodynamic stress $\boldsymbol{\Sigma}$ has contributions from the viscous stresses arising from in-plane velocity gradients $\nabla\mathbf{v}$, the forces arising from the bending elasticity of the surface, and finally the nonequilibrium active stresses arising from the ATP consuming activity of molecular motors. Assuming the surface behaves as a Newtonian fluid, the viscous stress is

$$\boldsymbol{\Sigma}_{\text{viscous}} = 2\eta\,\mathbf{E} + (\eta_b - \eta)\,\mathrm{Tr}(\mathbf{E})\,\mathbf{P}, \tag{4.4}$$

where η and η_b are, respectively, the shear and bulk viscosities, and the surface strain-rate tensor $\mathbf{E} = [\nabla\mathbf{v} + (\nabla\mathbf{v})^{\mathsf{T}}]/2$ with $(\cdots)^{\mathsf{T}}$ denoting the transpose. Note that we have assumed that cytoplasmic exchange maintains the material density of the surface at a constant value, and have also neglected the two-dimensional pressure [Jülicher et al., 2018]. The Canham-Helfrich energy $\mathcal{E}_{\text{CH}} = \beta \int_{\text{surface}} \mathcal{H}^2$, where β is an elastic modulus, governs the bending elasticity of a symmetric bilayer without any spontaneous curvature [Canham, 1970; Helfrich, 1973]. The equilibrium shapes of such fluid-surfaces, corresponding to the minima of $\mathcal{E}_{\text{CH}}$, can be obtained by considering the bending stress [Capovilla and Guven, 2002; Capovilla et al., 2005; Salbreux and Jülicher, 2017],

$$\mathbf{\Sigma}_{\text{bending}} = \beta\, \mathcal{H}\, [(\mathcal{H}\,\mathbf{P} - 2\,\mathbf{S}) + 2\nabla\mathcal{H} \otimes \hat{\mathbf{n}}] \,. \tag{4.5}$$

Note that the first term within $[\dots]$ is completely symmetric, owing to the symmetric nature of $\mathbf{P}$ and $\mathbf{S}$. The second term, which is asymmetric, arises due to implicitly taking into account the torque balance on the surface [Salbreux and Jülicher, 2017]. Thus, the geometrodynamics of a passive fluid-surface is governed by equations (4.1) and (4.2), where the velocity is obtained by solving $\nabla \cdot (\mathbf{\Sigma}_{\text{viscous}} + \mathbf{\Sigma}_{\text{bending}}) = -\mathbf{F}_{\text{ext}}$. From the equation for surface evolution (4.1), for the evolution of the surface geometry (4.2) and the force-balance, we obtain the equilibrium shapes of passive surfaces as the long-time limit of the dynamics. To probe this equilibrium dynamics, we start the simulations with a triangulated surface with a non-spherical geometry with a spherical harmonic perturbation such that any given point on the surface is given by $\mathbf{x}(\theta,\phi) = R_0(1 + \alpha Y_m^\ell(\theta,\phi))\hat{\mathbf{n}}$, where R_0 is the radius of the unperturbed spherical mesh. The force balance equation at any instant of time gives us the total velocity $\mathbf{v}$ which renders the tangential velocity $\mathbf{v}_\parallel$ responsible for the passive dissipation due to fluid flows and the $\mathbf{v}_\perp$ responsible for the deformation.

Relaxation dynamics of a passive surface

In Figure 4.1(a) we show the time course of shape evolution for a perturbed shape corresponding to an $\ell = 3$ spherical harmonic deformation. The surface relaxes to a sphere after $\sim \tau$ where τ is an intrinsic timescale for the passive surface dynamics, defined as $\tau = \eta/\beta$. We then calculate the dynamics of the deviation of $\mathcal{E}_{\text{CH}}$ from $\mathcal{E}_0$ ($\mathcal{E}_{\text{CH}}$ corresponding to a perfect sphere). We notice from Figure 4.1 **(b)** that this deviation also approaches zero as the surface relaxes, further confirming that the stable shape for a passive surface is a sphere, which has a constant mean curvature $\mathcal{H}(\mathbf{x}) = \mathcal{H}_0 = 1/R_0$. Here, we have

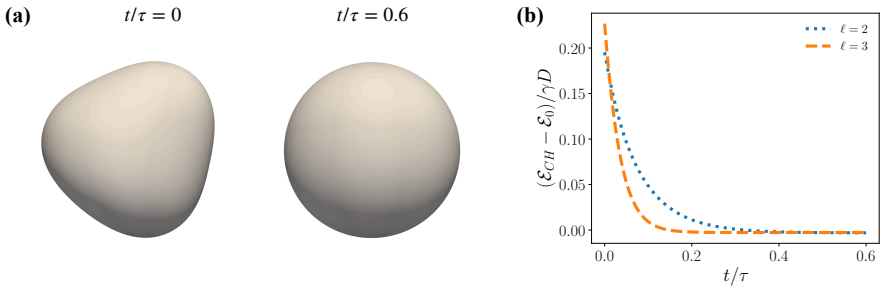

Figure 4.1: (a) Shape evolution of a passive surface with $\ell = 3$ perturbation. (b) Evolution of the deviation of Canham-Helfrich free energy of the surface sphere $\mathcal{E}_0$. The two lines correspond to an initial perturbation in the shape corresponding to $\ell = 2$ (dotted-blue) and $\ell = 3$ mode (dashed-orange).

only enforced the constraint of enclosed volume preservation. Even though we do not explicitly solve for the dynamics of the enclosed fluid (for a cell, the cytoplasm), we consider its incompressible nature through this constraint. With an additional constraint on surface area, a host of equilibrium shapes can be observed, even at equilibrium [Deuling and Helfrich, 1976; Seifert et al., 1991; Seifert, 1997; Martínez-Balbuena et al., 2021]. However, we do not add such a constraint, as it is experimentally observed that the surface area of a cell undergoes considerable increase during cytokinesis [Dan and Dan, 1947; White and Borisy, 1983; Gauthier et al., 2009; Khaliullin et al., 2018].

4.2 ACTIVE SURFACES

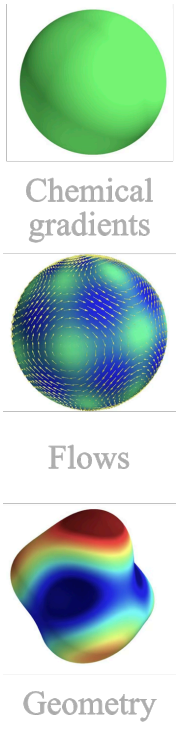

Figure 4.2: Dynamics of active surfaces

From the previous section, we note that the only stable shape of the passive surface with the equilibrium stresses described therein is a sphere. From Fig 4.1, it is also clear that this is the shape that minimises the total Canham-Helfrich free energy of the surface $\mathcal{E}_{\text{CH}}$ is a sphere. To introduce activity in this system, as in the previous chapter, we consider a scalar field representing the myosin concentration on the surface

$$\frac{\partial c}{\partial t} = -\nabla \cdot (\mathbf{v}c) + D\nabla^2 c - k(c - c_0)\,, \tag{4.6}$$

where, the first second and third terms on the right represent the advection, diffusion, and turnover (cytoplasmic exchange) of myosin respectively. Note that unlike the previous chapter, the velocity field now has has a non-zero component in the normal direction $\mathbf{v} \cdot \hat{\mathbf{n}} \neq$

0. Using the directional split of velocity field $\mathbf{v} = \mathbf{v}_\parallel + v_\perp \hat{\mathbf{n}}$ in the advection term we get

$$\nabla \cdot ((\mathbf{v}_\parallel + \mathbf{v}_\perp)c) = c\,(\nabla \cdot \mathbf{v}_\parallel) + \nabla c \cdot \mathbf{v}_\parallel + c\,(\nabla \cdot \mathbf{v}_\perp) + \nabla c \cdot \mathbf{v}_\perp.$$

The final term is zero due to the tangential (surface) derivative having a zero normal component $\nabla c \cdot \mathbf{v}_\perp = \nabla c \cdot (v_\perp \hat{\mathbf{n}}) = 0$. The third term on the right $\nabla \cdot \mathbf{v}_\perp = \nabla \cdot (v_\perp \hat{\mathbf{n}}) = v_\perp \nabla \cdot \hat{\mathbf{n}} + \nabla v_\perp \cdot \hat{\mathbf{n}}$. Where the second term is again zero due to the tangential property of the surface derivative. Realising $\nabla \cdot \hat{\mathbf{n}} = \mathrm{Tr}(\nabla \hat{\mathbf{n}}) = \mathrm{Tr}(\mathbf{S}) = H$ and $c\,(\nabla \cdot \mathbf{v}_\parallel) + \nabla c \cdot \mathbf{v}_\parallel = \nabla \cdot (c\mathbf{v}_\parallel)$, we can rewrite the surface transport equation as:

Directional split of the transport equation

$$\frac{\partial c}{\partial t} = -\nabla \cdot (c\mathbf{v}_\parallel) - H v_\perp\, c + D\nabla^2 c + k(c_0 - c) \tag{4.7}$$

This directional split makes brings out the multiple effects that can change the concentration of myosin at a given point on the active surface. The final two terms on the right remain unchanged when compared to the case with fixed geometry. The first term on the right represents the advection of the concentration field due to fluid transport in the surface, represented by the tangential divergence of the current due to the tangential velocity field $\mathbf{v}_\parallel$. The second term on the right arises purely due to geometric changes of the cell surface. This term represents the local dilatation of the surface, where a negative sign of the dilatation would represent an effective "compression" of the surface. This can be seen from the evolution equation for the area element $\sqrt{g} = \sqrt{\mathrm{Det}(\mathbf{g})}$ of the surface [Waxman, 1984; Powers, 2010] :

$$\frac{\partial \sqrt{g}}{\partial t} = \mathcal{H}\, v_\perp \sqrt{g}\,. \tag{4.8}$$

The total stress in the thin film $\mathbf{\Sigma} = \mathbf{\Sigma}_{\text{viscous}} + \mathbf{\Sigma}_{\text{bending}} + \mathbf{\Sigma}_{\text{active}}$ comprises a passive viscous component $\mathbf{\Sigma}_{\text{viscous}}$, a passive bending component $\mathbf{\Sigma}_{\text{bending}}$, and an active part $\mathbf{\Sigma}_{\text{active}}$. We assume $\mathbf{\Sigma}_{\text{active}}$ is isotropic in the tangent plane of the surface Γ and is regulated by the concentration c of the actomyosin

$$\mathbf{\Sigma}_{\text{active}} = \zeta\, \Delta\mu\, f(c(\mathbf{x}))\, \mathbf{P}, \tag{4.9}$$

where, without loss of generality, we take the stress-regulation function $f(c)$ to be of the form

$$f(c) = \frac{c}{c + c_*}, \tag{4.10}$$

with c_* being a saturation concentration. With all the stresses defined, we can now perform the directional split of the force-balance equation as well. Ignoring the centre-of-mass constraint, we now have:

$$\nabla \cdot (\boldsymbol{\Sigma}_{\text{viscous}} + \boldsymbol{\Sigma}_{\text{bending}} + \boldsymbol{\Sigma}_{\text{active}}) = \gamma \mathbf{v} + \Delta p \hat{\mathbf{n}}.$$

To find the contribution from viscous stresses, we use the definition of the strain rate tensor $\mathbf{E}$ and the directional split of velocity:

$$\begin{aligned}\mathbf{E} &= \frac{\nabla(\mathbf{v}_\parallel + v_\perp \hat{\mathbf{n}}) + \nabla^\mathsf{T}(\mathbf{v}_\parallel + v_\perp \hat{\mathbf{n}})}{2}, \\ &= \mathbf{E}_\parallel + v_\perp \mathbf{S},\end{aligned}$$

Directional split of the force-balance equation

where we identify $\mathbf{E}_\parallel = (\nabla \mathbf{v}_\parallel + \nabla^\mathsf{T} \mathbf{v}_\parallel)/2$, and have used the symmetric property of the curvature tensor $\mathbf{S} = \nabla \hat{\mathbf{n}} = \nabla^\mathsf{T} \hat{\mathbf{n}} = \mathbf{S}^\mathsf{T}$ and the tangentiality of the surface derivative $\nabla v_\perp \cdot \hat{\mathbf{n}} = 0$. We therefore get the contribution of viscous stresses to force balance as:

$$\begin{aligned}\nabla \cdot \boldsymbol{\Sigma}_{\text{viscous}} = \eta &\left(\nabla^2 \mathbf{v}_\parallel + 2(\nabla v_\perp \cdot \mathbf{S} + v_\perp \nabla \mathcal{H})\right) \\ &+ \eta_b \nabla(\nabla \cdot \mathbf{v}_\parallel) + \eta \mathcal{K} \mathbf{v}_\parallel + (\eta_b - \eta)\nabla(\mathcal{H} v_\perp) \\ &- (\eta_b - \eta)[\mathcal{H} \nabla \cdot v_\parallel + v_\perp \mathcal{H}^2 + v_\perp(\mathcal{H}^2 - \mathcal{K})]\, \hat{\mathbf{n}}. \end{aligned} \tag{4.11}$$

To obtain this expression, we have used $\mathcal{H} = \text{Tr}(\mathbf{S})$, $\nabla \cdot \mathbf{S} = \nabla \mathcal{H} - \text{Tr}(\mathbf{S} \cdot \mathbf{S})\hat{\mathbf{n}}$, and $\nabla \cdot \mathbf{P} = -\mathcal{H}\hat{\mathbf{n}}$ Further, from (2.16) we also know that $\text{Tr}(\mathbf{S} \cdot \mathbf{S}) = \mathcal{H}^2 - \mathcal{K}$. From the bending stresses, we get [Capovilla and Guven, 2002]:

$$\nabla \cdot \boldsymbol{\Sigma}_{\text{bending}} = \beta \left(2[\mathcal{H}\mathbf{P} - \mathbf{S}] \cdot \nabla \mathcal{H} + [2\nabla^2 \mathcal{H} + \mathcal{H}^3 - 2\mathcal{K}\mathcal{H}]\, \hat{\mathbf{n}} \right). \tag{4.12}$$

Finally, the active stress gives us:

$$\nabla \cdot \boldsymbol{\Sigma}_{\text{active}} = \zeta \Delta\mu \left(\nabla f(c) - \mathcal{H} f(c) \hat{\mathbf{n}} \right). \tag{4.13}$$

Therefore, the force balance condition in the tangential direction is:

$$\begin{aligned}&\eta \left(\nabla^2 \mathbf{v}_\parallel + 2(\nabla v_\perp \cdot \mathbf{S} + v_\perp \nabla \mathcal{H})\right) \\ &+ \eta_b \nabla(\nabla \cdot \mathbf{v}_\parallel) + \eta \mathcal{K} \mathbf{v}_\parallel + (\eta_b - \eta)\nabla(\mathcal{H} v_\perp) \\ &+ \beta \left(2\nabla \mathcal{H}[\mathcal{H}\mathbf{P} - \mathbf{S}] \right) + \zeta \Delta\mu \nabla f(c) = \gamma \mathbf{v}_\parallel. \end{aligned} \tag{4.14}$$

Collecting the terms with $\hat{\mathbf{n}}$, we get the force-balance in the normal direction:

$$-(\eta_b - \eta)[\mathcal{H}\nabla \cdot v_\parallel + v_\perp \mathcal{H}^2 + v_\perp(\mathcal{H}^2 - \mathcal{K})] + \frac{\beta}{\mathcal{H}}[2\nabla^2\mathcal{H} + \mathcal{H}^3 - 2\mathcal{K}\mathcal{H}] - \zeta\Delta\mu f(c) = \frac{\Delta p + \gamma v_\perp}{\mathcal{H}}. \tag{4.15}$$

"soap bubble" limit of an active surface

We now look at the limit $\beta \to 0$ and consider the absence of concentration gradients which, as can be seen from the tangential force-balance, leads to $\mathbf{v}_\parallel = \mathbf{0}$ and $\nabla v_\perp = 0$ leading to $v_\perp =$ constant. The constraint on volume further guarantees that $v_\perp = 0$. This renders a force-balance condition where the pressure across the surface is balanced by a *constant* and *isotropic* tension on the surface; i.e., the Young-Laplace law for a soap bubble. Thus, in the absence of any patterns, we expect to see no shape changes on the active surface, and the steady state is perfectly spherical.

In all the results that follow, we start with a spherical geometry; the concentration of the stress regulator is homogeneous, with noise of a small relative amplitude. The following non-dimensional quantities emerge from the relevant parameters in the equations:

$$\mathrm{Pe} = \frac{\zeta\Delta\mu}{\gamma D}, \quad \Lambda = \sqrt{\frac{\eta}{\gamma R_0^2}}, \quad \mathcal{B} = \frac{\beta}{\gamma D}, \quad \mathrm{Da} = \frac{kR_0^2}{D}. \tag{4.16}$$

The Péclet number Pe compares the strength of the active advective flows with diffusive transport, L is the ratio of the hydrodynamic length $\sqrt{\eta/\gamma}$ to the radius R_0 of the initial spherical shape, $\mathcal{B}$ is a non-dimensional bending rigidity, finally, Da is the Damköhler number comparing the turnover rate with the diffusive timescale R_0^2/D. In our theoretical results, we report concentration and time in units of c_* and $\tau = \eta/(\gamma D)$. For this chapter, we fix $c_0/c_* = 1$ and $\eta_b/\eta = 5/4$, and start with a spherical surface of radius R_0, and a uniform concentration of c with small random fluctuations. Increasing the Pe, we observe the emergence of spot like patterns (Figure 4.3). It is important to note that a linear perturbation analysis reveals that the $\ell = 1$ spherical harmonic is the fastest growing mode at this instability threshold [Mietke et al., 2019b], and numerical results are in agreement with this analytical prediction. To analyse the full nonlinear dynamics of our active geometrodynamic theory defined by the equations (4.1) - (4.3) and (4.6), we use the finite-element method. We triangulate the surface and use the FEniCS library Alnæs et al. [2015] to solve the resulting discrete system of equations. Time-marching was done

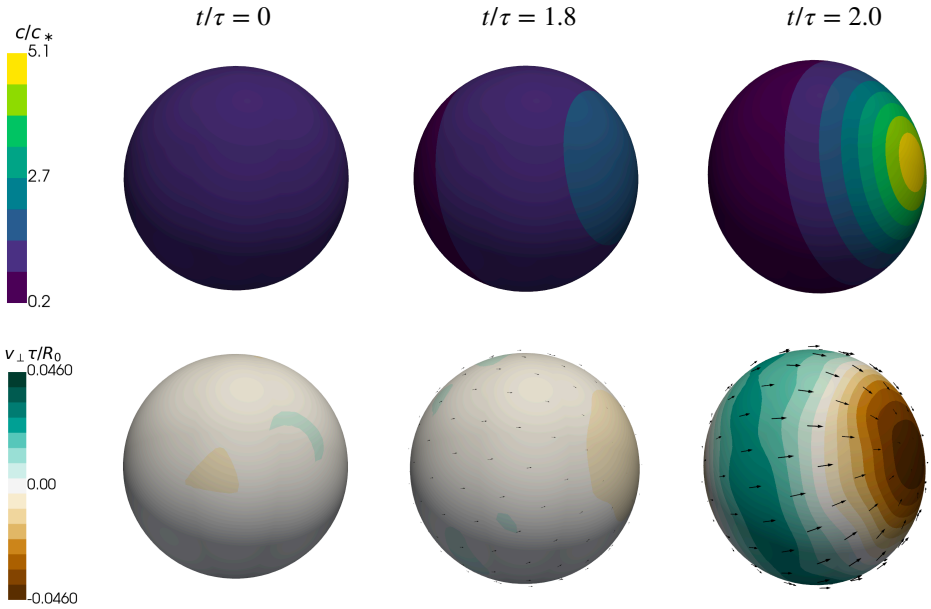

Figure 4.3: Spontaneous spot-like patterns on active surfaces. The top and bottom panels show the dynamics of myosin concentration and the velocity fields on the surface. With the heat map denoting the deformation velocity in the bottom panel $v_\perp$ and the vector field showing the tangential velocity field $\mathbf{v}_\parallel$. For this simulation, $\mathrm{Pe} = 15$, $\Lambda = 0.5$, and $\mathrm{Da} = 0.2$.

using an implicit-explicit scheme. Near the critical Péclet Pe^*, we see very minimal deformations in the surface, this is also in line with the prediction that the pattern forming instability threshold is independent of the strength of bending rigidity $\mathcal{B}$ [Mietke et al., 2019a].

4.3 SELF-ORGANISED CYTOKINETIC PATTERNS IN ACTIVE SURFACES

At larger values of Pe, we see the spontaneous emergence of cytokinesis-like patterns in both the surface geometry and the myosin concentration field $c(\mathbf{x})$. As shown in the top row of Figure 4.4, an initially uniform concentration field with small random perturbations starting from spherical shape spontaneously develops a ring-like pattern of myosin in time. Concomitantly, the geometry of the surface deforms to a shape resembling a cytokinetic furrow. The bottom row of Figure 4.4 shows the spatiotemporal evolution of the active flow $\mathbf{v}(\mathbf{x})$ on the deforming surface: the glyphs represent the tangential velocity $\mathbf{v}_\parallel$ while the heat-map represent the normal velocity $v_\perp$. It is known that at large Pe, inhomogeneities in myosin concentration can accumulate to destabilise the homogeneous state on fixed domains [Bois et al.,

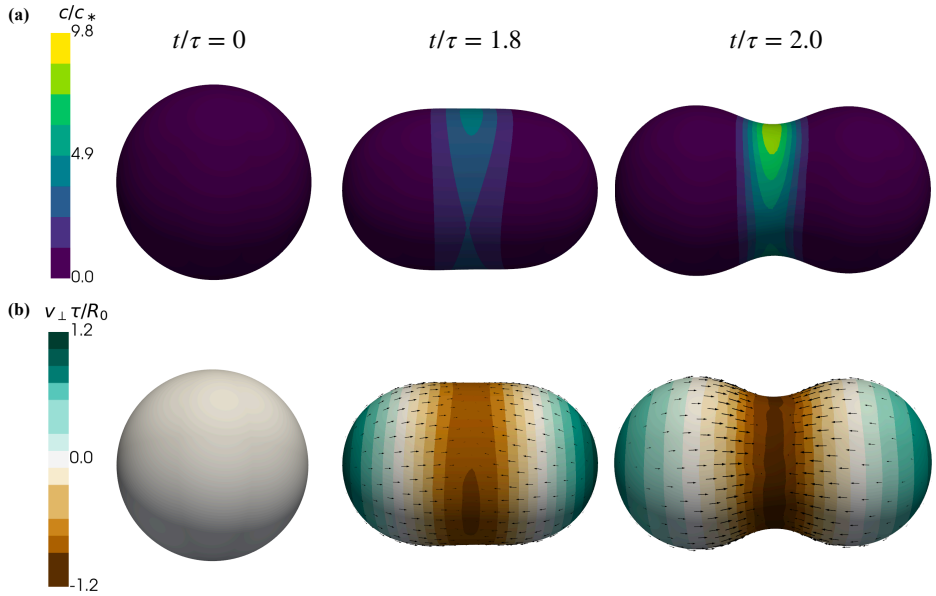

Figure 4.4: Geometrodynamics of an active surface, resulting in cytokinesis. The top panels show the dynamics of myosin concentration on the surface. The bottom panels show the evolution of velocity fields on the surface. With the heat map and glyphs denoting the deformation speed and tangential velocity as before. For this simulation, Pe = 55, $\Lambda = 0.5$, and Da = 0.2.

2011]. However, in our case, the surface also deforms in response to the velocity field associated with these concentration patterns. In

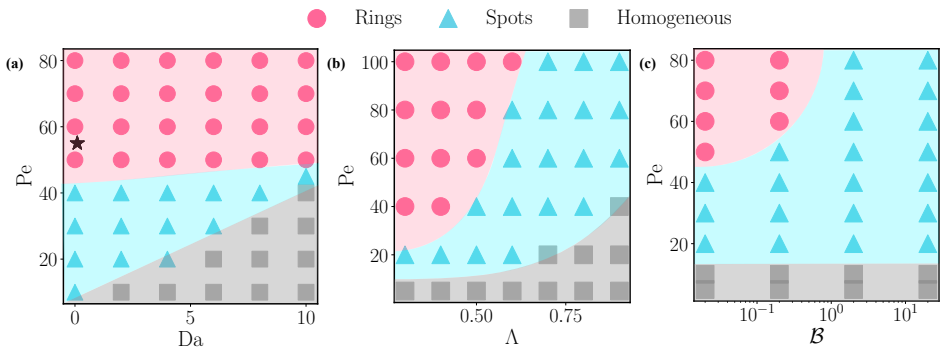

Figure 4.5: Phase diagram with the variations in non-dimensional parameters

Figure 4.5 **a**, we show a phase-diagram of the patterns obtained from our theoretical model as we vary the strength of the active stresses (Pe) and the turnover-rate (Da). At low Pe, the state with a homogeneous concentration and a spherical shape is the stable solution. Upon increasing Pe, we find a spot-like pattern of the concentration and a concomitant deformed shape as the stable solution. At larger Pe, this state undergoes an instability wherein the concentration field self-organizes in the form of a ring-like pattern and the shape in-

gresses continuously. Note that this latter state is not a steady-state solution. Eventually, the surface ingresses to a large extent leading to self-intersections in our numerical implementation, at which point our theory is no longer valid. However, we can follow the kinetics of this ingression process starting from a spherical shape. We observe that during this process, the ring remains planar and is approximately circular. Varying the hydrodynamic length Λ and the bending rigidity $\mathcal{B}$ in Figure 4.5 **(b)** and **(c)**, we find that a broad range of parameters can lead to the emergence of ring-like patterns of concentration and the concomitant furrow-like shapes of the surface

CYTOKINESIS IN *C. elegans* ZYGOTES

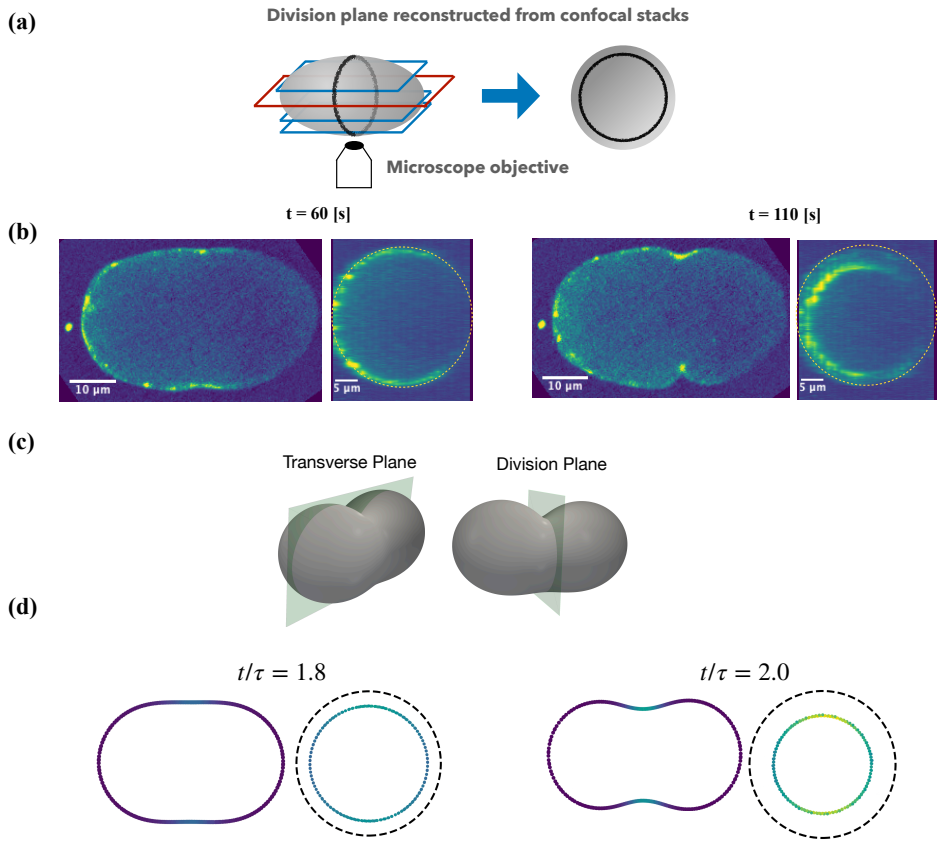

Figure 4.6: Cross-sections of cytokinesis showing the division and transverse planes in experiments **(b)** and theory **(d)**.

To compare the predictions of our theoretical model with experimental data, we consider the first embryonic division in *C. elegans*. We imaged GFP-labelled non-muscle myosin NMY-2 using confocal microscopy (Figure 4.6 **(a)**). Combining several Z-stacks, we obtain

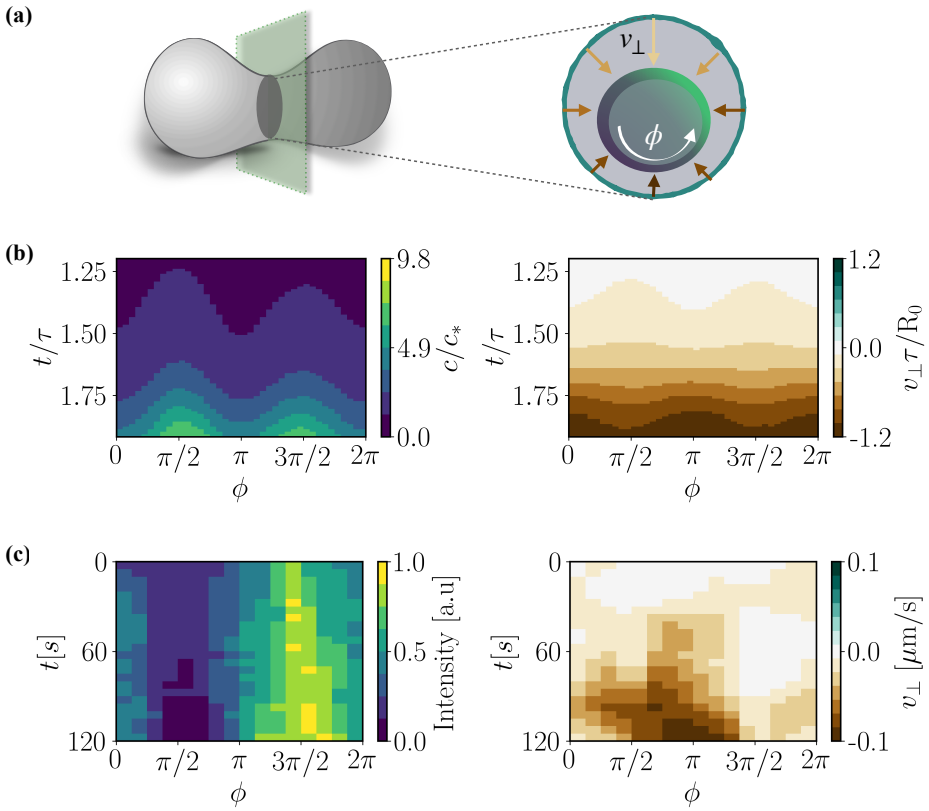

Figure 4.7: Kymographs showing the dynamics of myosin and deformation velocity from theory **(b)** and experiment **(c)**.

the three-dimensional spatiotemporal dynamics of NMY-2::GFP. In Figure 4.6 **(b)**, we plot the cell shape and myosin intensity in the transverse and division planes, at two different time points, as seen in *C. elegans* zygotes. Notice the remarkable similarity in Figure 4.6 **(b)** and Figure 4.6 **(d)** of both the concentration and shape patterns. We immediately notice that the surface ingresses asymmetrically: we will return to this point later. In Figure 4.7 **(b)**, we show the kymograph of the concentration pattern and the ingression rate ($v_\perp$) in the division plane from our numerical calculations. We compare this with the kymographs of the NMY-2::GFP and normal velocity of the contractile ring seen in Figure 4.7 **(c)**.

4.4 SURFACE DYNAMICS IN CYTOKINESIS

Next, we try to look at this self-organised dynamics more quantitatively. To measure the dynamics of the cytokinetic ring, we define the initial ring radius R_0, the ring radius at a particular time t as $R(t)$. Plotting the dynamics of radius with respect to the non-dimensionalised

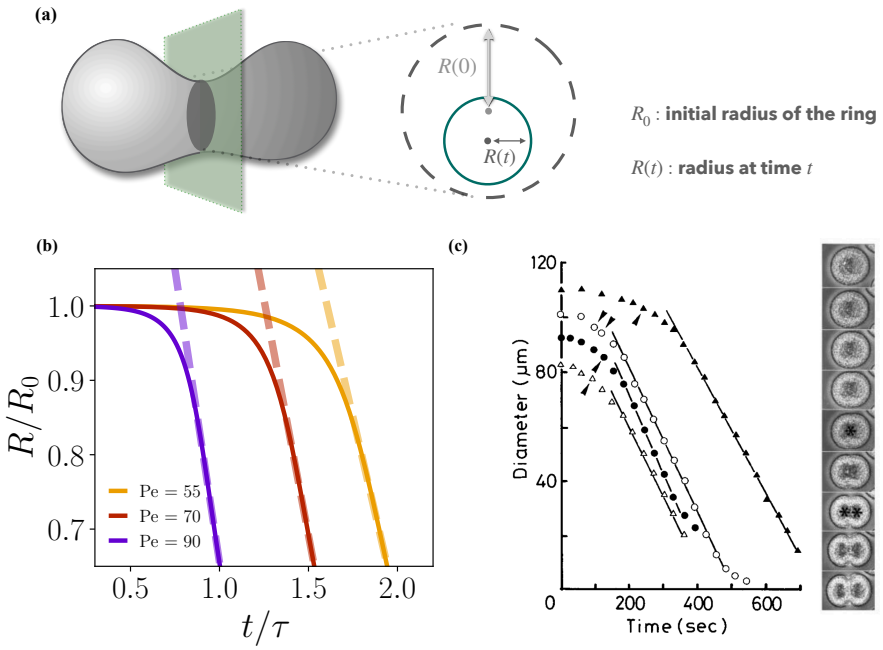

Figure 4.8: (a) Kinetics of radius decrease in self-organised cytokinesis patterns on active surfaces at different values of Pe. (b) Comparison with experimental results from *C. elegans* embryonic cell division under different experimental conditions. (c) Shows the dynamics of ingression during cell division in 4 different sea urchin species. The symbols represent different species as: triangles (empty) representing *A. crassispina*, circles (empty) representing *C. japonicus*, triangles (filled) representing *S. nudus*, and circles (filled) representing *H. pulcherrimus*. Panel (d) is reproduced with permission, from I. Mabuchi, *J. Cell Sci.* (1994) [Mabuchi, 1994] (© The Company of Biologists).

time t/τ where $\tau = \eta/(\gamma D)$, we have two important observations. First, we see that after an initial slow period, the ring constricts at a relatively constant rate, which allows us to identify the constriction rate $u_\perp$, shown in Figure 4.8 (b). This linear decrease in the furrow radius as a function of time seems to be a universally observed feature across several eukaryotes [Mabuchi, 1994; Pelham Jr and Chang, 2002; Biron et al., 2005; Zumdieck et al., 2007; Carvalho et al., 2009; Khaliullin et al., 2018] (see Figure 4.8 **(c)**). Second, we observe that increasing the contractility, i.e., increasing Pe, increases the rate of ingression. This observation is in line with our understanding that a higher contractility implies a faster tangential flow, and also leads to faster deformations of the fluid surface. To test this, we performed RNAi perturbations on the embryo (see Appendix B) to modulate the contractility of the cortex, which affects the strength of the cortical flows [Naganathan et al., 2018]. We perform particle-imaging

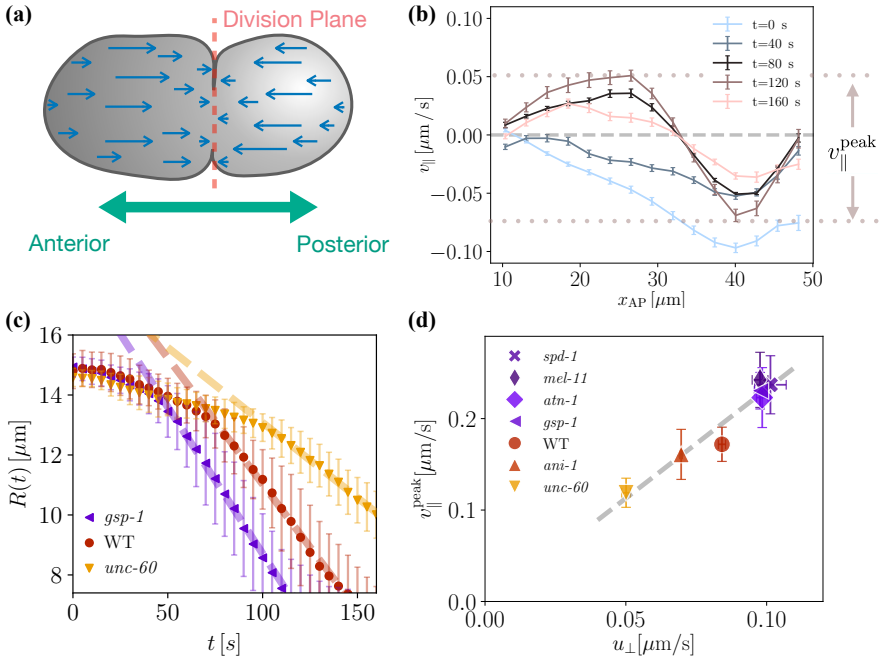

Figure 4.9: **(a)** Convergent flows in the *C. elegans* embryo. **(b)** Average flow velocity measured using Particle Imaging Velocimetry (PIV). Note that flow speed in the anterior to posterior direction is positive, and flow speed in the opposite direction is negative. The flows change sign at the division plane. We identify the maximum convergent flow as the peak-to-peak velocity $v_\parallel^{\text{peak}}$. **(c)** Ingression kinetics is linear across multiple RNAi conditions. **(d)** The ingression speed $u_\perp$ is correlated with $v_\parallel^{\text{peak}}$, indicating higher cortical flows lead to higher ingression speed. Dashed line represents a linear fit to the mean values. The error bars in **(c)** and **(d)** are standard error of the mean with $N = 11$ (WT), $N = 5$ (*spd-1*), $N = 7$ (*mel-11*), $N = 5$ (*atn-1*), $N = 11$ (*gsp-1*), $N = 6$ (*ani-1*), $N = 7$ (*unc-60*).

velocimetry on the experimental data (see Appendix B) to extract the average flows along the anterior-posterior axis of the embryo, shown in Figure 4.9 **(a)**. We notice that the flows intensify as the cytokinesis proceeds, and then diminish towards late stages. We therefore identify the maximum peak-to-peak velocity of the flows as shown in Figure 4.9 **(b)** with $v_\parallel^{\text{peak}}$. Extracting the radius dynamics from projected z-stacks, we confirm that cytokinetic ingression proceeds at a constant rate in experiments as well (4.9 **(c)**). Identifying the ingression speed, $u_\perp$ as we did in the theory, and comparing it against $v_\parallel^{\text{peak}}$, we see in Figure 4.9 **(d)** that both of these observables correlate strongly. As such, in the experimental results that are to follow, we will use $v_\parallel^{\text{peak}}$ as a measure of contractility.

4.5 APPROXIMATE THEORY FOR RING KINETICS

In this section, we derive an approximate theory for the kinetics of the ring radius and the (average) concentration of myosin in the ring. Around the time-point $t = t_{\mathcal{K}}$ where the (average) Gaussian curvature vanishes and the surface starts developing a neck-like region, we derive approximate equations for the ring radius R and the (averaged) myosin concentration c. Note that at $t = t_{\mathcal{K}}$, the summed curvature $\mathcal{H} = 1/R$.

We assume that (i) both the surface shape and the concentration of myosin are azimuthally symmetric in the ring, (ii) the surface variation of the myosin concentration peaks at the location of the ring, (iii) the tangential fluxes of myosin (from advection and diffusion) into the ring balance each other, and (iv) the shape deformations are volume preserving so that $\Delta p \approx 0$. Assumption (i) implies that the myosin concentration is uniform along the ring, assumption (iii) implies $\mathbf{v}_{\parallel} c - D\nabla c = \mathbf{0}$, i.e., the concentration in the ring changes only due to the evolution of geometry, while assumptions (ii) and (iv) imply that $\mathbf{v}_{\parallel} = \mathbf{0}$ on the ring. Since we observe ring-like patterns even when $\kappa = 0$, we neglect myosin turnover.

Dynamics of the ring radius

The force- and torque-balance condition in the normal direction takes the form

$$\left[\nabla \cdot \mathbf{\Sigma}_{\text{viscous}}\right]_{\perp} + \left[\nabla \cdot \mathbf{\Sigma}_{\text{bending}}\right]_{\perp} - \gamma\, v_{\perp} = \zeta\, \Delta\mu\, \mathcal{H}\, f(c). \tag{4.17}$$

We neglect the forces arising from viscous stresses, and for small deviations of the surface around $t = t_{\mathcal{K}}$, we retain terms to lowest order in curvatures while neglecting curvature gradients in the bending stresses (see (4.15)). We then get

$$v_{\perp} \approx \frac{-\zeta\, \Delta\mu\, \mathcal{H}\, f(c) + \beta\, \mathcal{H}^3}{\gamma}. \tag{4.18}$$

The equation governing the shape evolution leads to

$$\frac{dR}{dt} = v_{\perp} \approx -\left(\zeta\, \Delta\mu\, f(c) - \frac{\beta}{R^2}\right)\, \frac{1}{\gamma R}. \tag{4.19}$$

Dynamics of the myosin concentration in the ring

The concentration field evolves only due to the changing geometry (see (4.8)):

$$\partial_t c \approx -\mathcal{H}\, v_\perp\, c, \tag{4.20}$$

which using the above expression for $v_\perp$ leads to

$$\frac{dc}{dt} = \left(\zeta\,\Delta\mu\; f(c) - \frac{\beta}{R^2}\right)\frac{c}{\gamma R^2}. \tag{4.21}$$

Taken together, the above equations for R and c is our approximate theory for the ingression kinetics. We emphasize that these equations are valid only for short times around $t = t_{\mathcal{K}}$.

Rates of ingression and myosin accumulation

If $c \gg c_*$ (which is the case seen in Figure 4.4**a**), then $f(c) \approx 1$. In this case,

$$\frac{dR}{dt} = -\frac{\zeta\,\Delta\mu - \beta/R^2}{\gamma R}, \quad \frac{dc}{dt} = \frac{\zeta\,\Delta\mu - \beta/R^2}{\gamma R}\,\frac{c}{R}. \tag{4.22}$$

We clearly see that for a weakly active surface, i.e., $\zeta\,\Delta\mu/\beta \ll R^{-2}$, the radius R will increase whereas the concentration c will decrease. This represents the relaxation of the deformed surface to a sphere (Figure 4.1). On the other hand, when the activity is large, i.e., $\zeta\,\Delta\mu/\beta \gg R^{-2}$, the radius R decreases while the concentration c increases. The above equations imply that the surface constriction is governed only by the competition between activity dominates bending elasticity. However, note that we have ignored the effects of viscous dissipation and have implicitly assumed that the activity is high enough to have overcome these homogenizing effects.

In the regime where the activity dominates, i.e., $\zeta\,\Delta\mu/\beta \gg R^{-2}$, we neglect the effects of bending elasticity and get

$$\frac{dR}{dt} = -\frac{\omega}{R}, \qquad \frac{dc}{dt} = \frac{\omega\, c}{R^2}, \tag{4.23}$$

where $\omega = \zeta\,\Delta\mu/\gamma$. Solving for $R(t)$ gives

$$R(t) = \sqrt{R_{\mathcal{K}}^2 - 2\,\omega\,(t - t_{\mathcal{K}})}, \tag{4.24}$$

where $R_{\mathcal{K}}$ is the radius of the cytokinetic ring at $t = t_{\mathcal{K}}$. We emphasize that this is *not* the radius of the initial spherical surface, i.e., $R_{\mathcal{K}} \neq R_0$. For short times around $t_{\mathcal{K}}$, a Taylor expansion leads to

$$R(t) \approx R_{\mathcal{K}} \left(1 - \frac{\omega\,(t - t_{\mathcal{K}})}{R_{\mathcal{K}}^2}\right). \tag{4.25}$$

Using $R^2(t) \approx R_{\mathcal{K}}^2$ in the concentration equation, we get

$$c(t) \approx c(t_{\mathcal{K}}) \exp\left(\frac{\omega(t - t_{\mathcal{K}})}{R_{\mathcal{K}}^2}\right). \tag{4.26}$$

These solutions allows us to identify the constant ingression rate $u_\perp$ and the exponential rate k_m of myosin accumulation:

$$u_\perp \approx \frac{\zeta\,\Delta\mu}{\gamma\,R_{\mathcal{K}}}, \qquad k_m \approx \frac{\zeta\,\Delta\mu}{\gamma\,R_{\mathcal{K}}^2} \sim \frac{u_\perp}{R_{\mathcal{K}}}, \tag{4.27}$$

and predict a linear relationship between k_m and $u_\perp$.

Therefore, we have three important predictions from the approximate theory. First, we predict that the rate of ingression should be linear around the time $t = t_{\mathcal{K}}$. Second, we predict that the increase in average myosin in the ring should be exponential. Third, we expect to see a linear relationship between the time constant of exponential increase in myosin k_m and the rate of decrease of the cytokinetic ring radius $u_\perp$

4.6 GEOMETRODYNAMIC FEEDBACK UNDERLYING UNIVERSAL FEATURES OF CYTOKINESIS

To test the quantitative predictions from our approximate theory, in Figure 4.10 **(b)**, we plot the average Gaussian curvature in the ring $\mathcal{K}^{\text{ave}}(t) = \left(\int_{\text{ring}} \mathcal{K}\right) / (2\pi R(t))$ from our theory. We notice that $\mathcal{K}^{\text{ave}}$ decreases from an initial positive value to negative values (indicating the development of a furrow-like shape) at later times. Further, we see that the rate at which $\mathcal{K}^{\text{ave}}$ decreases is an increasing function of the activity, i.e., Pe. To obtain the corresponding data for the *C. elegans* embryo, we performed fluorescence imaging of a GFP-fused PH domain bound to the membrane. This allows us to digitally reconstruct the cell surface as a triangulated mesh, and extract the Gaussian curvature [Cohen-Steiner and Morvan, 2003] (see Appendix B). In Figure 4.10 **(c)**, we see the temporal evolution of the average Gaussian curvature $\mathcal{K}^{\text{ave}}$ in the wild-type (WT) embryo. We notice

that $\mathcal{K}^{\text{ave}}$ is almost zero at initial times, and decreases towards large negative values at later times, indicating the development of the furrow. Note that the negative values of $\mathcal{K}^{\text{ave}}$ at the onset of ingression are due to low signal-to-noise ratio. To test the theoretical prediction about the rate of decrease of $\mathcal{K}^{\text{ave}}$, we performed RNAi to modulate the contractility of the cortex, which affects the strength of the cortical flows [Naganathan et al., 2018]. We see in Figure 4.10 **(c)** that *gsp-1* RNAi embryos (which display enhanced cortical flows) show a faster rate of decrease of $\mathcal{K}^{\text{ave}}$ while this rate decreases in *nmy-2* RNAi embryos (which have reduced cortical flows) compared to WT.

Dyanamics of Gaussian curvature

Next, Figure 4.10 **(d)** shows the evolution of the furrow radius $R(t)$ as a function of time from our theory. We notice that after an initial slow phase, the dynamics of $R(t)$ transitions around $t = t_{\mathcal{K}}$ to a linear decrease with time, thus confirming the first prediction of our approximate theory. This rate is related to the ring-averaged normal velocity of the surface $\int_{\text{ring}} v_{\perp}(t)$. Figure 4.10 **(e)** compares the evolution of $R(t)$ for three different RNAi conditions in the *C. elegans* embryo and shows that $R(t)$ decreases linearly with time, as seen before, consistent with the theory.

We then follow the dynamics of the ring-averaged concentration $m(t) = \left(\int_{\text{ring}} c(t)\right) / (2\pi R(t))$ in Figure 4.10 **(f)**, and notice that it increases exponentially with time $m(t) \sim e^{k_m t}$, thus defining the rate k_m. In Figure 4.10 **(g)**, we plot the NMY-2::GFP intensity across different RNAi conditions in the *C. elegans* embryo and notice that it shows an exponential increase as predicted by our theory.

Dynamics of ring-averaged myosin

We notice from Figure 4.10 **(b)** and **(f)** that the rates $u_{\perp}$ and k_m increase with Pe. We ask if there is a linear relationship between them as predicted by the approximate theory. To answer this, we numerically solved our model equations (4.1) - (4.6) for a range of Pe values, at different values of the turnover rate Da, and the hydrodynamic length-scale Λ, and averaged over random initial conditions. In Figure 4.10 **(a)**, we plot k_m against $u_{\perp}$, where the colour of the symbol maps to different values of Pe, and observe a linear relation as predicted by the above approximate calculation.

We next ask if k_m and $u_{\perp}$ are correlated during cytokinesis in the *C. elegans* zygote. We notice from Figure 4.10 **(c)** and **(e)** that the rates $u_{\perp}$ and k_m vary across RNAi conditions in the embryo. In Figure 4.11 **(b)**, we plot k_m against $u_{\perp}$ extracted from the data in the embryo for different RNAi conditions, where the colour of the symbol now maps to the strength of $v_{\parallel}^{\text{peak}}$. As in the previous section, we use $v_{\parallel}^{\text{peak}}$ as a measure of the contractility. As predicted by our theory, we

Linear relation between $u_{\perp}$ and k_m

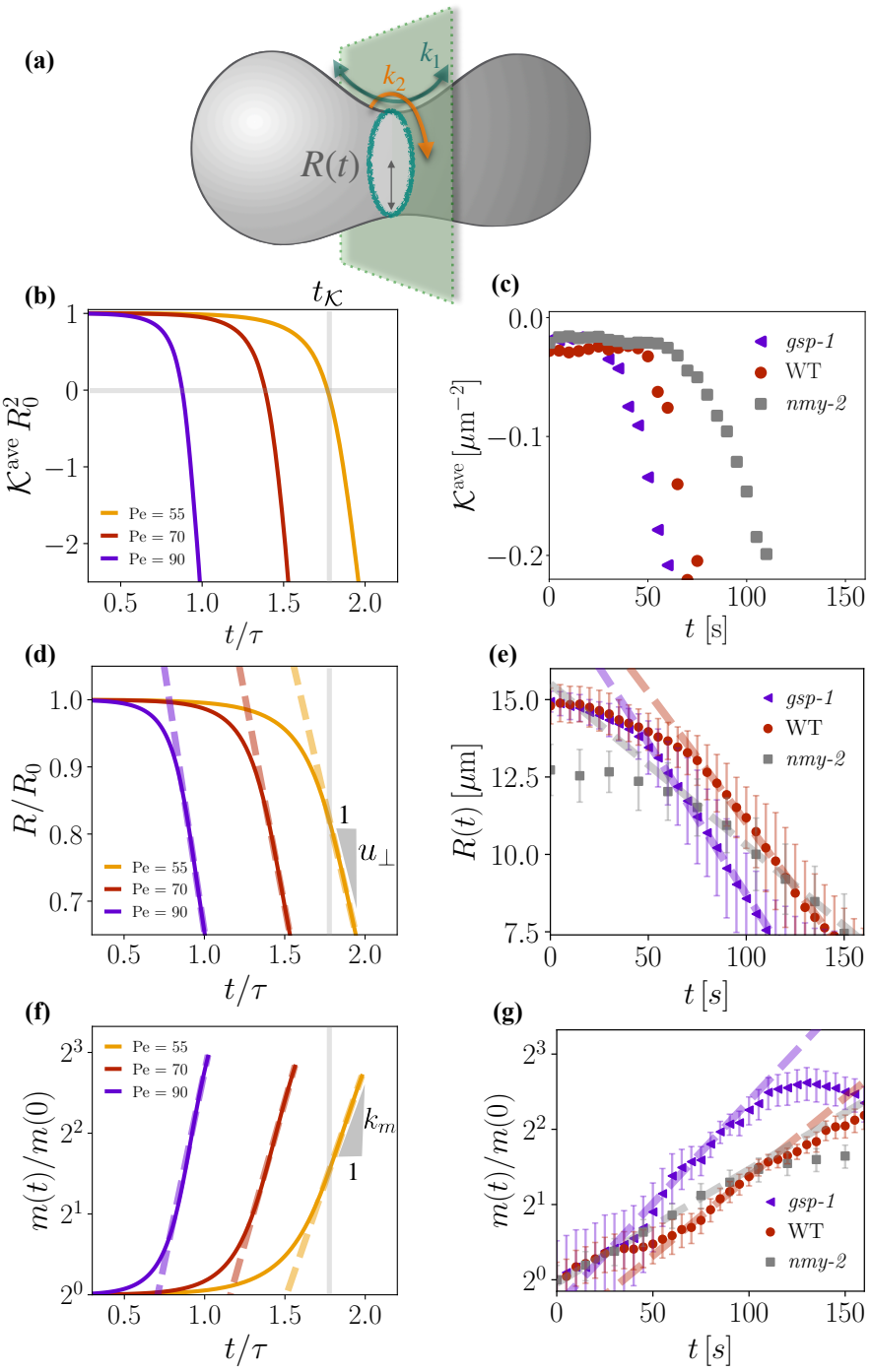

Figure 4.10: **a.** In the division plane, $R(t)$ denotes the radius of curvature of the furrow. The Gaussian curvature of the surface is $\mathcal{K} = k_1 k_2$, where k_1 and $k_2 = 1/R$ are the principal curvatures of the surface. **b.** The ring-averaged Gaussian curvature $\mathcal{K}^{\text{ave}}$ starts from positive values and crosses zero at $t = t_\mathcal{K}$ when the surface starts developing a furrow-like region. The rate of decrease of $\mathcal{K}^{\text{ave}}$ increases with Pe. **c.** Compared to the wild-type (WT) *C. elegans* embryo, the strength of cortical flows is higher in *gsp-1* RNAi embryos and lower in *nmy-2* RNAi embryos. We observe a similar decrease in $\mathcal{K}^{\text{ave}}$. **d.** The radius $R(t)$ of the furrow decreases linearly around $t = t_\mathcal{K}$ and the rate of decrease $u_\perp = -dR/dt$ increases with Pe. **e.** These features are also observed in *C. elegans* embryos. **f.** The ring-averaged myosin concentration $m(t) \sim e^{k_m t}$ shows an exponential increase around $t = t_\mathcal{K}$. **g.** We observe this exponential increase across RNAi conditions. The error bars in **(e)** and **(g)** are standard error of the mean with $N = 11$ (WT), $N = 11$ (*gsp-1*), $N = 11$ (*nmy-2*).

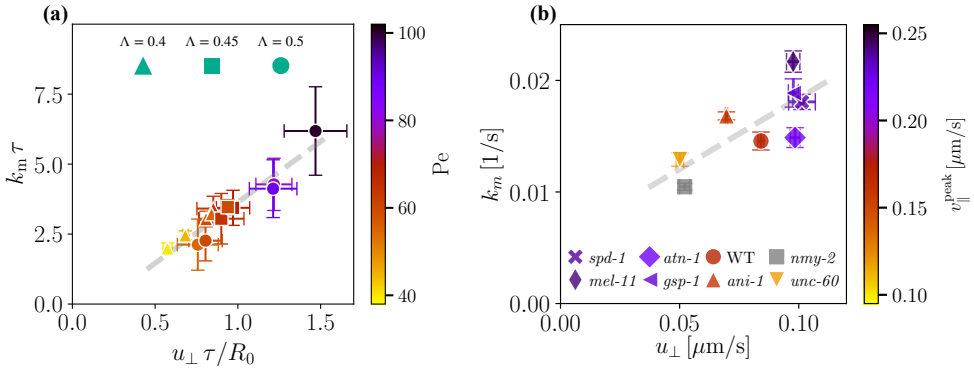

Figure 4.11: **(a)** We plot k_m versus $u_\perp$ over a range of Pe and Λ, and observe a linear relation between them as predicted by the approximate theory in (4.27). Here, the error bars denote standard error over random initial conditions. **(b)** We extract $u_\perp$ and k_m from the fits (dashed-lines) in Figure 4.10**(e)** and Figure 4.10**(g)** respectively and observe that k_m is linear in $u_\perp$. In **(a)**, Da $= 1/10$, and $\mathcal{B} = 1/50$. The error bars in **(b)** are standard error of the mean with $N = 11$ (WT), $N = 5$ (*spd-1*), $N = 7$ (*mel-11*), $N = 5$ (*atn-1*), $N = 11$ (*gsp-1*), $N = 6$ (*ani-1*), $N = 11$ (*nmy-2*), $N = 7$ (*unc-60*).

see a positive linear correlation between k_m and $u_\perp$. Since we have employed NMY2::GFP imaging for the embryos, it is difficult to obtain the flows from PIV for the *nmy-2* RNAi condition due to low intensity values. However, since it involves the direct depletion of myosin, we anticipate the flows to be much lower than in WT embryo. To conclude, the predictions of our theoretical model incorporating the active geometrodynamics of the surface for the self-organized kinetics of ingression agree with experimental measurements. In other words, these results imply that the shape changes during cytokinesis, while initiated by signals, is possibly a self-organized process driven by actomyosin contractility.

4.7 DYNAMICS OF ASYMMETRY IN CYTOKINESIS

We next turn to the asymmetric ingression of the surface that we alluded to earlier [Maddox et al., 2007; Hsu et al., 2023]. Both the concentration pattern of the active stress regulator and the surface geometry seen in Figure 4.6 **(d)**, as well as the spatial maps of NMY-2::GFP and the cross-section of the cell seen in 4.6 **(b)**, show that there are asymmetries during ingression. This is also clearly seen in the kymographs in Figure 4.7.

As shown in Figure 4.12 **(a)**, the deviation Δ of the center of the cytokinetic ring from its initial position, is a quantitative measure of

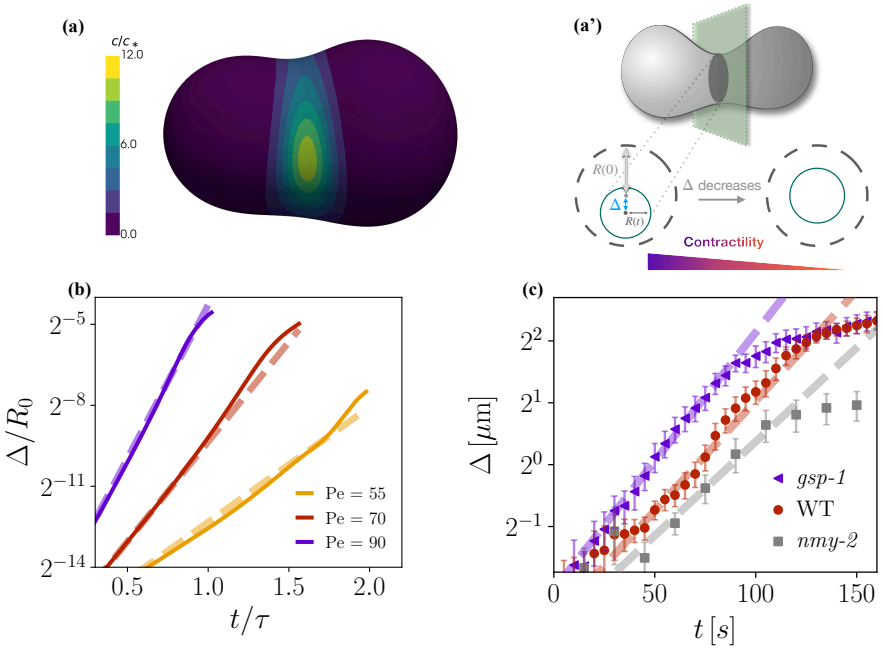

Figure 4.12: **(a)** During cytokinesis, the centre of the cytokinetic ring does not remain fixed. The displacement Δ of the centre of the ring from its location at $t = 0$ is a measure of the asymmetry of ingression. The asymmetry Δ reduces upon decreasing contractility. **b.** From our numerical simulations, we predict an exponential increase $\Delta \sim e^{k_\Delta t}$ of the asymmetry with the rate k_Δ. Furthermore, we predict k_Δ increases with Pe. The error bars are as in Figure 4.10.

this asymmetry [Menon et al., 2017]. In Figure 4.12**(b)**, we plot the temporal evolution of Δ and notice that it increases exponentially, i.e., $\Delta \sim e^{k_\Delta t}$ which defines the rate-constant k_Δ. Figure 4.12 **(c)** shows the variation of Δ with time extracted from the embryo for several RNAi conditions. As predicted by our theory, Δ increases exponentially with time. We further note that k_Δ increases with Pe in the theory and with the strength of the cortical flows in the cell. We now ask if there is a correlation between the rate k_Δ at which the asymmetry increases and the ingression rate $u_\perp$ of the furrow. In Figure 4.13 **(a)**, we plot k_Δ versus $u_\perp$ from our theory, where the colour of the symbols map to the value of Pe. Correspondingly, we plot in In Figure 4.13 **(b)** k_Δ versus $u_\perp$ extracted from the embryo across different RNAi conditions, where the colour of the symbols now represent $v_\parallel^{\text{peak}}$ as defined earlier. We clearly see both from theory and experiment that the rate at which the cytokinetic furrow ingresses asymmetrically is linearly correlated with the ingression rate of the furrow. We expect that small inhomogeneities in the myosin distribution can exist due to inherent noise in a small system such as the cell [Milo et al., 2010]. These initial inhomogeneities can either be amplified due to the geometrodynamic

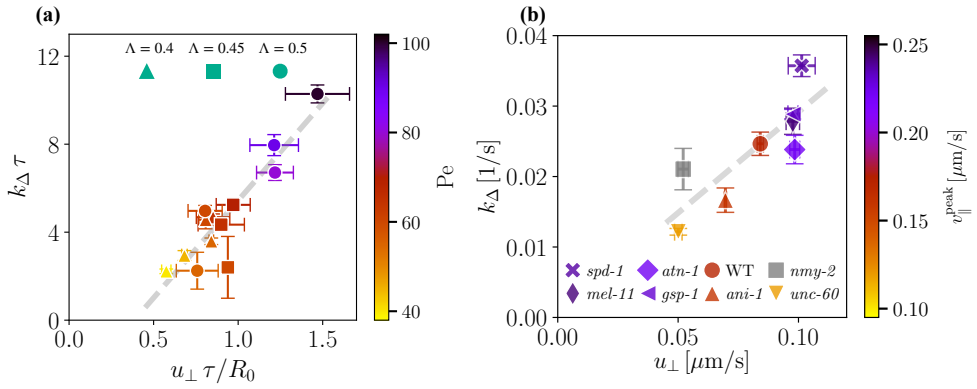

Figure 4.13: **(a)** In our numerical simulations, we find k_Δ increase linearly with the ingression rate $u_\perp$. **(b)** We find that this feature is also observed during the first division of the *C. elegans* embryo across RNAi conditions. Taken together, **a** and **b** imply that embryos with higher contractility (higher $v_\parallel^{\text{peak}}$) show higher asymmetry during ingression. The parameter values and the calculation of error bars are as in Figure 4.11.

feedback arising from active flows, or be suppressed due to relaxation processes such as diffusion or turnover. The amplification will be higher if the cortical contractility is higher, giving rise to a correlation between the rate of asymmetry increase and ingression speed. To summarise, a faster ingression seems to lead to a more asymmetric ingression. We note that changes in the ingression rate, even within our theory, can be brought out by parameters apart from the contractility Pe. We therefore also show in the plots (different markers) an increase/decrease in other parameters, for example, the hydrodynamic length L and the Damköhler number that can lead to increased or decreased flows through different mechanisms, but display the same emergent correlations. The perturbations we have employed affect diverse physical parameters of the cortex [Naganathan et al., 2018]. However, a close match of varied experimental perturbations with our theoretical results strongly suggests that changes in different emergent parameters can lead to similar changes in the geometrodynamic patterns in cytokinesis. Our theoretical model for the self-organized geometrodynamics of the surface not only predicts the ingression of the cytokinetic furrow, but also predicts the concomitant asymmetric ingression, in good comparison with experimental data.

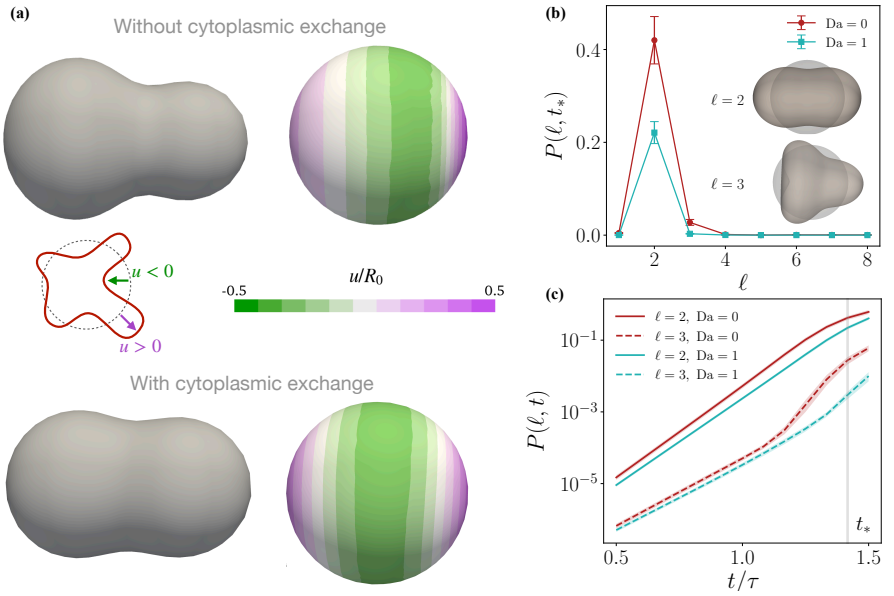

Figure 4.14: In the regime where we observe ring-like constriction patterns of the surface, the positioning of the ingression ring, and hence the geometry of the surface, is controlled by the turnover rate (Da) of myosin with the cytoplasm. When Da $= 0$, we find that the ingression ring is positioned asymmetrically, as shown in the top row. An increase in turnover symmetrizes the position of this ingression ring resulting in equal sized lobes, as shown in the bottom row for Da $= 1$. A quantification of the shape deformation is the radial displacement u, with the visualization of its contours on the base spherical surface. **(b)** Expanding u in spherical harmonics $Y_{\ell m}$, we can obtain the spectral density $P(\ell, t) = \sum_m |u_{\ell m}(t)|^2$ of the deformation field. A plot of $P(\ell, t)$ at a timepoint t_* shows that while $\ell = 2$ is the dominant mode at Da $= 0, 1$, there is a significant contribution of the $\ell = 3$ mode for Da $= 0$. **(c)** The time evolution of $P(\ell, t)$ shows an exponential rise at earlier times. We also notice that $P(\ell = 3, t)$ is enhanced for $t \gtrsim \tau$ for Da $= 0$. Noticing the shapes corresponding to $\ell = 2, 3$ deformations shown in the inset to **(b)**, this clearly indicates as asymmetric positioning of the ring. The errorbars in **(b)** and the shaded regions in **(c)** represent the standard error of the mean computed over $N = 20$ random initial conditions.

4.8 CONTROL OF ASYMMETRIC CELL DIVISION THROUGH CYTOPLASMIC EXCHANGE

Interestingly, we also observe in our theory that the putative "daughter cells" can be different in size (Fig. 4.12 **(a)**). Clearly, this asymmetry is controlled by the positioning of the ingression ring. While the orientation of the division plane emerges spontaneously in our theory, we find that the position of the ingression ring on the active surface can be controlled by cytoplasmic exchange (turnover) rate κ of c. Without cytoplasmic exchange (Da $= 0$), we find that the positioning

of the ingression ring is such the resulting shape of the surface is reminiscent of asymmetric cell division [Knoblich, 2001; Cowan and Hyman, 2004]. With cytoplasmic exchange, however, we find that this asymmetric positioning of the ingression ring is suppressed, i.e., the sizes of the resulting daughter cells are similar. To quantify this asymmetry, we measure the radial displacement u of the deformed surface relative to the initial spherical shape, and visualize it on this reference sphere (Fig. 4.14 **(a)**). We observe that the magnitude of this displacement is similar with and without cytoplasmic exchange. However, the region with maximum ingression is asymmetrically positioned when Da $= 0$, and this asymmetry is reduced when Da $\neq 0$. Further, expanding the displacement field $u = \sum_{\ell m} u_{\ell m}(t)\, Y_{\ell m}(\hat{v})$ in terms of the spherical harmonics $Y_{\ell m}$ (where $\hat{v}$ is the unit normal on the reference sphere), we compute the rotationally invariant spectral density $P(\ell, t) = \sum_m |u_{\ell m}(t)|^2$ to quantify these asymmetries. Fig. 4.14 **(b)** shows $P(\ell, t_*)$ corresponding to the timepoint t_* indicated in Fig. 4.14 **(c)**. We observe that the dominant mode is $\ell = 2$ for both Da $= 0, 1$. However, for Da $= 0$, there is a significant weight in the $\ell = 3$ mode as well. Fig. 4.14 **(c)** shows the time evolution of $P(\ell, t)$ for $\ell = 2, 3$. We notice that $P(\ell = 3, t)$ gets enhanced for $t > \tau$ at Da $= 0$. This clearly indicates asymmetric positioning of the ring. To conclude, in addition to the asymmetric ingression discussed in the previous section, these theoretical results also indicate the possibility of controlling the positioning and stability of the cytokinetic ring using through cytoplasmic exchange.

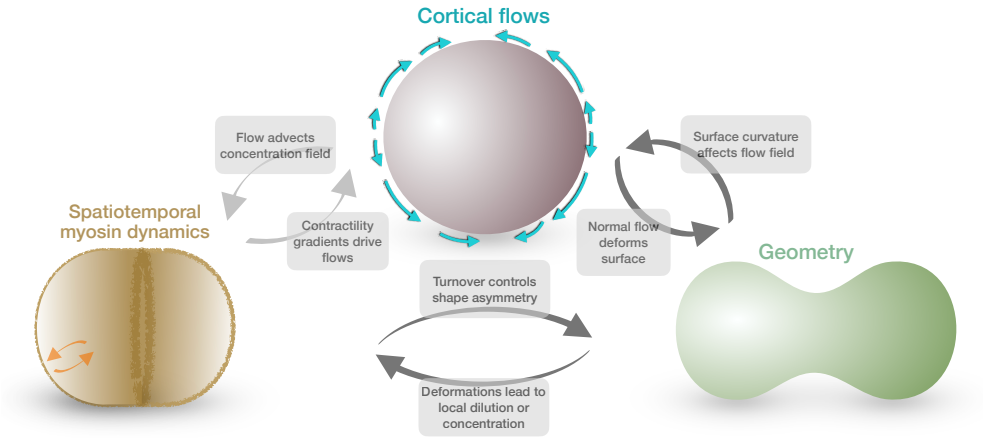

Figure 4.15: A qualitative summary of geometrodynamic feedback underlying cytokinesis in animal cells

This thesis has quantitatively uncovered the coupling between the spatiotemporal dynamics of myosin patterns, the concomitant cortical

flows arising from the spatial gradients of contractility, and the resulting geometrodynamics of the active surface. At high activity strengths (Pe $\gg$ 1), non-trivial patterns of concentration, flows, and shapes emerge spontaneously from the active surface model. Furthermore, asymmetries in concentration patterns enhanced by cortical flows, lead to the emergence of patterns that show asymmetric ingression of the cytokinetic ring and also those that resemble asymmetric cell division. The quantitative comparison with experiments of cytokinesis-like patterns from the theory indicates that active geometrodynamic feedback underlies cytokinesis.

4.9 SUMMARY

We can summarize this chapter's findings by noting the following points.

First, in the theoretical model, we hypothesized that the active stresses responsible for tangential flows on the surface are also the sources for the normal flows that deform the surface. The dynamical geometry of the surface, in turn, has a strong feedback on the patterns of the active stress regulators. We have shown that this tight coupling between active patterns and dynamical shapes – active geometrodynamics – leads to spontaneous formation of cytokinesis like patterns.

Second, the agreement between the theoretical model and experimental data from the *C. elegans* embryo for the ingression kinetics strongly suggests that the underlying physics of cytokinesis is governed by the large-scale self-organized nature of the chemical and shape patterns. In particular, the predictions of the linear decrease in the furrow radius, the exponential increase in the concentration of the active-stress regulator in the ring, and the exponential increase in the asymmetry of the ring that emerge naturally in the theoretical model are confirmed by the data. Moreover, the relationship between the kinetic rates ($u_\perp$, k_m, and k_Δ) predicted by the theory across various parameter values are borne out in the experiment across different RNAi conditions.

Third, consistent with the predictions of a linear stability analysis of the homogeneous state, neglecting cytoplasmic flows [Mietke et al., 2019b; Picardo et al., 2025], the initial patterns of concentration are localized spots, even in the regime where we find rings. However, the non-linearities in the active geometrodynamics of the surface lead to

the merger of these spot-like patterns, resulting in the emergence of a ring-like pattern.

Fourth, though these localized spots merge to form a ring-like pattern, the concentration is not uniform in the ring. Moreover, the positive geometrodynamic feedback between concentration patterns and the surface shape amplifies the inhomogeneities of the concentration in the ring, leading to asymmetries in ingression. In the theory, we find that the enhancement of these inhomogeneities can occur when the active flows are sufficiently strong. In other words, the timescale for the growth of inhomogeneous patterns resulting from active flows should be smaller than the timescales for the homogenization of the concentration by isotropic process such as diffusion and turnover [Thiyagarajan et al., 2022].

Fifth, in the cell, the initiation of cytokinesis is under tight control of the cell-division cycle. The signals for this initiation can be localized in space and time (for instance, through positioning of the spindle) or lead to global changes in material properties (such as contractility) of the cortex at appropriate temporal checkpoints [Fischer-Friedrich et al., 2016]. However, these results suggest that once cytokinesis is initiated, the subsequent spatiotemporal patterns of the active-stress regulators and the geometry of the cell surface could result from a self-organized dynamics.

5

CONCLUSION

5.1 SIGNALLING, CONTROL, SELF-ORGANISATION

In this thesis, we have tried to understand the universal features of cytokinesis resulting from the interplay between active mechanochemical patterns and the dynamical geometry of the cell surface. In animal cells, cytokinesis is under tight control in both time and space [Bement et al., 2005; Clark and Paluch, 2011]. With this in mind, we repeat the question asked in the first chapter: could self-organised active dynamics underlie general features observed in cytokinesis? Our theoretical results strongly suggest this possibility. We know from early experiments that signals emanating from the spindle initiate cytokinesis. However, the continued presence of these signals is perhaps dispensable once the cell surface deforms beyond a threshold [Swann and Mitchison, 1953; Hiramoto, 1956]. Strikingly, there are experiments demonstrating the emergence of a cytokinetic ring-like structure in unfertilised sea urchin embryos upon treatment with Calyculin A (which presumably increases the activity of myosin in the cell) [Tosuji et al., 1992]. In our theory, an increase in the actomyosin contractility leads to the spontaneous emergence of rings. Further, we note that asymmetries in cytokinesis arise naturally in our theory when the contractility is high. However, in big (radius $> 200\,\mu$m) cells, this asymmetry could be controlled by the asymmetric localisation of a comparatively smaller spindle which activates the surface [Rappaport, 1996].

5.2 CONFINEMENT, ACTIN ALIGNMENT, AND CYTOPLASMIC FLOWS

The minimal theoretical model for the geometrodynamics of the surface considered in this study neglects several realistic features of the cell. We first notice that the cytokinetic furrow has a high curvature in the *C. elegans* embryo compared to the theoretically predicted shape.

Confinement due to eggshells

This contrast possibly arises because the embryo is confined in an eggshell, which prevents the daughter cells from moving apart. A few studies indicate that removing this eggshell leads to a lower curvature in the ingression furrow [Koyama et al., 2012].

Filament alignment and anisotropic stresses

Second, in our theory, we have neglected the nematic alignment of actin filaments in the cytokinetic ring [Reymann et al., 2016; Spira et al., 2017] and have considered an isotropic active stress in the tangent plane of the surface. Our experiments in the embryo show that the tangential component of the cortical flows towards the ring decreases after the onset of cytokinesis (Figure 4.9). However, our theory predicts a monotonic increase in the magnitude of the tangential flows $\mathbf{v}_\parallel$, well beyond the onset of furrow ingression. It is possible that including the dynamics of the orientational degrees of freedom of the actomyosin cortex, and the associated anisotropic active stresses, might reduce the tangential flows from the poles towards the ring. During asymmetric (unilateral) ingression, the actin filaments are also reported to align close the furrow [Schroeder, 1968]. Using agent-based models, theoretical studies have proposed that there exists a feedback mechanism between the surface curvature and actin alignment that can give rise to asymmetric ingression [Dorn et al., 2016], since the actin filaments are expected to have a preferential alignment along the divison plane of the cell. This feedback is missing in our theory, and studying the impact of anisotropic stresses on active geometrodynamics could possibly lead to very interesting avenues.

Cytoplasmic flows

Third, previous theoretical studies have shown that including cytoplasmic flows can lead to the emergence of ring-like patterns of the concentration field [Greenspan, 1977; Mietke et al., 2019a]. However, this mechanism requires a strong coupling between the cortical and cytoplasmic flows, with ring-like patterns emerging when $\eta/(\mu R_0) \ll 1$, where μ is the cytoplasmic shear viscosity. Using values of the cortical shear viscosity obtained in other cells [Turlier et al., 2014] and considering appropriate values for the shear viscosity of the cytoplasmic fluid [Charras et al., 2009], we estimate $\eta/(\mu R_0) \sim 10$ for the *C. elegans* embryo. This indicates that ring-like patterns are unlikely to emerge from a strong coupling between cortical and cytoplasmic flows. However, the ratio $\eta/(\mu R_0)$ can be smaller for cells much larger than *C. elegans* embryo. This suggests a stronger coupling between cytoplasm and cortex. From recent experimental and theoretical results [Wu et al., 2024; Liao and Lauga, 2024], it is also clear that the cytoplasmic flows play a central role in spindle positioning during cytokinesis. In

large cells, therefore, coupling between cytoplasmic and cortical flows could also have a major impact on the asymmetry of ingression.

Fourth, this work demonstrates that the active geometrodynamic framework developed here also leads to the emergence of asymmetric division spontaneously. Asymmetric cell division is typically preceded by the establishment of cell-polarity involving complex chemical interactions between the species involved [Gross et al., 2019]. On the other hand, we have considered a simple linear turnover reaction with a rate constant κ. When coupled with active deformations, we observe that the absence of cytoplasmic exchange ($\kappa = 0$) leads to an emergent asymmetry in the sizes of the putative daughter cells. In the presence of cytoplasmic exchange ($\kappa \neq 0$), this asymmetry is reduced. This result is in line with experimental evidence suggesting that myosin turnover stabilizes cytokinetic rings [Thiyagarajan et al., 2022].

5.3 CYTOKINESIS IN RECONSTITUTED SYSTEMS?

The self-organised nature of cytokinetic ingression that we have demonstrated in this thesis indicates that cytokinesis-like patterns could arise in synthetic systems as well [Baldauf et al., 2022]. In studies on reconstituted systems, spontaneous patterns of localised myosin and travelling waves have been reported [Vogel et al., 2020; Abu Shah and Keren, 2014]. These reconstituted cortices also display a spontaneous emergence of motility [Sakamoto et al., 2022], and even the emergence of actomyosin rings [Miyazaki et al., 2015]. However, these actomyosin rings do not show any ingression of the surface or subsequent division, possibly due to the lack of a strong coupling between the enclosing membrane and the reconstituted meshwork. The results from this thesis indicate that active patterns on static peanut-shaped geometries, and self-organised active geometrodynamics could be relevant to observe cytokinesis of these synthetic "cells".

5.4 AN EVOLUTIONARY OUTLOOK

This thesis focused on the physics of cytokinesis. As we have demonstrated, cytokinesis-like patterns can occur spontaneously due to an instability of the state with homogeneous myosin and isotropic shape. Clearly, the cell controls the initiation of cytokinesis by coupling to genetic regulatory mechanisms. During the course of evolution, the addition of mechanisms to control this initiation was a slow, and

step-wise process [Krylov et al., 2003]. Studying cellular mechanisms in embryos is therefore of special interest, since they are expected to be transcriptionally silent. Embryonic cell divisions, therefore, offer a great deal of insight about cellular self-organisation. The vast range of sizes in embryos allows for the exploration of different physical principles operating at larger length-scales.

Our work demonstrates that the physics of active deformable surfaces underlies cellular morphogenesis. We expect similar principles to underlie shape dynamics at the scale of tissues, wherein gradients of myosin activity can drive tissue morphogenesis [Streichan et al., 2018; Gehrels et al., 2023]. One can hope that the dynamical feedback between geometry and active forces will help reveal more general principles that underlie the origin of shape and form in the living world around us [Thompson, 1917].

APPENDIX

A

MATHEMATICAL NOTATION

In $\mathbb{R}^3$, given a scalar field $\varphi(\mathbf{x})$, vector fields $\mathbf{u}(\mathbf{x}) = \sum_i u_i(\mathbf{x})\,\hat{\mathbf{e}}_i$ and $\mathbf{v}(\mathbf{x}) = \sum_i v_i(\mathbf{x})\,\hat{\mathbf{e}}_i$ with $\hat{\mathbf{e}}_i$ being the orthonormal Cartesian basis vectors, and second-rank tensor fields $\mathbf{A}(\mathbf{x}) = \sum_{i,j} A_{ij}(\mathbf{x})\,\hat{\mathbf{e}}_i \otimes \hat{\mathbf{e}}_j$ and $\mathbf{B}(\mathbf{x}) = \sum_{i,j} B_{ij}(\mathbf{x})\,\hat{\mathbf{e}}_i \otimes \hat{\mathbf{e}}_j$ with $\otimes$ being the tensor product, we use the following notations

$$\mathbf{u} \cdot \mathbf{v} \equiv \sum_i u_i\, v_i, \tag{A.1}$$

$$\mathbf{u} \cdot \mathbf{A} \equiv \sum_{i,j} u_i\, A_{ij}\, \hat{\mathbf{e}}_i, \qquad \mathbf{A} \cdot \mathbf{u} \equiv \sum_{i,j} A_{ij}\, u_j\, \hat{\mathbf{e}}_i, \tag{A.2}$$

$$\mathbf{A} \cdot \mathbf{B} \equiv \sum_{i,j,k} A_{ik}\, B_{kj}\, \hat{\mathbf{e}}_i \otimes \hat{\mathbf{e}}_j, \qquad \mathbf{A} : \mathbf{B} \equiv \sum_{i,j} A_{ij}\, B_{ij}. \tag{A.3}$$

Then the derivatives in $\mathbb{R}^3$ are

$$\nabla_3 \varphi = \sum_i \partial_i \varphi\, \hat{\mathbf{e}}_i, \tag{A.4}$$

$$\nabla_3 \mathbf{u} = \sum_{i,j} \partial_i u_j\, \hat{\mathbf{e}}_i \otimes \hat{\mathbf{e}}_j, \qquad (\nabla_3 \mathbf{u})^{\mathsf{T}} = \sum_{i,j} \partial_j u_i\, \hat{\mathbf{e}}_i \otimes \hat{\mathbf{e}}_j \tag{A.5}$$

$$\nabla_3 \mathbf{A} = \sum_{i,j,k} \partial_i A_{jk}\, \hat{\mathbf{e}}_i \otimes \hat{\mathbf{e}}_j \otimes \hat{\mathbf{e}}_k, \tag{A.6}$$

which lead to the advective terms

$$\mathbf{v} \cdot \nabla_3 \varphi = \sum_i v_i\, (\partial_i \varphi), \tag{A.7}$$

$$\mathbf{v} \cdot (\nabla_3 \mathbf{u}) = \sum_{i,j} v_i\, \partial_i u_j\, \hat{\mathbf{e}}_j = \sum_{i,j} v_j\, \partial_j u_i\, \hat{\mathbf{e}}_i = (\nabla_3 \mathbf{u})^{\mathsf{T}} \cdot \mathbf{v}, \tag{A.8}$$

$$\mathbf{v} \cdot (\nabla_3 \mathbf{A}) = \sum_{i,j,k} v_i\, \partial_i A_{jk}\ \hat{\mathbf{e}}_j \otimes \hat{\mathbf{e}}_k. \tag{A.9}$$

B

NUMERICAL FORMULATION

The membrane-cortex composite is treated as a fluid surface Γ. The geometry of this surface is changed by the local normal velocity $\mathbf{v}_\perp \equiv v_\perp \hat{\mathbf{n}} = \mathbf{v} - \mathbf{v}_\parallel$. Thus a material point $\mathbf{x}$ on Γ evolves according to:

$$\frac{d\mathbf{x}}{dt} = v_\perp \, \hat{\mathbf{n}}. \tag{B.1}$$

As the surface deforms, its geometry changes. The evolution equation for the unit normal vector field is given by

$$\frac{\partial \hat{\mathbf{n}}}{\partial t} + \nabla v_\perp = 0. \tag{B.2}$$

The surface velocity field $\mathbf{v}$ arises from force and torque balance conditions:

$$\nabla \cdot \boldsymbol{\Sigma} - \gamma \mathbf{v} - \Delta p \, \hat{\mathbf{n}} - \mathbf{F}_{\text{CM}} \cdot (\hat{\mathbf{n}} \otimes \hat{\mathbf{n}}) = 0, \tag{B.3}$$

where the Lagrange multipliers Δp and $\mathbf{F}_{\text{CM}}$ ensure, respectively, that the volume enclosed by the surface does not change and the centre-of-mass does not move. The volume constraint is implemented by

$$\int_\Gamma v_\perp = 0, \tag{B.4}$$

while the constraint to hold the centre-of-mass fixed is implemented by

$$\int_\Gamma (v_\perp \, \hat{\mathbf{n}}) = \mathbf{0}. \tag{B.5}$$

The hydrodynamic stress has viscous, bending and active contributions. The viscous stress is

$$\boldsymbol{\Sigma}_{\text{viscous}} = 2\eta \, \mathbf{E} + (\eta_b - \eta) \, \text{Tr}(\mathbf{E}) \, \mathbf{P}, \tag{B.6}$$

where η and η_b are, respectively, the shear and bulk viscosities, and the surface strain-rate $\mathbf{E} = \left(\nabla\mathbf{v} + (\nabla\mathbf{v})^{\mathsf{T}}\right)/2$. The bending stress

$$\boldsymbol{\Sigma}_{\text{bending}} = \beta\,\mathcal{H}\left[(\mathcal{H}\,\mathbf{P} - 2\mathbf{S}) + 2\nabla\mathcal{H}\otimes\hat{\mathbf{n}}\right]. \tag{B.7}$$

where β is the bending rigidity and $\mathcal{H}$ is the mean curvature. The active stress is regulated by the concentration field c of myosin motors and is given by

$$\boldsymbol{\Sigma}_{\text{active}} = \zeta\Delta\mu\,\frac{c}{c + c_*}\,\mathbf{P}, \tag{B.8}$$

where $\zeta\Delta\mu$ is an activity coefficient and c_* is a saturation concentration. The myosin concentration itself evolves according to

$$\frac{\partial c}{\partial t} + \nabla\cdot(\mathbf{v}c) - D\nabla^2 c + \kappa\,(c - c_0) = 0, \tag{B.9}$$

where D is the diffusion constant, κ is the turnover rate, and c_0 is a set-point concentration.

Equations (B.1), (B.2), (B.3), (B.4), (B.5), and (B.9) completely specify our theory for active deformable surfaces, given an initial shape and an initial concentration field. However, we find solving the above equations along with (2.19) and (2.28) for the geometrical quantities $\mathbf{P}$ and $\mathbf{S}$ leads to better numerical stability.

To numerically solve our model, we first discretize the surface Γ by a triangulated mesh. We then reformulate the dynamical equations into a weak-form suitable for an implementation via the finite-element method. We use the FEniCS library [Alnæs et al., 2015] to carry out the actual implementation of the FEM. For time-evolution, we used a first-order implicit-explicit method.

To check the evolution of geometrical quantities, we consider a specified time-dependent deformation of the surface Γ parametrized by

$$\mathbf{x}(\theta,\phi) = \left[R_0 + \alpha\,\sin\omega t\;Y_m^\ell(\theta,\phi)\right]\,\hat{\mathbf{n}},$$

where R_0 is the radius of the base sphere, α and ω are, respectively, the amplitude and rate of the deformation, and $Y_m^\ell(\theta,\phi)$ is a real spherical harmonic. This allows us to exactly compute $\hat{\mathbf{n}}(\mathbf{x},t)$, $\mathbf{P}(\mathbf{x},t)$, and $\mathbf{S}(\mathbf{x},t)$. We then numerically solve the time-evolution of the geometrical quantities via (B.2), (2.19) and (2.28), and compare with the analytical solutions to find appropriate convergence of the errors, defined to be L_E^2/S_{ar}, where L_E^2 represents the maxima of L^2 norm

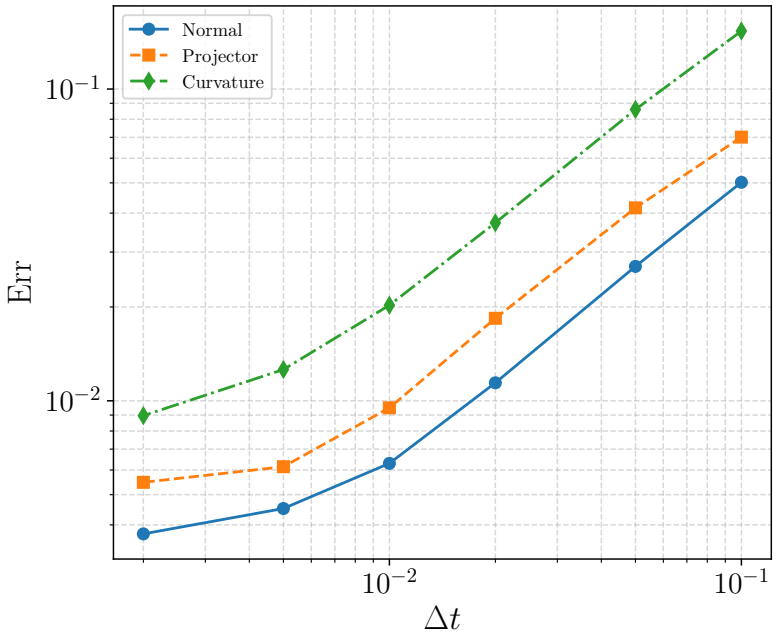

Figure B.1: Numerical convergence of errors for time evolution of $\hat{\mathbf{n}}$, $\mathbf{P}$, and $\mathbf{S}$

of the error and S_{ar} is the surface area of the surface mesh. This is necessary as the spherical harmonic deformations which the mesh is subjected to do not preserve the surface area. We then find the maxima of this error, referred to as Err, and plot against with refinement in time-step Δt in Fig. B.1. The convergence trends that follow are as expected from a first-order scheme.

C

EXPERIMENTAL METHODS AND ANALYSIS

EXPERIMENTAL METHODS

The experiments in chapter 4 of this thesis were performed by Prof. Masatoshi Nishikawa at the Hosei University, Tokyo. In this section is a summary of the culture assays for worms and the imaging techniques involved. The analysis of the data resulting from these experiments and the comparison with theory is part of the work reported in this thesis.

Worm strains and culture

C. elegans strains were maintained at 20°C and shifted to 25°C for 24 hr under nonRNAi condition. RNAi was performed via feeding, as described in [Naganathan et al., 2018]. Feeding durations were 9-10 hr for *unc-60*, 16-18 hr for *nmy-2*, and 27-29 hr for *ani-1*. For *atn-1*, *gsp-1*, *mel-11*, and *spd-1*, feeding was conducted for 29-31 hr at 25°C. The following transgenic strains were used: LP162 for NMY-2::GFP imaging, and LP306 for imaging GFP-tagged PH domain for plasma membrane imaging.

Time-lapse imaging

Z-stack confocal images were acquired using a Nikon Ti2-E microscope with a Yokogawa CSU-W1 spinning disk unit, a NIDAQ-triggered Piezo Z-stage (MCL Nano-Z-100-N2), and a Nikon PlanApo 60× water-immersion objective (N.A. 1.2). Images were captured by an sCMOS camera (Hamamatsu ORCA-Fusion) at 256 × 256 pixels, using 2 × 2 binning from an original 512 × 512 pixel region. GFP-tagged proteins in zygotes were excited with a 488 nm diode laser. For NMY-2::GFP imaging, the laser power was 15 mW (30 mW for *nmy-2* RNAi), with a

40 ms exposure. Z-stacks of 20 slices at 1.5 μm intervals were acquired every 5 s (15 s for *nmy-2* RNAi). For GFP-PH domain imaging, a 4 mW laser with a 20 ms exposure was used; 10-slice Z-stacks at 1 μm spacing were acquired every 5 s.

One-cell embryos were dissected from young adults in M9 buffer and mounted between a coverslip and slide using 25 μm spacer beads (for NMY-2 imaging) or 10 μm beads (for PH domain imaging), sealed with VALAP. Smaller beads were used to bias ingression initiation from the lateral side; larger beads were used to suppress embryo rotation before cytokinesis onset.

ANALYSIS OF EXPERIMENTAL DATA

Analysis of ring structure and myosin dynamics

The Z-stacks obtained from confocal microscopy were projected, rotated by 90°, and interpolated in space using the 3D projection plugin of the open-source software Fiji [Schindelin et al., 2012]. The image was then binarised and segmented using the multi-otsu thresholding algorithm through the *scikit-image* library in Python[Liao et al., 2001; Van der Walt et al., 2014]. The segmented pixels identified to belong to the ring were then fitted to obtain a circle using a total least squares estimator implemented in scikit image [Jekel, 2016], rendering the radius and position of the center of the cytokinetic ring which, when multiplied with the pixel length p_l render the structural parameters $R(t)$ and $\Delta(t)$, representing the ring radius and asymmetry respectively.

To measure the myosin intensity, a 10 pixel wide region around the fitted circle representing the cytokinetic ring was masked. The total intensity in this masked region was then calculated by adding the individual pixel intensity and multiplying the pixel area p_l^2. To estimate the ring myosin intensity per unit length $m(t)$, the total intensity was ten divided by the estimate of the ring perimeter given by $2\pi R(t)$.

Surface reconstruction and estimation of Gaussian curvature

For each time point and z-slice, Otsu thresholding was applied to create a binary mask of the GFP-PH signal using the scikit-image library. The resulting mask was processed with a Canny edge detector ($\sigma = 2$) to obtain high-contrast outlines of the membrane. These binary

edge images were then analysed using OpenCV to identify external contours [Bradski, 2000], and the largest connected contour in each slice was rendered at a thickness of one pixel.

To reconstruct the three-dimensional embryo surface, each contour pixel was converted into a 3D coordinate by scaling the x and y pixel indices using the known pixel size and assigning the z-coordinate according to the slice index. All contour points from a given time point were aggregated into a 3D point cloud. Surface meshes were reconstructed from these point clouds using the vedo library [Musy et al., 2021]. Gaussian curvature was computed for each reconstructed mesh using the angle-deficit formulation implemented in the trimesh library[Cohen-Steiner and Morvan, 2003; Dawson-Haggerty et al., 2019]. For each vertex, the discrete Gaussian curvature was calculated as the angular deficit and then normalized by the corresponding barycentric vertex area (defined as $A_v = \sum_f (A_f/3)$ where f represents a face connected to the vertex and A_f is the area corresponding to the face). The final expression for the Gaussian curvature $\mathcal{K}$ at a vertex v is given by:

$$\mathcal{K}_v = \frac{2\pi - \sum_f \theta_f}{A_v},$$

where θ_v is the angle between of edges connecting the face f with the vertex v. The axes of symmetry of the reconstructed mesh were determined using principal component analysis (PCA) as implemented in the scikit-learn library [Pedregosa et al., 2011]. Roughly 10 percent of the total vertices that that were closest to the axis of symmetry approximately aligning with the long axis of the embryo were chosen. A further subsampling of about half of these vertices, closest to the middle of the z-stack, were chosen to represent the average ring Gaussian curvature. This further reduction was to ensure the curvature values do not get dominated by vertices close to the mesh edge. Therefore, the average Gaussian curvature in the ring is $\mathcal{K}^{\text{ave}} = \langle \mathcal{K}_v \rangle$ where $\langle \dots \rangle$ represents the average over all the preidentified vertices.

Particle Imaging Velocimetry

Particle Image Velocimetry was performed on the bottom-planes of the z-stacks using PIVlab in MATLAB with the FFT window-deformation algorithm [MathWorks, 2024; Thielicke and Sonntag, 2021]. Image pairs were processed using contrast-limited adaptive histogram equal-

ization (CLAHE, 64-px tiles). Vector fields were computed using a two-pass interrogation scheme: an initial 32×32 pixel interrogation window with a 16 pixel step, followed by a refined pass using 24×24 px windows with a 12 pixel step. The Gaussian 2×3-point estimator was used for subpixel peak detection, and the standard correlation-robustness setting was enabled. The resulting 2D vector fields were averaged along the y-axis (with the x-axis aligned with the Anterior-Posterior axis of the embryo) to obtain cortical flows towards the cytokinetic ring.

BIBLIOGRAPHY

Enas Abu Shah and Kinneret Keren. Symmetry breaking in reconstituted actin cortices. *Elife*, 3:e01433, 2014.

Sami C. Al-Izzi and Richard G. Morris. Morphodynamics of active nematic fluid surfaces. *Journal of Fluid Mechanics*, 957:A4, 2023.

Bruce Alberts, Rebecca Heald, Alexander Johnson, David Morgan, Martin Raff, Keith Roberts, and Peter Walter. *Molecular biology of the cell: seventh international student edition with registration card*. WW Norton & Company, 2022.

Martin S. Alnæs, Jan Blechta, Johan Hake, August Johansson, Benjamin Kehlet, Anders Logg, Chris Richardson, Johannes Ring, Marie E. Rognes, and Garth N. Wells. The FEniCS project version 1.5. *Archive of Numerical Software*, 3(100):9–23, 2015.

John M Arnold. Cleavage furrow formation in a telolecithal egg (loligo pealii) i. filaments in early furrow formation. *The Journal of cell biology*, 41(3):894–904, 1969.

Lucia Baldauf, Lennard Van Buren, Federico Fanalista, and Gijsje Hendrika Koenderink. Actomyosin-driven division of a synthetic cell. *ACS Synthetic Biology*, 11(10):3120–3133, 2022.

William M Bement, Hélène A Benink, and George Von Dassow. A microtubule-dependent zone of active rhoa during cleavage plane specification. *The Journal of cell biology*, 170(1):91–101, 2005.

Archit Bhatnagar, Michael Nestler, Peter Gross, Mirna Kramar, Mark Leaver, Axel Voigt, and Stephan W Grill. Axis convergence in c. elegans embryos. *Current Biology*, 33(23):5096–5108, 2023.

David Biron, Pazit Libros, Dror Sagi, David Mirelman, and Elisha Moses. Cytokinesis: The initial linear phase crosses over to a multiplicity of non-linear endings: Biphasic cytokinesis and cooperative single cell reproduction. In *Forces, Growth and Form in Soft Condensed Matter: At the Interface between Physics and Biology*, pages 217–234. Springer, 2005.

Justin S Bois, Frank Jülicher, and Stephan W Grill. Pattern formation in active fluids. *Physical Leview Letters*, 106(2):028103, 2011.

Karine G Bourdages, Benjamin Lacroix, Jonas F Dorn, Carlos P Descovich, and Amy S Maddox. Quantitative analysis of cytokinesis in situ during c. elegans postembryonic development. *PloS one*, 9 (10):e110689, 2014.

G. Bradski. The OpenCV Library. *Dr. Dobb's Journal of Software Tools*, 2000.

Otto Bütschli. *Studien über die ersten Entwicklungsvorgänge der Eizelle, die Zelltheilung und die Conjugation der Infusorien*. C. Winter, 1876.

Peter B Canham. The minimum energy of bending as a possible explanation of the biconcave shape of the human red blood cell. *Journal of theoretical biology*, 26(1):61–81, 1970.

Riccardo Capovilla and Jemal Guven. Stresses in lipid membranes. *Journal of Physics A: Mathematical and General*, 35(30):6233, 2002.

Riccardo Capovilla, Jemal Guven, and Efrain Rojas. Hamilton's equations for a fluid membrane. *Journal of Physics A: Mathematical and General*, 38(41):8841, 2005.

Ana Carvalho, Arshad Desai, and Karen Oegema. Structural memory in the contractile ring makes the duration of cytokinesis independent of cell size. *Cell*, 137(5):926–937, 2009. ISSN 00928674.

Guillaume T Charras, Timothy J Mitchison, and L Mahadevan. Animal cell hydraulics. *Journal of cell science*, 122(18):3233–3241, 2009.

Andrew G. Clark and Ewa Paluch. Mechanics and regulation of cell shape during the cell cycle. In Jacek Z. Kubiak, editor, *Cell Cycle in Development*, pages 31–73. Springer Berlin Heidelberg, 2011.

Andrew G Clark, Kai Dierkes, and Ewa K Paluch. Monitoring actin cortex thickness in live cells. *Biophysical journal*, 105(3):570–580, 2013.

David Cohen-Steiner and Jean-Marie Morvan. Restricted delaunay triangulations and normal cycle. SCG '03, page 312–321, New York, NY, USA, 2003. Association for Computing Machinery. ISBN 1581136633.

Carrie R Cowan and Anthony A Hyman. Asymmetric cell division in c. elegans: cortical polarity and spindle positioning. *Annu. Rev. Cell Dev. Biol.*, 20(1):427–453, 2004.

Marina E Crowder, Magdalena Strzelecka, Jeremy D Wilbur, Matthew C Good, George Von Dassow, and Rebecca Heald. A comparative analysis of spindle morphometrics across metazoans. *Current Biology*, 25(11):1542–1550, 2015.

Katsuma Dan and Jean Clark Dan. Behavior of the cell surface during cleavage. viii. on the cleavage of medusan eggs. *The Biological Bulletin*, 93(2):163–188, 1947.

Dawson-Haggerty et al. trimesh, 2019.

MC Delfour and Jean-Paul Zolésio. Shapes and geometries, volume 22 of advances in design and control. *Society for Industrial and Applied Mathematics (SIAM), Philadelphia, PA,*, 2011.

HJ Deuling and W Helfrich. The curvature elasticity of fluid membranes: a catalogue of vesicle shapes. *Journal de Physique*, 37(11): 1335–1345, 1976.

Jonas F Dorn, Li Zhang, Tan-Trao Phi, Benjamin Lacroix, Paul S Maddox, Jian Liu, and Amy Shaub Maddox. A theoretical model of cytokinesis implicates feedback between membrane curvature and cytoskeletal organization in asymmetric cytokinetic furrowing. *Molecular biology of the cell*, 27(8):1286–1299, 2016.

Helge Feddersen, Laeschkir Würthner, Erwin Frey, and Marc Bramkamp. Dynamics of the bacillus subtilis min system. *mBio*, 12 (2):e00296–21, 2021.

Elisabeth Fischer-Friedrich, Yusuke Toyoda, Cedric J Cattin, Daniel J Müller, Anthony A Hyman, and Frank Jülicher. Rheology of the active cell cortex in mitosis. *Biophysical journal*, 111(3):589–600, 2016.

Nils C. Gauthier, Olivier M. Rossier, Anurag Mathur, James C. Hone, and Michael P. Sheetz. Plasma membrane area increases with spread area by exocytosis of gpi anchored protein compartment. *Biophysical Journal*, 96(3):151a, 2009.

Emily W Gehrels, Bandan Chakrabortty, Marc-Eric Perrin, Matthias Merkel, and Thomas Lecuit. Curvature gradient drives polarized tissue flow in the drosophila embryo. *Proceedings of the National Academy of Sciences*, 120(6):e2214205120, 2023.

Nathan W Goehring, Philipp Khuc Trong, Justin S Bois, Debanjan Chowdhury, Ernesto M Nicola, Anthony A Hyman, and Stephan W

Grill. Polarization of par proteins by advective triggering of a pattern-forming system. *Science*, 334(6059):1137–1141, 2011.

HP Greenspan. On the dynamics of cell cleavage. *Journal of Theoretical Biology*, 65(1):79–99, 1977.

Pavel Grinfeld et al. *Introduction to tensor analysis and the calculus of moving surfaces*, volume 1. Springer, 2013.

Peter Gross, K Vijay Kumar, Nathan W Goehring, Justin S Bois, Carsten Hoege, Frank Jülicher, and Stephan W Grill. Guiding self-organized pattern formation in cell polarity establishment. *Nature physics*, 15 (3):293–300, 2019.

Daniel P. Haeusser and William Margolin. Splitsville: structural and functional insights into the dynamic bacterial z ring. *Nature Reviews Microbiology*, 14(5):305–319, 2016.

Wolfgang Helfrich. Elastic properties of lipid bilayers: theory and possible experiments. *Zeitschrift für Naturforschung c*, 28(11-12):693–703, 1973.

Y Hiramoto. Cell division without mitotic apparatus in sea urchin eggs. *Experimental cell research*, 11(3):630–636, 1956.

Jonathon Howard. *Mechanics of Motor Proteins and the Cytoskeleton*. Sinauer Associates, Sunderland, MA, 2001. ISBN 0878933344.

Jonathon Howard, Stephan W Grill, and Justin S Bois. Turing's next steps: the mechanochemical basis of morphogenesis. *Nature Reviews Molecular Cell Biology*, 12(6):392–398, 2011.

Martin Howard, Andrew D. Rutenberg, and Simon De Vet. Dynamic compartmentalization of bacteria: Accurate division in *E. Coli*. *Physical Review Letters*, 87(27):278102, 2001.

Christina Rou Hsu, Gaganpreet Sangha, Wayne Fan, Joey Zheng, and Kenji Sugioka. Contractile ring mechanosensation and its anillin-dependent tuning during early embryogenesis. *Nature Communications*, 14(1):8138, 2023.

Thomas Jankuhn, Maxim Olshanskii, and Arnold Reusken. Incompressible fluid problems on embedded surfaces: Modeling and variational formulations. *Interfaces and Free Boundaries*, 20(3):353–377, November 2018.

Charles F Jekel. *Obtaining non-linear orthotropic material models for PVC-coated polyester via inverse bubble inflation*. PhD thesis, Stellenbosch: Stellenbosch University, 2016.

Alastair D Jenkins and Kristian B Dysthe. The effective film viscosity coefficients of a thin floating fluid layer. *Journal of Fluid Mechanics*, 344:335–337, 1997.

Frank Jülicher, Armand Ajdari, and Jacques Prost. Modeling molecular motors. *Reviews of Modern Physics*, 69(4):1269, 1997.

Frank Jülicher, Stephan W Grill, and Guillaume Salbreux. Hydrodynamic theory of active matter. *Reports on Progress in Physics*, 81(7): 076601, 2018.

Renat N Khaliullin, Rebecca A Green, Linda Z Shi, J Sebastian Gomez-Cavazos, Michael W Berns, Arshad Desai, and Karen Oegema. A positive-feedback-based mechanism for constriction rate acceleration during cytokinesis in caenorhabditis elegans. *eLife*, 7:e36073, 2018.

Juergen A Knoblich. Asymmetric cell division during animal development. *Nature reviews Molecular cell biology*, 2(1):11–20, 2001.

Eugene V Koonin. The origin and early evolution of eukaryotes in the light of phylogenomics. *Genome biology*, 11(5):209, 2010.

Hiroshi Koyama, Tamiki Umeda, Kazuyuki Nakamura, Tomoyuki Higuchi, and Akatsuki Kimura. A high-resolution shape fitting and simulation demonstrated equatorial cell surface softening during cytokinesis and its promotive role in cytokinesis. *PLoS One*, 7(2): e31607, 2012.

Erwin Kreyszig. *Differential geometry*, volume 11. Courier Corporation, 1991.

Karsten Kruse. A dynamic model for determining the middle of escherichia coli. *Biophysical Journal*, 82(2), 2002.

Dmitri M Krylov, Kim Nasmyth, and Eugene V Koonin. Evolution of eukaryotic cell cycle regulation: stepwise addition of regulatory kinases and late advent of the cdks. *Current Biology*, 13(2):173–177, 2003.

Nick Lane and William Martin. The energetics of genome complexity. *Nature*, 467(7318):929–934, 2010.

Petra Anne Levin, Iren G. Kurtser, and Alan D. Grossman. Identification and characterization of a negative regulator of FtsZ ring formation in *Bacillus subtilis*. *Proceedings of the National Academy of Sciences*, 96(17):9642–9647, 1999.

Ping-Sung Liao, Tse-Sheng Chen, Pau-Choo Chung, et al. A fast algorithm for multilevel thresholding. *J. Inf. Sci. Eng.*, 17(5):713–727, 2001.

Weida Liao and Eric Lauga. Hydrodynamic mechanism for stable spindle positioning in meiosis ii oocytes. *PRX Life*, 2(4):043003, 2024.

Issei Mabuchi. Biochemical aspects of cytokinesis. *International review of cytology*, 101:175–213, 1986.

Issei Mabuchi. Cleavage furrow: timing of emergence of contractile ring actin filaments and establishment of the contractile ring by filament bundling in sea urchin eggs. *Journal of Cell Science*, 107(7): 1853–1862, 1994.

Issei Mabuchi and Makoto Okuno. The effect of myosin antibody on the division of starfish blastomeres. *The Journal of cell biology*, 74(1): 251–263, 1977.

Amy Shaub Maddox, Lindsay Lewellyn, Arshad Desai, and Karen Oegema. Anillin and the septins promote asymmetric ingression of the cytokinetic furrow. *Developmental Cell*, 12(5):827–835, 2007.

L Martínez-Balbuena, A Arteaga-Jiménez, E Hernández-Zapata, and E Urrutia-Buñuelos. Application of the helfrich elasticity theory to the morphology of red blood cells. *American Journal of Physics*, 89(5): 465–476, 2021.

MathWorks. Matlab, 2024.

Pamela Maupin and Thomas D Pollard. Arrangement of actin filaments and myosin-like filaments in the contractile ring and of actin-like filaments in the mitotic spindle of dividing hela cells. *Journal of ultrastructure and molecular structure research*, 94(1):92–103, 1986.

Mirjam Mayer, Martin Depken, Justin S Bois, Frank Jülicher, and Stephan W Grill. Anisotropies in cortical tension reveal the physical basis of polarizing cortical flows. *Nature*, 467(7315):617–621, 2010.

JF McClendon. A note on the dynamics of cell division: a reply to robertson. *Archiv für Entwicklungsmechanik der Organismen*, 34(2): 263–266, 1912.

Vidya V Menon, SS Soumya, Amal Agarwal, Sundar R Naganathan, Mandar M Inamdar, and Anirban Sain. Asymmetric flows in the intercellular membrane during cytokinesis. *Biophysical Journal*, 113 (12):2787–2795, 2017.

Teije C Middelkoop, Jonas Neipel, Caitlin E Cornell, Ronald Naumann, Lokesh G Pimpale, Frank Jülicher, and Stephan W Grill. A cytokinetic ring-driven cell rotation achieves hertwig's rule in early development. *Proceedings of the National Academy of Sciences*, 121(25): e2318838121, 2024.

Alexander Mietke, V Jemseena, K Vijay Kumar, Ivo F Sbalzarini, and Frank Jülicher. Minimal model of cellular symmetry breaking. *Physical Review Letters*, 123(18):188101, 2019a.

Alexander Mietke, Frank Jülicher, and Ivo F Sbalzarini. Self-organized shape dynamics of active surfaces. *Proceedings of the National Academy of Sciences*, 116(1):29–34, 2019b.

Ron Milo, Paul Jorgensen, Uri Moran, Griffin Weber, and Michael Springer. Bionumbers—the database of key numbers in molecular and cell biology. *Nucleic acids research*, 38(suppl_1):D750–D753, 2010.

Makito Miyazaki, Masataka Chiba, Hiroki Eguchi, Takashi Ohki, and Shin'ichi Ishiwata. Cell-sized spherical confinement induces the spontaneous formation of contractile actomyosin rings in vitro. *Nature cell biology*, 17(4):480–489, 2015.

Edwin Munro and Bruce Bowerman. Cellular symmetry breaking during caenorhabditis elegans development. *Cold Spring Harbor perspectives in biology*, 1(4):a003400, 2009.

M Musy, G Jacquenot, G Dalmasso, R de Bruin, A Pollack, F Claudi, C Badger, B Sullivan, D Hrisca, D Volpatto, et al. vedo, a python module for scientific analysis and visualization of 3d objects and point clouds. *Zenodo*, 1, 2021.

Sundar Ram Naganathan, Sebastian Fürthauer, Josana Rodriguez, Bruno Thomas Fievet, Frank Jülicher, Julie Ahringer, Carlo Vittorio Cannistraci, and Stephan W Grill. Morphogenetic degeneracies in the actomyosin cortex. *eLife*, 7:e37677, 2018.

Masatoshi Nishikawa, Sundar Ram Naganathan, Frank Jülicher, and Stephan W. Grill. Controlling contractile instabilities in the actomyosin cortex. *eLife*, 6:e19595, 2017.

Fabian Pedregosa, Gaël Varoquaux, Alexandre Gramfort, Vincent Michel, Bertrand Thirion, Olivier Grisel, Mathieu Blondel, Peter Prettenhofer, Ron Weiss, Vincent Dubourg, et al. Scikit-learn: Machine learning in python. *the Journal of machine Learning research*, 12: 2825–2830, 2011.

Robert J Pelham Jr and Fred Chang. Actin dynamics in the contractile ring during cytokinesis in fission yeast. *Nature*, 419(6902):82–86, 2002.

MM Perry, HA John, and NST Thomas. Actin-like filaments in the cleavage furrow of newt egg. *Experimental cell research*, 65(1):249–253, 1971.

Jason R Picardo, V Jemseena, and K Vijay Kumar. Active waves from nonreciprocity and cytoplasmic exchange. *Physical Review E*, 112(2): L022401, 2025.

Thomas D Pollard and Ben O'Shaughnessy. Molecular mechanism of cytokinesis. *Annual review of biochemistry*, 88(1):661–689, 2019.

Thomas R Powers. Dynamics of filaments and membranes in a viscous fluid. *Reviews of Modern Physics*, 82(2):1607–1631, 2010.

Raymond Rappaport. *Cytokinesis in animal cells*. Cambridge University Press, 1996.

David M. Raskin and Piet A. J. De Boer. Rapid pole-to-pole oscillation of a protein required for directing division to the middle of *Escherichia coli*. *Proceedings of the National Academy of Sciences*, 96(9): 4971–4976, 1999.

Paul Renteln. *Manifolds, Tensors and Forms*. Cambridge University Press, 2014.

Anne-Cecile Reymann, Fabio Staniscia, Anna Erzberger, Guillaume Salbreux, and Stephan W Grill. Cortical flow aligns actin filaments to form a furrow. *eLife*, 5:e17807, 2016.

Arnab Saha, Masatoshi Nishikawa, Martin Behrndt, Carl-Philipp Heisenberg, Frank Jülicher, and Stephan W Grill. Determining physical properties of the cell cortex. *Biophysical journal*, 110(6): 1421–1429, 2016.

Ryota Sakamoto, Ziane Izri, Yuta Shimamoto, Makito Miyazaki, and Yusuke T Maeda. Geometric trade-off between contractile force and viscous drag determines the actomyosin-based motility of a cell-sized droplet. *Proceedings of the National Academy of Sciences*, 119 (30):e2121147119, 2022.

Guillaume Salbreux and Frank Jülicher. Mechanics of active surfaces. *Physical Review E*, 96(3):032404, 2017.

Guillaume Salbreux, Jacques Prost, and Jean-Francois Joanny. Hydrodynamics of cellular cortical flows and the formation of contractile rings. *Physical review letters*, 103(5):058102, 2009.

Guillaume Salbreux, Guillaume Charras, and Ewa Paluch. Actin cortex mechanics and cellular morphogenesis. *Trends in cell biology*, 22(10): 536–545, 2012.

Johannes Schindelin, Ignacio Arganda-Carreras, Erwin Frise, Verena Kaynig, Mark Longair, Tobias Pietzsch, Stephan Preibisch, Curtis Rueden, Stephan Saalfeld, Benjamin Schmid, et al. Fiji: an open-source platform for biological-image analysis. *Nature methods*, 9(7): 676–682, 2012.

TE Schroeder. Cytokinesis: filaments in the cleavage furrow. *Experimental cell research*, 53(1):272–276, 1968.

Thomas E Schroeder. The contractile ring: I. fine structure of dividing mammalian (hela) cells and the effects of cytochalasin b. *Zeitschrift für Zellforschung und mikroskopische Anatomie*, 109(4):431–449, 1970.

Thomas E Schroeder. Actin in dividing cells: contractile ring filaments bind heavy meromyosin. *Proceedings of the National Academy of Sciences*, 70(6):1688–1692, 1973.

Udo Seifert. Configurations of fluid membranes and vesicles. *Advances in physics*, 46(1):13–137, 1997.

Udo Seifert, Karin Berndl, and Reinhard Lipowsky. Shape transformations of vesicles: Phase diagram for spontaneous-curvature and bilayer-coupling models. *Physical review A*, 44(2):1182, 1991.

John Maynard Smith and Eors Szathmary. *The major transitions in evolution*. Oxford University Press, 1997.

Laurie G Smith. Plant cytokinesis: motoring to the finish. *Current biology*, 12(6):R206–R208, 2002.

Josef Spek. Oberflächenspannungsdifferenzen als eine ursache der zellteilung. *Archiv für Entwicklungsmechanik der Organismen*, 44(1): 5–113, 1918. ISSN 1432-041X.

Felix Spira, Sara Cuylen-Haering, Shalin Mehta, Matthias Samwer, Anne Reversat, Amitabh Verma, Rudolf Oldenbourg, Michael Sixt, and Daniel W Gerlich. Cytokinesis in vertebrate cells initiates by contraction of an equatorial actomyosin network composed of randomly oriented filaments. *eLife*, 6:e30867, 2017.

Sebastian J Streichan, Matthew F Lefebvre, Nicholas Noll, Eric F Wieschaus, and Boris I Shraiman. Global morphogenetic flow is accurately predicted by the spatial distribution of myosin motors. *Elife*, 7:e27454, 2018.

Georg Strompen, Farid El Kasmi, Sandra Richter, Wolfgang Lukowitz, Farhah F Assaad, Gerd Jürgens, and Ulrike Mayer. The arabidopsis hinkel gene encodes a kinesin-related protein involved in cytokinesis and is expressed in a cell cycle-dependent manner. *Current Biology*, 12(2):153–158, 2002.

M. M. Swann and J. M. Mitchison. Cleavage of sea-urchin eggs in colchicine. *Journal of Experimental Biology*, 30(4):506–514, 1953.

Jack W. Szostak, David P. Bartel, and P. Luigi Luisi. Synthesizing life. *Nature*, 409(6818):387–390, 2001.

William Thielicke and René Sonntag. Particle image velocimetry for matlab: Accuracy and enhanced algorithms in pivlab. *Journal of Open Research Software*, 9(1), 2021.

Sathish Thiyagarajan, Shuyuan Wang, Ting Gang Chew, Junqi Huang, Lokesh Kumar, Mohan K Balasubramanian, and Ben O'Shaughnessy. Myosin turnover controls actomyosin contractile instability. *Proceedings of the National Academy of Sciences*, 119(43):e2211431119, 2022.

Tracy Y Thomas. *Concepts from tensor analysis and differential geometry*. Elsevier, 1961.

D'Arcy Wentworth Thompson. *On Growth and Form*. Cambridge University Press, Cambridge, UK, 1917.

H Tosuji, Issei Mabuchi, Nobuhiro Fusetani, and Tohru Nakazawa. Calyculin A induces contractile ring-like apparatus formation and condensation of chromosomes in unfertilized sea urchin eggs. *Proceedings of the National Academy of Sciences*, 89(22):10613–10617, 1992.

Philipp Khuc Trong, Ernesto M Nicola, Nathan W Goehring, K Vijay Kumar, and Stephan W Grill. Parameter-space topology of models for cell polarity. *New Journal of Physics*, 16(6):065009, 2014.

A.M. Turing. The chemical basis of morphogenesis. *Philosophical Transactions of the Royal Society of London. Series B, Biological Sciences*, 237(641):37–72, 1952.

Hervé Turlier, Basile Audoly, Jacques Prost, and Jean-François Joanny. Furrow constriction in animal cell cytokinesis. *Biophysical Journal*, 106(1):114–123, 2014.

Stefan Van der Walt, Johannes L Schönberger, Juan Nunez-Iglesias, François Boulogne, Joshua D Warner, Neil Yager, Emmanuelle Gouillart, and Tony Yu. scikit-image: image processing in python. *PeerJ*, 2:e453, 2014.

Sven K Vogel, Christian Wölfer, Diego A Ramirez-Diaz, Robert J Flassig, Kai Sundmacher, and Petra Schwille. Symmetry breaking and emergence of directional flows in minimal actomyosin cortices. *Cells*, 9(6):1432, 2020.

Shawn W Walker. *The shapes of things: a practical guide to differential geometry and the shape derivative*. SIAM, 2015.

Allen M Waxman. Dynamics of a couple-stress fluid membrane. *Studies in Applied Mathematics*, 70(1):63–86, 1984.

J.G. White and G.G. Borisy. On the mechanisms of cytokinesis in animal cells. *Journal of Theoretical Biology*, 101(2):289–316, 1983.

Lewis Wolpert, Cheryll Tickle, and Alfonso Martinez Arias. *Principles of development*. Oxford University Press, USA, 2015.

Hai-Yin Wu, Gökberk Kabacaoğlu, Ehssan Nazockdast, Huan-Cheng Chang, Michael J Shelley, and Daniel J Needleman. Laser ablation and fluid flows reveal the mechanism behind spindle and centrosome positioning. *Nature Physics*, 20(1):157–168, 2024.

Pei-Hsun Wu, Dikla Raz-Ben Aroush, Atef Asnacios, Wei-Chiang Chen, Maxim E Dokukin, Bryant L Doss, Pauline Durand-Smet, Andrew Ekpenyong, Jochen Guck, Nataliia V Guz, et al. A comparison of methods to assess cell mechanical properties. *Nature methods*, 15 (7):491–498, 2018.

Naohide Yatsu. Observations and experiments on the ctenophore egg: I. the structure of the egg and. *Journal of the College of Science, Imperial University of Tokyo*, 32(3):1–21, 1912.

Alexander Zumdieck, Karsten Kruse, Henrik Bringmann, Anthony A Hyman, and Frank Jülicher. Stress generation and filament turnover during actin ring constriction. *PloS one*, 2(8):e696, 2007.

LIST OF PUBLICATIONS

- **Active geometrodynamics predicts the emergence of cytokinesis**
  Aditya Singh Rajput, Kunal Kumar, Masatoshi Nishikawa, K. Vijay Kumar
  bioRxiv, 10.1101/2025.11.07.683232 (2025)

- **Geometric Localisation of Active Patterns**
  Kunal Kumar*, Aditya Singh Rajput*, V. Jemseena, K. Vijay Kumar [*in preparation*]

- **Self-organisation in embryonic cell-division: signalling, mechanics, geometry** [*review article*]
  Aditya Singh Rajput, K. Vijay Kumar [*in preparation*]

OTHER PUBLICATIONS

- **Shape-dependent motility of polar inclusions in active baths**
  Pritha Dolai*, Aditya Singh Rajput*, K. Vijay Kumar
  Physical Review E., **110**, 014607 10.1103/PhysRevE.110.014607 (2024)

* equal contribution